The Synthesis and Characterization of Model Interface Couples for Inorganic Matrix Composite Applications

by

Brent Victor Chambers

B.E., Vanderbilt University, 1983

S.M., Massachusetts Institute of Technology, 1987

Submitted to the Department of
Materials Science and Engineering
in Partial Fulfillment of the Requirements for the Degree of
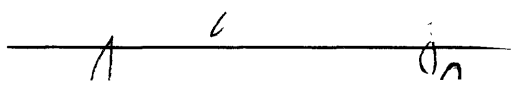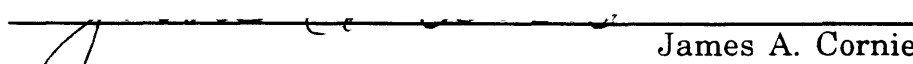
DOCTOR OF PHILOSOPHY

at the

MASSACHUSETTS INSTITUTE OF TECHNOLOGY

April 29, 1994

© Massachusetts Institute of Technology 1994

Signature of author_____
Department of Materials Science and Engineering
April 29, 1994

Certified by _____
Ali S. Argon
Thesis Supervisor

Certified by _____
James A. Cornie
Thesis Supervisor

Accepted by_____
C. V. Thompson, Chairman
Departmental Committee on Graduate Students
Department of Materials Science and Engineering

The Synthesis and Characterization of Model Interface Couples for Inorganic Matrix Composite Applications

by
Brent Victor Chambers

Submitted to the Department of Materials Science and Engineering
on April 29, 1994 in partial fulfillment of the Requirements for the Degree
of Doctor of Philosophy in Materials Engineering.

ABSTRACT

The fracture toughness of fiber reinforced composites may be optimized without unwarranted loss of transverse strength through control of the interface strength between reinforcing material and matrix. These design considerations, including limits on the permissible interface strengths, have been delineated by others. This present work examines the effect of carbon interlayers on the tensile strength of flat interface couples representing the interface between fiber and its coating. Polished single crystal sapphire wafers, 1.0 inch in diameter and 0.5 mm thick, were substituted for the fiber; relatively thick, $2\mu m$, SiC coatings are substituted for the thin coatings used in composite materials; and 2000Å carbon interlayers, being the weakest material present, act as mechanical fuses to control the overall strength of the entire system.

As the SiC coatings had to be relatively thick, homogenous, and nearly stress-free, a study of the deposition of SiC by plasma enhanced chemical vapor deposition (PECVD) was conducted. Coatings with a nearly zero residual stress were deposited at 275°C, $50\mu m$ pressure and 30 watts applied power with the lower electrode self-biased at +3 volts. Uniform deposition was insured through the use of hydrogen as a dilution gas.

The carbon interlayers processed by PECVD at 400°C deposited on sapphire were found by high resolution TEM to be amorphous or microcystalline carbon depending on the applied rf power. Carbon deposited on microcrystalline SiC by low pressure CVD between 1100 and 1500°C was determined by x-ray diffraction to be highly oriented in structure with the degree of preferred orientation increasing from a Bacon Anisotropy Factor of 4.5 for material deposited on SiC at 1100°C to 6.8 for material deposited at 1500°C.

Strength of the SiC/C/Sapphire couples was determined through a technique called laser spallation whereby a laser is pulsed onto a thin absorbing layer on the reverse side of the substrate; the laser impact creates a shock wave which propagates through the substrate, gets reflected from the front surface where it is converted into a tension wave, and, if of sufficient intensity, causes delamination of the film. This phenomena itself is investigated using a high speed digitizer to examine shock wave propagation through piezo-electric quartz and is also modeled with finite element techniques.

The tensile strength of the sapphire/SiC interface was found to be 14.7 MPa for LPCVD SiC and 10.0 MPa for PECVD SiC. Couples with amorphous carbon interlayers had a strength of 2.0 MPa. The strength of interface couples with highly oriented carbon interlayers scaled with the carbon processing temperature.

Thesis Supervisor: Professor Ali S. Argon
Title: Quentin Berg Professor of Mechanical Engineering
Thesis Supervisor: Doctor James A. Cornie
Title: Principal Research Associate

Acknowledgments

It is now the early morning hours of a day late in the year of 1993. Bob Dylan blasts from my boom box. A few things left to do and I am out of here. This savage journey is almost over. Of the materials class of 1983 I am the last one left. The rest are gone. I alone walk the halls at night and soon all that will be left of me is the back of my head in the picture of Professor Sadoway's class in the Infinite Corridor. I am reminded of that verse, "A man dies and his place does not remember him."

It has been an honor and a joy to work with Professor Ali Argon. He has amazing wisdom and pastoral gifts, as well as a sharp wit. I am glad Jim Cornie knew the value of the graduate process. I have really appreciated Ken Russel's nose for what is "a thesis." Professor Carl Thompson gently turned up the heat at the proper time. These people were my committee and I am grateful for the part each played in my initiation.

There are the people who have been next to me and walked this road with me. Ibrahim Ucok and Ralph Mason were my best friends from the group next door. Ibo gave me all the hospitality of the east and managed to teach even me a little Turkish. Ralph was my paddling partner; on the night after my oral exam he called me up, "Do you want to go boating tomorrow?" Veronique Michaud showed me how a woman can do the thesis ritual without losing the connection to her feelings. She worked harder than most, but I never knew her to pull an all-nighter, deprive herself of food, or to be bad tempered. (I, on the other hand, have pulled at least one all-nighter for every page in this thesis.) Tom Piccone was my Christian brother in lab. Not that we always talked shop, but he was an example how a Christian does a thesis. I also am grateful for his willingness to help with any computer problems that came up. I have enjoyed sharing lab space with David Dunand and Shiyu Zhang. John Matz and Juan Bruno pumped me up in the weight room as well as in lab. I am also grateful for the friendship of Jackie Isaacs, Tami Jonas, Gerad Sommer, Qi Zhao, Robert Calhoun, Elizabeth Earhart, Nathan Taylor, Pavel Bystricky, Chris San Marchi.....

Maria Due helped in countless ways. Her service was so selfless and good natured. She got out of here before most of us and how we have all missed her. I am also grateful for the training I received from John Martin and Libby Shaw in the Surface Lab. Libby is one of the most gifted teachers I have known. Rich Perilli and Tim McClure are the characters that run the micro lab. Only they could put out the fires, joke, laugh and help all at the same time. Gunter Arndt is a master and I mean that in the old sense of the word. His wisdom and skill in engineering is amazing. I worked with him as an apprentice. I would also like to acknowledge

4

There have also been some anonymous types: Clark, Jack, Ed, Roy, Margot, Susan, Charlie, Bob, Paul, Matt, Nathaniel, Janis, Lucy, and others. These people helped me stay sober and balanced.

George Lindsay has been an important character in my life. He guided me through the rebuilding of several old chevy engines and he taught me how to get the job done with whatever was on hand. He is a master mechanic.

Ken Larsen is also a master, a master of the schools from New York, Oslo, Zurich, and Jerusalem. I am grateful for his wisdom, not only in its content, but also for the way in which he has brought it to me.

As an undergrad I approached Professor Barry Lichter at Vanderbilt University and asked him to write a recommendation for me to graduate school. He agreed on the condition that I apply to MIT. "I would have you work for me, but it would be better for you to go there." I am extremely grateful for his guidance.

Barbara Collins helped. She kept me company through difficult stages of writing and did extensive editorial and layout work. But, Barbara Collins no longer exists. She is now Barbara Chambers and she is a most wise and beautiful woman. Her love has been deeply satisfying.

This work is dedicated to my family. I am very grateful for the love which they have expressed to me in innumerable ways. I see myself as their son, the son of farmers, railroad and highway men, engineers, and businessmen, the son of good, hard working people who love each other and are the good citizens without which no city or nation can stand. I pray that I may be found faithful with the heritage that I have received.

Shortly before I came to MIT I became a Christian and it is difficult for me to distinguish between my life at MIT and my life in Jesus. It is here that He sheltered me and healed me and revealed Himself to me. I leave MIT as a medieval monk might have left his monastery, full of fear, yet confident of Him who called me and goes before me. I praise His name and confess Him as Lord.

"Jesus answered and said to them, 'This is the work of God, that you believe in Him whom He has sent.'"

John 6.29

5

Table of Contents

6

List of Illustrations and Figures

8

List of Tables

I. Introduction

Composite materials are composed of two phases, a reinforcing material and a matrix. The materials that make up the two components are chosen to suit a particular application such that the desirable properties of each component may be maximized while minimizing their particular weaknesses. For metal matrix composites with continuous ceramic fiber reinforcement it is possible to bring together the high stiffness of the fiber with the toughness of the metal to produce a material with an extremely high strength to weight ratio.

Many problems associated with these materials stem from their fracture behavior. If the matrix and reinforcing material are strongly bonded, cracks originating in the matrix will easily propagate through both the matrix and fiber, leading to sudden, catastrophic failure. As the application most concerned with materials with high strength to weight ratios centers around flight, mechanical failure needs to be graceful, i.e., gradual and not abrupt. If the matrix and reinforcing material are weakly bonded, the material will not fail in a sudden manner; however, it will then have low transverse strength. Indeed, composites have a high density of interfaces and the bulk mechanical properties of the composite are largely determined by the interface strength between the matrix and the reinforcing material.

Therefore, attention has shifted from the properties of the individual components to control of the interface between them. Coatings have been applied to the fibers to keep them from reacting with the matrix to produce

brittle products that lead to crack initiation. Argon [1] introduced the concept of using these coatings to control the interface strength to act as a mechanical fuse deflecting cracks in a controlled manner. Argon and Gupta [2] have elucidated the theoretical design considerations in which composite toughness may be maximized without undue sacrifice of composite transverse strength. The purpose of this work was to process an interface for the sapphire/SiC system with a specific tensile strength as prescribed using the design criteria Argon and Gupta.

In the second chapter of this thesis the theoretical framework of interface tailoring is discussed and the strategy behind the model couples is presented. Theoretical discussion focuses on the works of Argon, Cornie, and Gupta and will include the calculation of the desired interface strength for crack bridging and frictional pullout for composites reinforced with SiC-coated sapphire fibers. The model interface couples consist of SiC and carbon films deposited on sapphire wafers and different aspects of the processing and testing of these couples are examined in depth in subsequent chapters.

Chapter 3 focuses on the processing of SiC coatings by plasma enhanced chemical vapor deposition (PECVD). This chapter involves questions of uniformity of deposition, homogeneity of structure, and residual stresses in coatings. The literature pertaining to each of these subjects is briefly reviewed and the method used to determine satisfactory processing conditions is detailed. Finally, processing parameters required to produce a homogenous, low stress, $2\mu m$ thick SiC coating are presented.

Chapter 4 is dedicated to the processing and evaluation of carbon films deposited by both plasma and thermal CVD. The chapter begins by briefly outlining the literature relating the processing / structure

relationship in the deposition of carbon. The particular process procedures used in the work are detailed and the structure of carbon films by both deposition processes are examined by x-ray diffraction, transmission electron microscopy (TEM), and x-ray photo-electron spectroscopy (XPS).

Chapter 5 is devoted to the mechanical testing of the model interface couples through the use of a laser spallation technique. In this experiment a laser is pulsed onto a thin absorbing layer on the reverse side of the substrate and an elastic shock wave is created which propagates through the substrate eventually loading the substrate/film interface in tension. If this shock wave is of sufficient amplitude, the interface will separate causing delamination of the film. This phenomenon is experimentally investigated using a high speed digitizer to examine the wave propagation through piezo-electric quartz. These experimental results are then used as a basis for a finite element model to transfer the results from quartz substrates to sapphire substrates. Chapter 5 closes with the tensile strength results of the model couples and the relationship between tensile strength and couples processing is discussed.

Chapter 6 contains a discussion of the entire work, particularly with respect to the design criteria outlined in the second chapter, Chapter 7 presents the conclusions and Chapter 8 contains suggestions for future work.

II. The Design of Interfaces

As the development of fibers for the continuous reinforcing of composites has progressed, attention has shifted from the fibers and matrix to the interface between them. It has become quite apparent that success in controlling the strength and toughness of inorganic composites rests upon control of the interfaces in these materials. The main concern of this work is to contribute to the understanding of the relationship between the processing of interfaces, and the resulting ability to control bulk composite strengths and toughness. The purpose of this chapter is to briefly review the theory regarding control of bulk mechanical composite properties, primarily toughness and longitudinal and transverse strength, through interface design, and then to present the general thinking that was the impetus to this work.

The most desired result of interface control is to achieve composite toughening through the deflection of cracks propagating through the matrix. If these cracks can be deflected at the fiber/matrix or fiber/coating interface, the fibers may still carry longitudinal loads, the crack energy may be consumed through delamination and fiber pull-out, and complete failure may be delayed. This has been called toughening through "interface delamination, crack-bridging, and frictional pull-out [1, 3]" and is shown schematically in Figure 2.1. This phenomenon has been successfully demonstrated in ceramic composite systems [3-5].

Argon and coworkers [6] have mathematically delineated the material requirements for crack deflection at a composite interface while

maintaining maximum transverse composite strength. The lower bound, σ^*, for interface strength is given as:

$$\sigma^*_{(lower\ bound)} = k\ \sigma_t \qquad (2.1)$$

where k is the maximum stress concentration factor due to presence of reinforcing elements and σ_t is the transverse strength of the composite. The upper bound on interface strength is determined by calculating the resistance to crack propagation in all directions at the bimaterial interface and then determining the requirements necessary such that crack propagation resistance is least along the fiber/coating interface.

The physics of the "resistance to cracking" is specified in terms of a strength and an energy release criterion [6], both of which must be met. The strength criteria are specified as two limits in the ratio of material strengths to directional stresses:

$$\frac{\sigma^*_i}{\sigma^*_f} < \frac{\sigma_{\theta\theta}[\theta = \pi/2]}{\sigma_{\theta\theta}[\theta = 0]} \qquad (2.2)$$

$$\frac{\sigma^*_{r\theta}}{\sigma^*_f} < \frac{\sigma_{r\theta}[\theta = \pi/2]}{\sigma_{\theta\theta}[\theta = 0]} \qquad (2.3)$$

The first criterion signifies that the ratio of interface strength, σ^*_i, to fiber strength, σ^*_f, must be less than the ratio of the tensile stress tending to separate the interface ($\sigma_{\theta\theta}[\theta = \pi/2]$) to the tensile stress on the plane across the fiber ($\sigma_{\theta\theta}[\theta = 0]$). (See the schematic in Figure 2.2 showing the crack tip at the bimaterial interface.) The second inequality specifies that the ratio of interface shear strength, $\sigma^*_{r\theta}$, to fiber strength must be less than the ratio of

18

the actual shear stress ($\sigma_{r\theta}[\theta =\pi/2]$) upon the interface to the axial stress across the fiber at the crack tip. The energy criterion for crack deflection at an interface between two materials relates the work of separating the materials to the rate of energy release upon separation:

$$\frac{G_{ci}}{G_{cft}} < \frac{G_d}{G_p} \tag{2.4}$$

meaning that the ratio of the work of separation of the interface, G_{ci}, to work of fracture across the fiber, G_{cft}, must be less than energy release rate for growth along the interface, G_d, to the energy release rate across the fiber, G_p [7].

While it is not possible to state generalized formulae delineating the energy criterion, Gupta, et. al. [6] have specified the strength criterion in the form of delamination charts based on the material properties of the coating and fiber. These charts specify the ratio of stress across the interface to stress along the fiber for both fiber failure and interface delamination as a function of the Dunders parameter, α, and are shown in Figure 2.3 for various Dunders parameters, β. The parameters α and β are bimaterial constants and are defined [6]:

$$\alpha = \frac{[\sqrt{(s_{11}s_{22})_2}/\sqrt{(s_{11}s_{22})_1} - 1]}{[\sqrt{(s_{11}s_{22})_2}/\sqrt{(s_{11}s_{22})_1} + 1]} \tag{2.5}$$

$$\beta = \frac{[\sqrt{s_{11}s_{22}} + s_{12}]_2 - [\sqrt{s_{11}s_{22}} + s_{12}]_1]}{\sqrt{(H_{11}H_{22})}} \tag{2.6}$$

Directions are as defined in Figure 2.2 and s_{11} and s_{22} are the elastic compliances for the fiber and coating, denoted 1 and 2, respectively, and H_{11} and H_{22} are defined as:

$$H_{11} = [2n\lambda^{1/4}\sqrt{s_{11}s_{22}}]_1 + (2n\lambda^{1/4}\sqrt{s_{11}s_{22}})_2 \qquad (2.7)$$

$$H_{11} = [2n\lambda^{-1/4}\sqrt{s_{11}s_{22}}]_1 + (2n\lambda^{-1/4}\sqrt{s_{11}s_{22}})_2 \qquad (2.8)$$

where $\lambda = \dfrac{s_{22}}{s_{11}}$, $n = \sqrt{\dfrac{(1+\rho)}{2}}$, and $\rho = \dfrac{2s_{12} + s_{66}}{\sqrt{s_{11}s_{22}}}$.

The chart is used by first calculating the Dunders parameters for the fiber-coating couple. Note that the Dunders parameter β has less of an effect on the results and may reasonably be assumed to be 1.0 without introducing large error into the calculation. After α is determined for the material pair the value, Φ, read off the chart used to specify the maximum permissible interface strength for interface delamination:

$$\sigma_{i,\,max} = \Phi\,\sigma_f^* \qquad (2.9)$$

The maximum interface strength for SiC coatings on carbon pitch fibers and on sapphire fibers have been calculated as described here and are presented in Table 2.1. Processing of model interface strengths as prescribed by the above theory and listed in Table 2.1 was one of the main goals of this work; later workers could then process interfaces in actual composite materials and mechanically test their composites to verify the entire interface design method. Future workers would be able to use the present results with model interface couples to direct their studies in the actual systems.

Table 2.1 Maximum Allowable Interface Strengths for Interface Delamination

Fiber	Fiber Modulus (GPa)	Fiber Strength (GPa)	Coating	Coating Modulus (GPa)	Maximum Allowable Strength (MPa)
Carbon Pitch-55*	E_{11}, 380 E_{22}, 13	2.12	SiC	448	95
Sapphire**	400	2.5	SiC	448	825

*properties from Cornie [6]
**properties from Battelle [8]

The direction pursued in the present work was taken from the success of the delamination/crack-bridging toughening effect witnessed in several composite systems in which the presence of a carbon or a carbon rich layer at the fiber surface was linked to the toughening [4, 5]. In these cases the carbon rich layer was formed due to a reaction of the fiber with some additive in the matrix during processing; however, this formation process was not understood. Graphite crystals also have properties that are highly dependent upon direction within the crystal and bulk materials have been produced with varying degrees of preferred orientation of crystallites [9]; therefore, it is theorectically possible that carbon films could be produced with strengths varying over a wide range by controlling the degree of preferred orientation among the crystallites; furthermore, the weak bonding between adjacent layers in the carbon crystallite could

provide a path deflecting a crack away from the fiber. The ideal interlayer would contain just enough randomly oriented crystallites to maintain transverse strength while also providing paths deflecting cracks away from the fiber. This is shown schmetically in Figure 2.4. Therefore, it was decided that an attempt would be made to use carbon coatings as interlayers in flat model test couples, shown schematically in Figure 2.5, in order to achieve interface strengths for actual fiber / coating systems predicated by the above design considerations.

The work would be undertaken through two separate, but related, approaches. There would be a processing / property study linking the processing of the model interface specimens to their mechanical properties as determined by laser spallation. In a parallel attack the processing / structure relationship in the production of thin carbon films would be studied. This two part method was necessary as a detailed structure study of the thin carbon layers in the mechanical couples would be very difficult and over extend the project. From the understanding of the processing / structure relationship in the processing of carbon films, a possible structure / property relationship may be contemplated; however, it must be emphasized that this contemplation is speculative as the structure of the carbon interlayers itself has not been studied in depth. This is a summary of the thinking and direction behind the present research now completed.
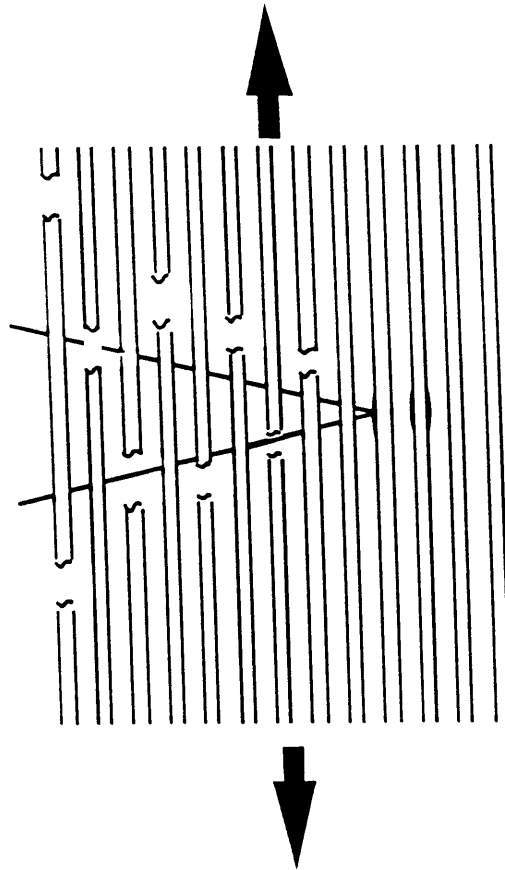
Figure 2.1 Schematic representation of the interface delamination/crack bridging/frictional pull-out composite toughening mechanism, from Cornie[3].
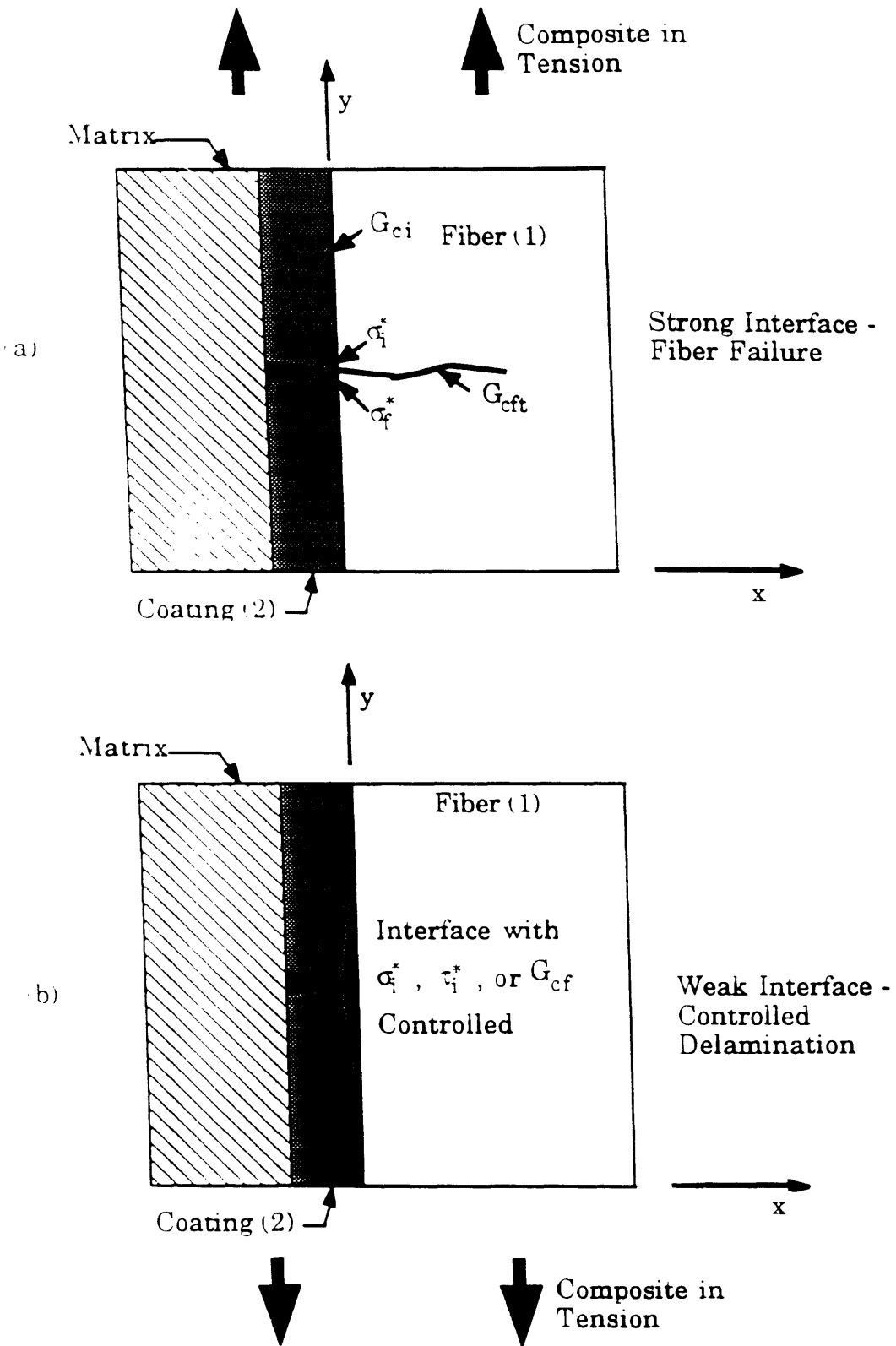
Figure 2.2   Schematic representation of fiber failure and interface
              delamination [3].
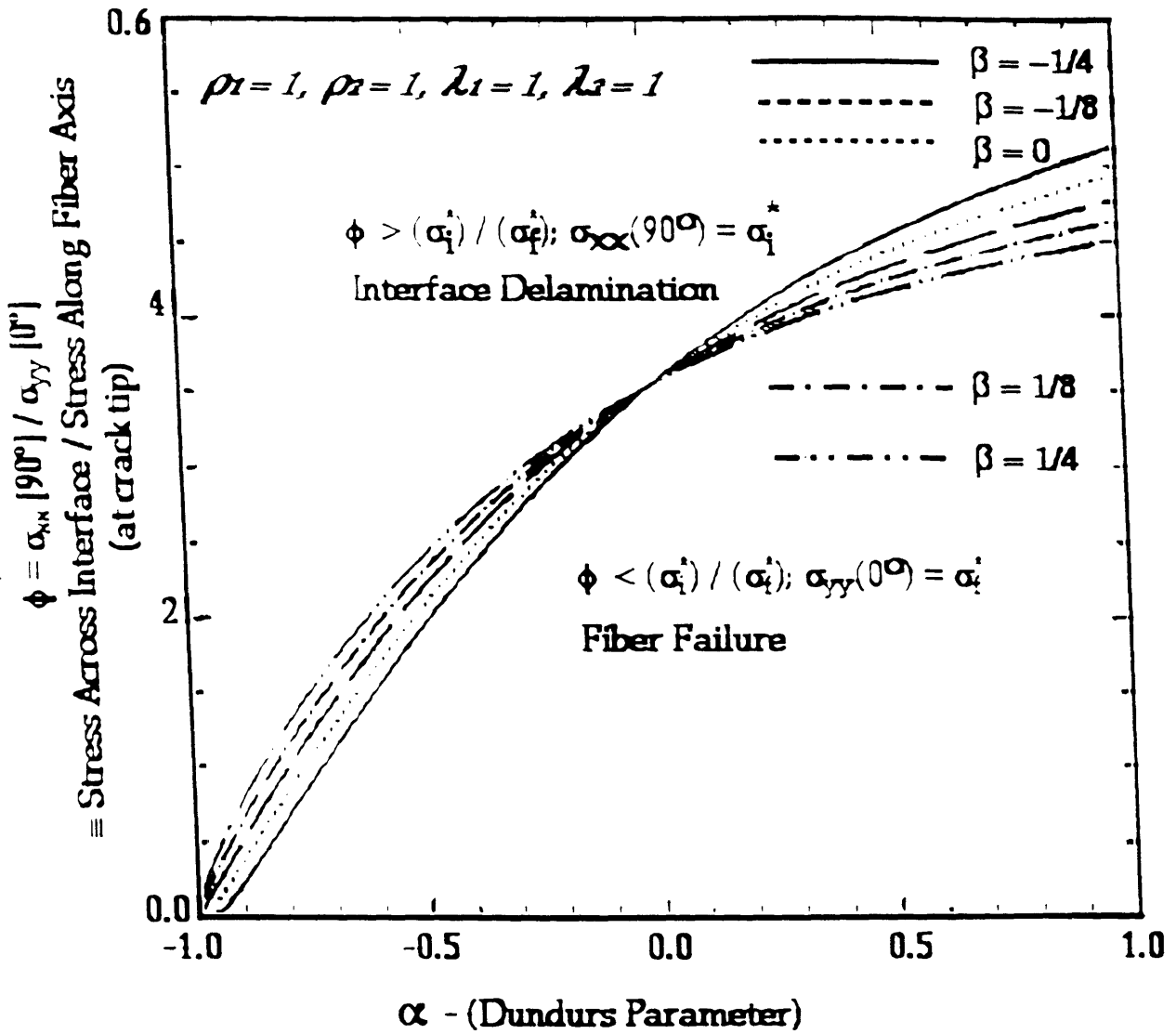
Figure 2.3   Generalized interface delamination chart for some values of
the Dundar's constant, β, from Gupta [6].
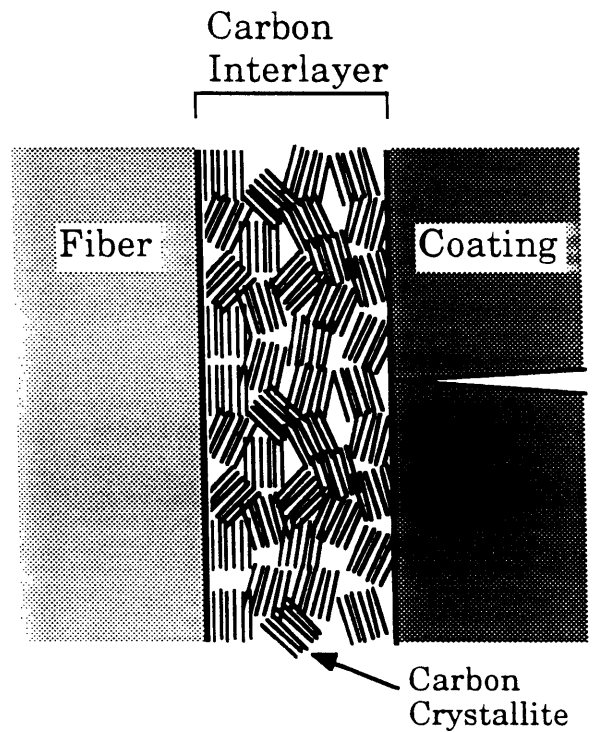
Figure 2.4   Schematic representation of the ideal carbon interlayer,
contaning enough randomly oriented crystallites to maintain
transverse strength while deflecting cracks away from the
fiber.

Interlayer: Carbon, 2000 Angstroms

Ceramic Coating: SiC, 2 μm

Sapphire Wafer, 500μm
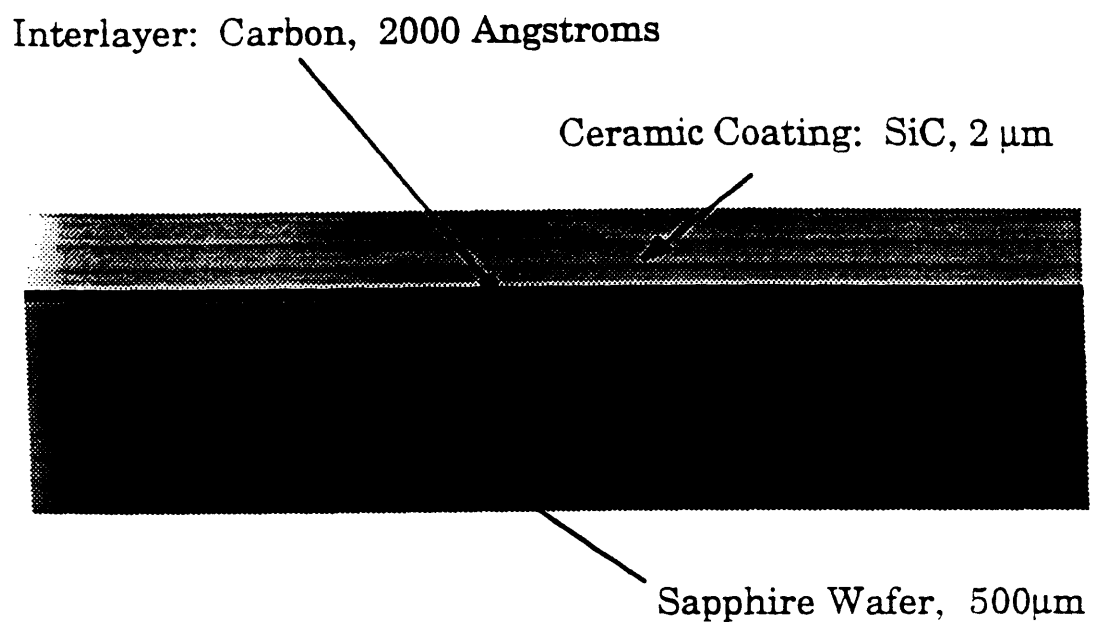
Figure 2.4 Schematic representation of the model interface test specimens.

III. Silicon Carbide by Plasma Enhanced Chemical Vapor Deposition

3.0 Introduction

This chapter discusses the processing by plasma enhanced chemical vapor deposition (PECVD) of the silicon carbide (SiC) layer for the spallation test couples. Enclosed is a brief general review of the literature regarding PECVD of SiC. This is followed by a description of the equipment used in this work and the general processing procedure. Three aspects of process development are then treated in detail: deposition uniformity and homogeneity and film stress. Each of these three subjects are examined in some detail in a short literature review followed by experimental results and a discussion of how these results affect the choice of processing parameters for laser spallation couples. In conclusion, we will present how we were able to process homogenous, uniform, low stress SiC coatings of several micron thickness.

3.1 Literature Review Regarding PECVD of SiC

3.1.1 An Overview of Plasma Enhanced CVD

Plasma enhanced chemical vapor deposition is a glow discharge process whereby the energy needed for chemical reaction is supplied through high energy electrons rather than by thermal activation. A glow discharge is created when applied high frequency power accelerates the few free electrons found in any gas. When these electrons gain sufficient energy, they may cause dissociation, ionization, or excitation of gas species

upon collision. Ionization events create more free electrons which are in turn accelerated and contribute to further breakdown of gas species. This collision cascade continues until the rate of electron and ion production equals the rate at which free electrons and ions are lost to surfaces or in recombination events. PECVD processing has been reviewed by a number of authors [10-13].

A steady state plasma for a two electrode system is shown schematically in Figure 3.1a and the voltages for this situation are shown in Figure 3.1b. Note that the potential of the plasma is more positive than any surface in contact with it. (For our system the plasma voltage for typical processing parameters is +15 volts while the upper electrode would be at -500 volts. The floating potential at the lower electrode is +3 volts.) This is because electrons are much more mobile than the relatively massive ions and diffuse more easily out of the glow. This potential between the plasma and electrodes accelerates ions into the electrode creating a bombardment of the surface and a generation of Auger electrons which are accelerated back into the plasma. These auger electrons have very large amounts of energy and dramatically affect the electron energy distribution of the plasma. The electron energy distribution plays a central role in the plasma chemistry, while ion bombardment of the surface greatly effects surface reactions and film properties and will be discussed in more detail below.

Specification of a plasma state involves knowledge of electron concentration and energy distribution, reactant concentrations, and residence time. These parameters are extremely difficult to determine; therefore, plasma processes are more often described in terms of macroscopic properties which include rf power and frequency, gas types

and flow rate, pump speed, reactor geometry, and electrode temperature, material, and potential for the purpose of specifying the conditions for a successful deposition process. These macroscopic parameters interrelate to determine the above microscopic properties.

Power affects the electron concentration which in turn determines the degree to which the gases are dissociated [14, 15]. Therefore, increasing the power increases the plasma potential as well as the number density and energy of the ions. Power and pressure together largely determine the electron energy distribution. Increasing the pressure lowers the electron energy, broadens the energy distribution, and decreases ion flux to the substrate [16, 17]. These pressure effects result from increased collisions at higher pressure. Generally, the best quality films used in microelectronics applications have been deposited at low pressures and low powers where there is low depletion of the process gases [13, 18].

While pressure and power are process variables that largely influence gas phase processes, substrate temperature primarily affects surface reactions. Higher substrate temperatures enhance surface reactions and product desorption leading to lower hydrogen film content, higher density and increased chemical stability [19]. Higher substrate temperature has also been linked to low oxygen contamination in films [20].

While not a process parameter like pressure or power, ion bombardment of the growing film is important and needs to be mentioned in its own right. Ion bombardment influences nucleation, growth kinetics, film composition, structure and stress [10]. Ion bombardment enhances desorption and often provides the necessary activation energy for etching processes [12]. It also increases surface adatom mobility, and if it is of sufficient intensity, may induce an amorphous to crystalline transition in

the growing film. In general, increased bombardment leads to higher film density and stress and decreased hydrogen content in most materials.

The entire deposition process consists of several steps: delivery of gas to the glow discharge, decomposition of the gases to form ions, excited species and neutral radicals, diffusion of these reactive species to the surface region, adsorption of the species to the surface, reaction at the surface to form the growing film, desorption of reaction products, and flow of these products away from the surface region; however, the process can basically be divided into two main steps: reaction of species in the plasma and reactions at the growing film surface. A successful model must have values of all rate coefficients for plasma chemistry and surface reactions. Because of the lack of information regarding these processes, complete models do not exist. The processes are instead described in terms of dominant reaction mechanisms.

3.1.2 Silane and Methane Based Plasmas

Quadrupole mass spectroscopic studies have shown that silane and methane tend to break down independently of each other, primarily forming SiH_2, SiH_3, CH_2 and CH_3 [21]. Their ions do react with each other, but as ions compose only one part in ten thousand of the gas species, neutral free radicals are the most important supply of species for the growing film [12, 22]. Therefore, silane and methane plasma reactions may be considered independently. (Ions are important to the deposition process in that they bombard the growing film, but their material contribution to the growing film is small.)

Discussion of silane reactions in the glow discharge processing of silicon films has resulted in some controversy. There are two theories

regarding the dominant mechanism of deposition. Robertson and Gallagher have proposed a model based on SiH_3^+ radicals [12, 23-26] and Veprek has proposed a model based on the SiH_2 radical [27-32]. Ross has given an excellent summary of the dispute [33] and before the controversy even started Haller [17] suggested that each mechanism may be dominant in different power/pressure regimes.

At low pressure and power it is likely that the processes based on SiH_2 production dominate. This deposition model is as follows: electron impact dissociates silane into SiH_2 and H_2. The SiH_2 immediately reacts with another silane molecule to form disilane, Si_2H_6. Disilane may also react with another SiH_2 radical to form higher silanes. Disilane and higher silanes decompose on the surface under the impact of ion bombardment. These reactions are shown below:

$$SiH_4 + e^- \; \text{---}> \; SiH_2 + H_2 + e^- \tag{1}$$

$$SiH_2 + SiH_4 \; \text{---}> \; Si_2H_6 \tag{2}$$

$$Si_2H_6 + SiH_2 \; \text{---}> \; Si_3H_8 \tag{3}$$

$$Si_2H_6 \; \text{---}> \; 2Si(a) + 3H_2 \tag{4}$$
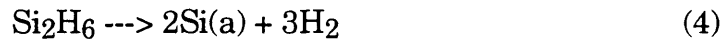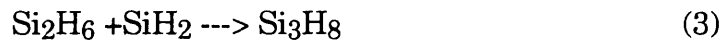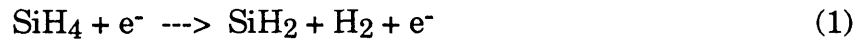
Reaction 1 is controlled by the electron energy distribution, reaction 2 may be considered instantaneous [31], and reaction 4 is controlled by ion bombardment, so that if reaction 4 is not fast with respect to reaction 1, powder is formed.

Methane dissociation in glow discharges has been studied by several workers [15, 22, 34, 35]. Rudolph [22] identified five dissociation reactions, with decomposition, primarily to CH_3 and CH_2 radicals, and Tachibana [34] listed a remarkable 56 possible radical reactions! The dominant radical reaction product depends on dilution gas and was found to be C_2H_2 with argon and C_2H_4 with hydrogen with C_2H_5 and C_2H_6 also present in each

[22]. The majority of evidence indicates that neutral radicals are responsible for the bulk of the deposition suggesting an ion bombardment enhanced model as for silane.

When mixing silane and methane in a plasma, several factors should be taken into account. Methane is more difficult to decompose in a plasma than silane [15] and CH_n radicals have lower sticking coefficients than silane based radicals [35]; therefore, it is necessary to have more methane than silane in the plasma to get an equal amount of silicon and carbon in the film. The much stronger attachment of hydrogen to methane is also the reason that the hydrogen content in the film is determined by the methane content of the plasma. Generally, the development of silane and methane based plasma processes in practice has been qualitatively guided by the above discussion with the particulars worked out empirically.

3.1.3 Structure and Properties of Amorphous SiC

The structure of silicon carbide deposited by plasma enhanced processes has been studied by transmission electron microscopy, infrared analysis, magnetic resonance and x-ray photoelectron spectroscopy and has been found to be an amorphous, hydrogenated, highly cross-linked network with a large number of tetrahedral sp^3-type bonds [22, 35-42]. This structure has been shown to have voids from 10 to 60 angstroms in diameter containing molecular hydrogen under extremely high pressure [36, 37, 43]. This pressure has been related to film stress and will be discussed further below. Because of this variability in density, SiC films have been produced with modulus values ranging from 5 to 95 percent of bulk SiC [44]. Amorphous SiC also has a high hardness and high chemical stability [40]

and has optical, electrical and mechanical properties which vary smoothly with carbon concentration [41-43].

3.2 The Plasma Enhanced CVD System

The original plasma enhanced CVD reactor system used for this work was designed and constructed by Landis [44]. The equipment has since been adapted and expanded to deal with new situations as they arose. These alterations are discussed in this chapter as they become applicable.

The chamber is 12 inches high, 18 inches in diameter and shown schematically in Figure 3.2. There are two rf electrodes 6 inches in diameter separated at a distance of 2.5 inches. The system has two main pumping systems. Initial pumping is accomplished with a Leybold™ 450 liter/second turbo-pump backed by a Leybold™ 0.5 liter/second (D90AC) mechanical pump. The system may also be pumped with a CTI eight inch cryo-pump which is located directly behind the main chamber and valved-off from the main system with a gate valve. Process gases are processed solely through the turbo/mechanical pump combination as accumulation of some process gases, particularly silane, at the cold head would be extremely dangerous. The gate valve at the cryo-pump is interlocked with the gas delivery system in such a way that the process gas shut-off valves are closed as long as the cryo gate valve is open.

Process gases are introduced into the system through a MKS™ series 260 control system. For the deposition of SiC, silane, methane, hydrogen and argon were used. Processing pressures were controlled with a MKS™ type 220B Baratron™ interfaced with a solenoid controlled butterfly valve.

The plasma is produced using 13.56 MHz power which may be supplied to either or both of the electrodes. The power supply for the upper

electrode is a RF Plasma Products™ HFS 501 component, while the supply

for the lower electrode is a HFS 251. While the power supplies require an

impedance of 50 ohms, the impedance of the plasma changes with

processing conditions. Therefore, a matching network composed of

variable capacitors and inductors is placed in series between the power

supplies and the electrodes. These capacitors and inductors are

manipulated so that they, in conjunction with the plasma, "show" the

power supplies 50 ohms. This is important because once a level of supplied

power is set and the plasma is "matched", the rf and dc voltages at the

upper and lower electrodes are then fixed and are no longer variables. A

more extensive description of the rf power system may be found in the

thesis of Landis [44]. Voltages at both the upper and lower electrodes were

measured with a SEV-2DC feedback controller.

The system as constructed by Landis had a differentially pumped

quadrupole mass spectrometer mounted below the lower electrode with a

small aperture between the plasma and the quadrupole. As it was

desirable to obtain thicker coatings at higher temperatures, this

instrument was removed and a heating element was installed in its place.

The heated electrode assembly is shown schematically in Figure 3.3. Note

that the heating element is made of molybdenum and that the lower

electrode plate is composed of graphite. NiChrome heating elements had

extremely short lifetimes and the stainless steel electrode plates were poor

conductors of heat. The thermocouple shown in Figure 3.3 is the control

thermocouple. Reported processing temperatures are from this

thermocouple.

The lower electrode alteration included a change in the way in which

rf power is supplied to the lower electrode. A schematic of the methods of

power supply before and after the alteration is shown in Figure 3.4. Before the heater was in place, power could be supplied to an electrically isolated fixed plate (marked in Figure 3.4b) to which the transfer (or electrode) plate simply was mounted. This lower plate impeded heat flow from the heater to the electrode plate and was, therefore, eliminated. Power is now supplied by a spring-loaded finger that presses against the side of the electrode plate. It was important to remove deposited coatings from the end of this finger regularly as the deposits affect the supply of power to the lower electrode surface.

3.3 General Processing Procedure

The general processing procedure was as follows: the system was pumped down to less than 5.0×10^{-6} torr and the lower electrode was heated to the processing temperature while the graphite lower electrode plate sat on the heater. Hydrogen and argon were introduced into the chamber and a plasma was struck. This was to clean the electrode surfaces. The exact processing parameters are shown in Table 3.1; these parameters were determined through experiments described in subsequent sections. After a 15 minute clean up period for the electrode surfaces, the lower electrode plate was withdrawn back into the load lock ready for the specimens.

Sapphire substrates were first dipped in tri-ethane, then acetone, and then placed for 2 minutes in methanol. Silicon wafers were cleaned with methanol, then dipped for 15 seconds in a 10 percent hydrofluoric acid in ethanol solution, and blown dry with nitrogen, following Herbots and coworkers [45]. The cleaned specimens were placed on the graphite lower electrode plate in the load lock and the plate was transferred to the main reactor chamber. The system was pumped down to 2.0×10^{-6} torr with both

the cryo and turbo pumping systems. The gases required for deposition were then introduced into the chamber and deposition began with the striking of the plasma. Typical deposition rates ranged from 10 to 30 nanometers per minute. The exact processing parameters for the SiC used in the production of spallation specimens are also displayed in Table 3.1. The methods by which these parameters were derived will be discussed later in this chapter.

Table 3.1 Processing Parameters for the Deposition of SiC

	Cleaning	Deposition
Time	15 minutes	3 hours
Temperature	300°C	275°C
Pressure	100 μm	50μm
Gas Flow		
SiH$_4$	---	1.8 sccm
CH$_4$	---	2.9 sccm
Ar	20.0 sccm	---
H$_2$	20.0 sccm	---
Upper Electrode		
Incident Power	100 watts	25 watts
DC Voltage	-450	-350
RF Voltage	-560	-240
Lower Electrode	floating	floating
Incident Power	---	---
DC Voltage	+8	+3
RF Voltage	-22	-12

3.4 SiC Process Development

3.4.1 Uniformity of Deposition

As the system electrodes are 6 inches in diameter and most of the substrates coated were 1 or 2 inches in diameter, it was possible to coat several wafers at once. Questions arose regarding the uniformity of coating thickness across the electrode surface. Uniform deposition for parallel plate PECVD reactors is achieved by balancing several factors which determine reaction rates including residence time, reactant concentration, and electron density [12, 14]. Residence time and concentration both decrease as the gas flows across the substrate while the electron density increases as the center of the electrode is reached. Gradients are kept to a minimum when input gases are depleted only slightly [46].

The spatial distributions of electrons and reactants are not easy to measure; however, the process variables, pressure and power, which dramatically affect the above parameters are easily controlled. If the power input to the plasma is large, there will be large gradients in concentration. Also if the pressure is too high, reactions will be much faster in the gas phase than on the substrate surface. Decreasing the power and pressure, however, decreases the deposition rate and thus increases deposition time.

Uniformity results are shown in Figures 3.5 and 3.6 where film thickness is plotted with respect to the radial distance from the center of the electrode. Three different input powers are shown in Figure 3.5 and three different pressures are shown in Figure 3.6. From Figure 3.5 it may be seen that the deposition is very uniform if the applied power is less than 30 watts. Interpretation of Figure 3.6, however, is less straight forward. It is apparent that at 100μm pressure the thickness varies greatly over small

length scales, so much so that the effect over the longer distances is not clearly visible. Sinha, et al. found that uniformity was poor at 100µm [47]. Local variation due to particle nucleation will be discussed in the next section. The 50µm curve shows a similar surface roughness, but the 30µm pressure deposition shows a smooth surface. It was unfortunate that 50 watts was chosen as the input power for all three deposition pressures as the previous Figure 3.5 has shown that the deposition is nonuniform at 50 watts over the electrode distance. These curves show that for processes at 30 watts or less at 30µm pressure, deposition will be very uniform over the length of the electrode.

3.4.2 Suppression of Particle Formation During Processing

A serious problem that was solved in the course of this work involved the formation of sub-micron sized particles in the plasma. These particles would embed themselves in the growing film and act as stress concentrators during laser spallation experiments so that the film failed before the coating/substrate interface. Particles in a sample coating are shown in the photomicrographs in Figure 3.7. In Figure 3.7b. the effect of the particles upon spallation may be seen as fracture withing the coating rather than at the coating / sustrate interface.

This phenomenon is called plasma particle generation or plasma polymerization and has been reported in both silane and methane based plasmas [15, 16, 22, 28, 48-51]. Particle contamination occurs when species created in the plasma react much more rapidly with each other than at a surface. Nuclei resulting from these reactions are usually charged and thus remain held in the plasma until they grow to be very large [52].

Unfortunately, while many workers will report this as a problem, solutions are not usually stated or only referred to vaguely.

Suppression of particle generation requires either impeding plasma reactions or enhancing surface sticking coefficients or both. Lowering the power will decrease the density and energy of electrons and thus produce fewer ions and radicals. Lowering the pressure decreases the number of collisions a reactive specie would suffer before encountering a wall. Increasing the flow rate reduces the residence time in the plasma. Diluting the plasma reduces the number of reactive collisions and changing the dilution gas alters the plasma electron energy distribution [15, 50].

All of the above process changes were successful to some degree; however, attempts at completely eliminating powder formation were unsuccessful until hydrogen was used to replace argon as the carrier gas. It was finally determined that use of hydrogen as the carrier gas with silane concentration at no more than 10 percent would not yield particles at 50 microns pressure and 100 watts power, but this would still allow deposition rates of nearly 60 nanometers per minute.

It should be noted that argon was unacceptable as a dilution gas. Spears, et. al. [48] detected particles trapped in the glow discharge via laser light scattering in gas plasmas as dilute as 0.1 % silane in argon with as little as 3 watts power. Knights, et. al. [50] found that argon dilution led to coatings with high void densities under all discharge parameters while others [49] showed that the reactive sticking coefficient of silane radicals was generally much larger in hydrogen than in argon based plasmas. Similar results were also found in methane-argon and methane-hydrogen plasmas where Rudolph and Moore [22] determined through mass

spectroscopy that while hydrogen dilution led to radical formation with nearly saturated carbon bonds and very little polymerization, argon dilution was shown to lead to unsaturated bonds permitting rapid polymerization. Roca i Cabarrocas [16] and Tachibana, et. al. [15] give some explanations for the favorable performance of hydrogen as a carrier gas. The former showed a large increase in ion energy and ion flux in silane-hydrogen plasmas which would increase the reactive sticking coefficient of neutral radicals. The latter showed that argon and hydrogen plasmas had significantly different electron energy distributions leading to much higher degrees of dissociation in argon plasmas.

Even after hydrogen was used as a dilution gas, test specimens continued to show particles in the films. These particles, however, were not produced in the plasma. The wafers were being sectioned into quarters by scoring them with a diamond-tipped pen. They would break nicely along the scratch; however, this process would generate a fine silicon dust that would stick to the pieces even after long ultra-sonic cleaning processes. Once this phenomenon was discovered, wafers were not sectioned until after all process steps were completed.

It was concluded that suppression of particle growth required the use of hydrogen gas with the silane gas concentration not more than 10 percent. In addition, the supplied power must be below 100 watts with the pressure below 50μm. Finally, there must also be no abrasion of the wafer in the vicinity of the test surface.

3.4.3 Residual Stresses in Coatings

3.4.3.1 Literature Review Regarding Stress in Films

Stresses in SiC [53-56], SiN [46, 47, 57-65], and SiO [59, 61, 62, 66] films produced by PECVD have been extensively studied. Stress in these coatings was found to vary over a great range from highly compressive to highly tensile and to depend on such processing parameters as substrate temperature, power supplied to the plasma, frequency of this power, electrode spacing, gas pressure, flow rate, and composition, and length and temperature of post-deposition anneals. The effects of these processing parameters on film stress were explained in terms of their effect on ion-bombardment, hydrogen incorporation and evolution, and bond relaxation and rearrangement.

These studies point to three main sources of stress in coatings. The first arises from the mismatch in thermal expansion between the substrate and the coating; this stress is usually small compared to other stresses in plasma processed coatings. The second source of stress in plasma processed coatings originates from a "peening" effect in which bombarding ions implant themselves below the surface of the growing film or strike surface atoms and push them deeper into the film causing a compressive stress in the coating [57, 67]. The third source of stress in coatings arises from the incorporation of hydrogen in the growing film [54].

Substrate temperature during processing is one of the most important parameters affecting stress in coatings. Film stress PECVD coatings is usually reported as compressive at low temperatures becoming linearly more tensile with increasing substrate temperature with a cross-over temperature at which the stress in the coating changes from compressive to tensile. This cross-over temperature has been reported as

400°C for SiC by Windischmann [53] and 580°C for SiN by Classaan et al [46]. However, it should be noted that Srinivasan, et al [59] reported the opposite effect of substrate temperature for silicon nitride coatings. Stresses were tensile at low deposition temperatures becoming more compressive as the substrate temperature was increased with a crossover temperature of 450°C at 130 watts.

While the substrate temperature does affect the stress due to thermal mismatch between the substrate and coating, for plasma processed coatings, the temperature mainly affects the stress due to the incorporation of hydrogen into the growing film. The desorption rate of hydrogen from the surface is influenced by the temperature and also by ion bombardment. If the film grows relatively fast compared to the hydrogen desorption, hydrogen is trapped in the film resulting in a compressive stress. On the other hand, when the film grows slowly compared to hydrogen desorption, the coating collapses behind the growth front and there is a tensile stress in the film. Beyer et. al. [68] have shown by infrared analysis that incorporated hydrogen is in both bonded and molecular states. Bonded hydrogen terminates silicon and carbon bonds at interior surfaces. Molecular hydrogen primarily resides in microvoids [36, 37, 69, 70] and Budhani et. al. [71] have shown through infrared analysis that it is molecular hydrogen, not bonded hydrogen, that is the main contributor to residual stresses in the coating.

If the voids are assumed to be like bubbles of a spherical shape, the stress field around an individual void is given by Timoshenko [72]. And if bubble changes of shape due to the stress field generated by the neighboring bubbles are neglected, and gas pressure is assumed to be the same in all voids, the resulting stress field at each point in space could be found as an

algebraic sum of all stress fields at this point. Residual stresses, generated by the sums of all bubbles in the coating, would scale linearly with the pressure of the trapped gas . The pressure of the trapped gas is linearly proportional to the mass of trapped gas. Therefore, if the hydrogen desorption is proportional to temperature, desorption effects alone would account for the linear response of stress to surface temperature during deposition.

Pressure, plasma power, electrode spacing and rf frequency are also important parameters affecting the stress in the coatings and are usually linked to their effect on the ion bombardment of the surface. Higher powers and lower pressures yield greater ion bombardment intensities and thus higher compressive stresses. Smaller electrode spacings also yield higher ion bombardment intensities. Srinivasan, et. al. [59] reported stresses ranging from 200 MPa at 100 watts to -2.9 GPa at 350 watts, and Aite, et. al. [61] reported stresses ranging from -400 MPa at 1500 mtorr to -2.2 GPa at 100 mtorr. In another system Aite [62] found that stress decreased from 200 MPa at 1800 mtorr to -400 MPa at 700 mtorr with zero stress at 1300 mtorr. Aite also showed that stresses decreased with electrode spacing from -1.05 GPa for a 15 mm gap to -550 MPa for a 22 mm gap. The plasma frequency also effects ion bombardment. At lower frequencies both the electrons and the ions in the plasma can respond to changes in the applied voltage, while at higher frequencies, only the electrons can respond to voltage changes since the ions are too massive. Therefore, stresses due to ion bombardment decrease dramatically at higher plasma frequencies. Claassen and coworkers [46] found that the stress in SiN changed rapidly from compressive to tensile between frequencies of 4 and 6 MHz. Aite [62] has also reported this type of response to plasma frequency.

Coating stress has been shown to be a function of stoichiometry. This effect is not as pronounced as the effect of temperature, power or pressure. Aite found that film stresses increase linearly with nitrogen incorporation from -920 MPa for 18 percent nitrogen in the plasma to -1.2 GPa for 72 percent nitrogen in the plasma.

The stress in films has also been manipulated through post-deposition anneals. These anneals change the film stress by supplying energy to release hydrogen from the film. Landis [44], Windischmann [54], and Budhani [71] all showed that upon annealing, the stress in the coating may change from highly compressive to highly tensile. This has been attributed to a diffusion controlled volume change in the material. Landis reported changes from -1.0 GPa to 3.0 GPa in SiC after annealing the specimens at 600°C under vacuum and Budhani reported stress changes from -1.1 GPa to 500 MPa in SiN after similar annealing.

3.4.3.2 Stress Measurement Procedure

Stress states in coatings have been traditionally determined by measuring the deflection of some substrate material due to the presence of a deposited coating. Silicon wafers are typically used as the substrate and the deflection has been measured using light interferometry [73] or a profilometer [74].

Stress in a thin film on a substrate is calculated using Stoney's equation [67]:

$$\sigma = \frac{E_s}{6} \frac{t_s^2}{t_c} \left[\frac{1}{R_b} - \frac{1}{R_a} \right]$$

where E_s is the substrate modulus (180 GPa for a 100 silicon wafer [75]), t_s is the substrate thickness, t_c is the coating thickness, R_a is the radius of curvature of the coated wafer, R_b is the radius of curvature of the bare wafer as measured before deposition. The radius of curvature, R, is determined from the deflection, h, and the diameter, d, of the wafer:

$$R = \frac{d^2}{2h}$$

See Figure 3.8a. Stress is defined as compressive if the coating is attempting to expand against the stiffness of the substrate and tensile if it is attempting to contract. This is shown in Figure 3.8b.

Two 2 inch wafers in the polished, as received condition are shown in the photographs in Figure 3.9. These pictures were taken with a camera mounted on a Graham Optical Systems Model 400LC Plano-Interferometer. The interference fringes show elevation differences of half the wavelength of the laser light used, 316.4 nanometers. These photographs show the usual topography of prime silicon wafers. Two things should be noted. First, it may be seen that the wafer shown in Figure 3.9a is "potato chip" shaped and therefore not suited for use as a stress measuring substrate. Second, it should be noted that while the wafer shown in Figure 3.9b is appropriately concave or convex, it is not uniformly so; thus, a measurement is dependent on the direction across which the curvature is taken. Previous workers have used photographs such as these to measure across the minor or major axis in photographs taken before and after coating deposition [73]. Others made traces with a profilometer across the wafer and averaged the measured deflections [44]. Neither of these techniques alone was satisfactory for the present work; results using either technique in isolation were greatly scattered and irreproducible; however, a

combination of these techniques proved to be very reliable in measuring wafer deflection.

Using a profilometer in conjunction with an interferometer was found to be the optimum method in determining deflections of coated and uncoated wafers. Wafers were first sorted with the interferometer; only those of nearly uniform convex or concave shape were chosen for profilometry. The surface of these wafers was then marked with a single, focused (~300 mJ) laser pulse to produce an 0.5 mm diameter spot approximately 1 cm from the wafer's edge. This mark was then used to align the wafer held in a two-part jig fit to the stage of a Dektak II profilometer as shown in Figure 3.10. The inner, circular piece held the wafer at its outer periphery on a knife edge while the outer jig component fit over the circular stage of the Dektak as shown in the side view of Figure 3.10. The inner jig piece was free to rotate within the outer and was scribed with an "x" that was used to align the jig with the profilometer and with the mark on the wafer surface. The scribed "x" and the mark on the wafer are shown in the top view of 3.10.

The exact deflection measurement procedure is as follows: a glass cover slide was placed on the stage of the Dektak and the needle of the profilometer was lowered. The microscope of the profilometer was then focused so that the needle was aligned with the cross-hair in the microscope. The needle was retracted and one edge of the cover slide was aligned with the center of the profilometer stage. The x-axis travel of the stage was then adjusted until the cross-hair in the microscope was aligned with the edge of the cover slide. At this point the travel of the profilometer needle would cross the center of its stage and therefore the center of the jig and wafer as the stage, jig and wafer are concentric. The x-axis travel of

the Dektak was not moved again during the measurement procedure. The wafer to be measured was placed onto the knife edge of the jig as shown in the side view of Figure 3.10 and the Dektak needle lowered. Once again the microscope focus was adjusted so that the needle appeared at the cross hair. This is because the jig elevated the wafer and thus changed the center of focus. The y-axis travel of the stage was used while rotating the inner jig so that the cross hair crossed the scribe in the inner jig. This scribe is labeled "alignment scribe" in the top view of Figure 3.10. The stage was then moved in the y direction while the wafer was rotated so that the laser mark could be seen under the cross hairs. At this point both the inner jig scribe mark and the laser mark on the wafer were on a line passing through the very center of the Dektak stage. The stage was then moved in the y direction as far as it would go and a 16 mm scan was run across the center of the wafer. The scan line is shown in the top view of Figure 3.10. This technique allowed measurement of the same path across the wafer even after the Dektak was used by other workers.

As a test of the repeatability of this procedure the entire set up was dismantled and reassembled six times. Each time the stage and the jig were randomly skewed. The average deflection measured was 8.064 μm with a standard deviation of 0.12 μm which amounts to a 1.5 percent error. The error due to the irregular concavity of the as-received wafer was much greater. The stress as calculated in three directions on one wafer averaged -375 MPa with a standard deviation of 26 MPa which comes to a 7.0 percent error. Therefore, the effects of sequential processing on one wafer could be very accurately determined, while the effect from wafer to wafer was less accurate.

3.4.3.3 Stress as Measured in SiC

The results of the first stress measurements were confusing until it was discovered that for coatings deposited with the heating element off, the stress in the coating changed over time upon exposure to atmosphere. The stress in a standard SiC film (gas ratios as described in Table 3.1) and a carbon rich film (methane concentration 10 times that of silane) is shown as a function of time in Figure 3.11. These same results are also plotted with respect to the square root of time in Figure 3.12. Films deposited at elevated temperatures were then investigated and it was found that for deposition temperatures over 200°C the stress was unaffected by exposure to atmosphere. An example of the stress versus time scale for coatings deposited at elevated temperatures is shown in Figure 3.13.

Once the stability criterion for processing was established, the as-deposited film stress for substrates was determined for different temperatures and bias voltages. Stress versus temperature for a floating (or self-biasing) lower electrode and for a grounded lower electrode is shown in Figure 3.14. The stress is shown as a function of voltage at the lower electrode in Figure 3.15 for a substrate temperature of 400°C.

The effect of annealing upon stress was also investigated. Wafers were annealed under a vacuum of 5.0×10^{-6} torr or better for one hour at 560, 680, 790, and 900°C. Stress versus annealing temperature for various deposition temperatures is shown for coatings deposited on a grounded lower electrode in Figure 3.16 and for coatings deposited on a floating lower electrode in Figure 3.17. It should be noted that films were deposited on one wafer and then this single wafer was annealed successively at the temperatures noted in the figures. It was determined that stress changes

upon annealing were complete after one hour at 600°C and higher temperatures as is demonstrated in Figure 3.18 for the 600°C anneal.

Stress results for four different anneals of coatings processed in an identical manner are shown in Table 3.2. The deposition for each wafer was conducted at 400°C at the standard power and flow rates. The first stress is that for the standard anneal under vacuum, the second value corresponds to the stress for an anneal in an argon atmosphere, and in the third and fourth cases, the coating was processed and thereafter left in the chamber at 400°C under high vacuum after deposition.

Table 3.2 Stresses for Various Anneals for Standard SiC Deposited at 400°C

Anneal Process	Stress
Anneal in vacuum, 1 hour, 635°C	+944 MPa
Anneal in Argon, 1 hour, 635°C	+929 MPa
Sat on lower electrode, 1.5 hours, 400°C	+292 MPa
Sat on lower electrode, 1 hours, 400°C	+216 MPa

Interpretation of stresses in PECVD coatings is based on an understanding of the process/structure relationship. Phenomena to be considered are ion bombardment of the growing film, hydrogen incorporation and desorption from a growing film, hydrogen release from a grown structure, and diffusion of atmospheric species into the porous structures.

The time variant stress in the coatings shown in Figures 3.11 and 3.12 deposited at room temperature can be understood in terms of diffusion

of some species into the porous, low density, amorphous structure. That the stress becomes increasingly compressive, indicating that the coating is attempting to expand against the substrate, argues that the diffusion is into the structure. The fact that the stress changes linearly with the square root of time indicates diffusion control. The diffusing species may be either water vapor or oxygen. Since the stress does not change in coatings processed at temperatures greater than 200°C, this implies that at these higher temperatures the film produced is dense enough that the pores are not interconnected sealing off the inner surfaces from adsorbing gas species.

The dependence of stress on substrate temperature is shown in Figure 3.14 and the dependence on electrode voltage or potential is seen in both Figures 3.14 and 3.15. Figure 3.14 shows that the as-deposited stress as a function of substrate temperature becomes more tensile for films deposited on a floating electrode and becomes more compressive for films deposited on a grounded electrode. The only difference between these two processes is that the floating electrode self-biases to +2 volts, while the grounded electrode is a 0 volts. This difference does not appear to be great, but it must be sufficient to greatly reduce the effect of ion bombardment of the growing film. Ion bombardment must be responsible because only ions would be affected by the potential of the substrate. Most of the ions in the glow are positively charged and would be deflected away from the biased substrate. The temperature of the substrate must also be taken into account. As the temperature of the surface increases, hydrogen desorption is enhanced. For the floating electrode at +2 volts the hydrogen desorbs more readily at higher temperature and the ion bombardment is retarded enough that it escapes easily; as the hydrogen desorbs the dangling bonds

exposed connect with each other, but are stretched in doing so, which accounts for the increasing tensile stress with deposition temperature.

The grounded electrode phenomenon is more difficult to explain. For the grounded electrode more hydrogen is also released from the near surface regions at higher deposition temperatures, but ion bombardment must interfere with the desorption or film growth in such a way as to keep the hydrogen in the film. Ion bombardment should not retard hydrogen adsorption as it is known to enhance desorption in other systems [12]. Increasing ion bombardment does increase the compressive stress as is shown in Figure 3.15 where the stress becomes increasingly more compressive with negative substrate bias.

The effect of annealing shown in Figures 3.16, 3.17 and 3.18 can be explained in terms of hydrogen diffusion out of the film followed by thermally activated rearrangement of the structure. In all cases the stresses became highly tensile upon annealing at the lowest of the anneal temperatures, 560°C. This temperature allowed complete diffusion of hydrogen out of the submicron film in one hour. In subsequent anneals at higher temperatures the coating relaxed. This is confirmed by the results in Table 3.4. Specimens "annealed" on the lower electrode at the deposition temperature showed an increase in tensile stress from +80 MPa to +294 MPa even at 400°C and this increased with time at 400°C. It was not tested, but it is believed that given enough time at 400°C, stresses near +900 MPa could be reached. At 400°C diffusion may be sufficiently slow that 1 hour is not enough time for complete dehydrogenation. Figure 3.18 shows that at 600°C 1 hour is sufficient to release all hydrogen present, but there is not sufficient temperature for relaxation of film structure. Thus, the annealing process is composed of two steps: a diffusion controlled process

whereby the film is stretched due to hydrogen escape followed by a thermally activated relaxation of the structure.

The goal of this study of stress in SiC films was to determine the processing procedure necessary for the production of low stress SiC films of 2 μm thickness. Such films are obtained by processing the coatings at 275°C on a floating electrode. See Figure 3.14. It was not possible to produce the relatively thick, low stress coatings through a deposition/annealing process as the diffusion of hydrogen out of the coatings before relaxation always produced sufficient tensile stress to cause film delamination.

3.5 Summary

Laser spallation test couples require a relatively thick, homogenous, uniform coating. Amorphous SiC processed by PECVD has been deposited to a thickness of 2μm with a stress less than 13 MPa at 275°C on a positively biased electrode. Previous workers could not produce coatings of this thickness that did not delaminate due to internal stress [44]. Particulate formation in the plasma was suppressed by using hydrogen as a dilution gas at 0.90 mass fraction at 50 μm pressure and 25 watts power. This low gas pressure and power insured thickness uniformity better than 5.0 percent across the electrode surface.

Cathode Sheath

glow discharge

Anode Sheath

Ground Shields

Power
Supply

(a)

V_{plasma}

Voltage

$V_{Electrode}$

Ground
or
Floating
Potential

Upper
Electrode

Lower
Electrode
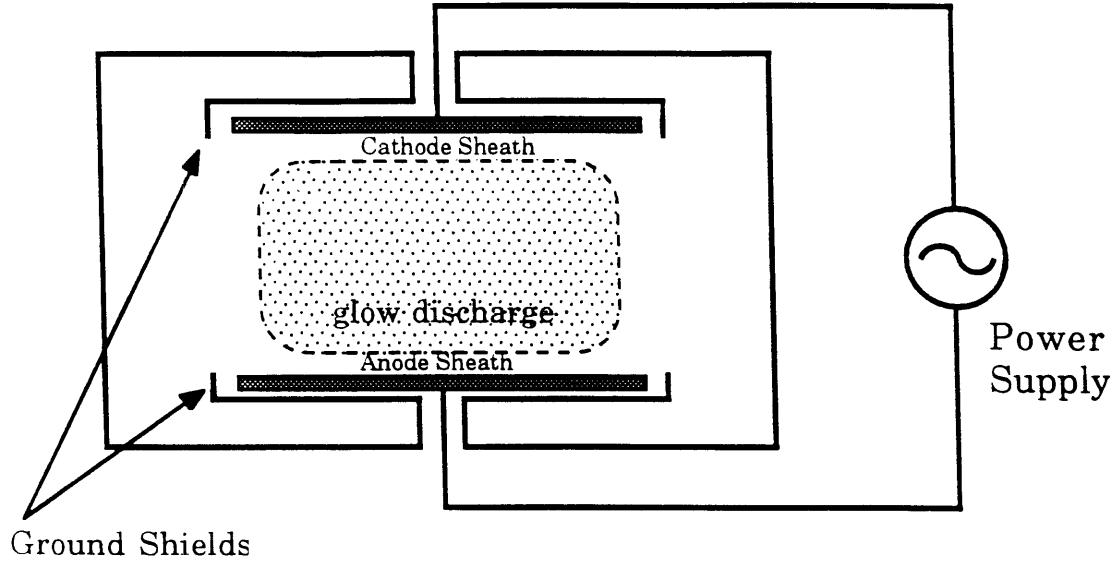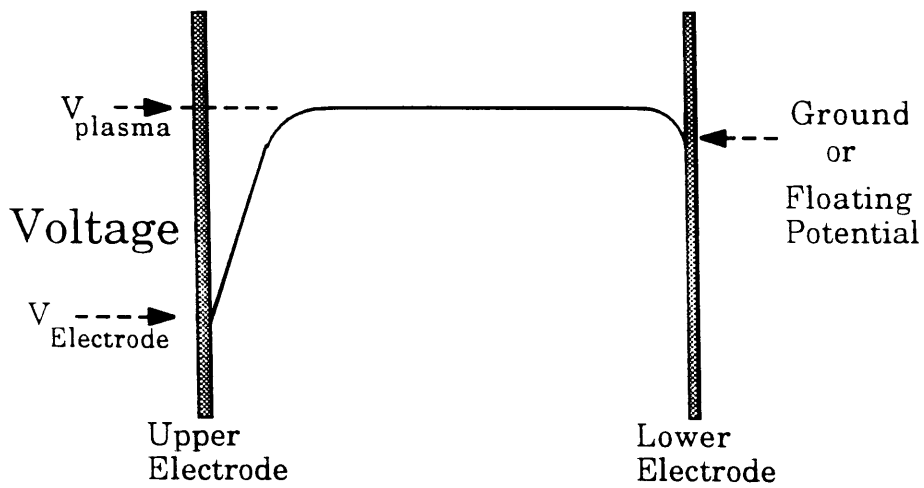
(b)

Figure 3.1 The glow discharge and voltages in plasma enhanced chemical
vapor deposition. Note that the plasma is more positive than
any surface with which it is in contact.

Cryo Pump

Upper Electrode

Gas Inlet

Load Lock

Exhaust Port

(a) Top View

Gas Inlet

Glow Discharge

Load Lock

Electrodes

To Turbo Pump
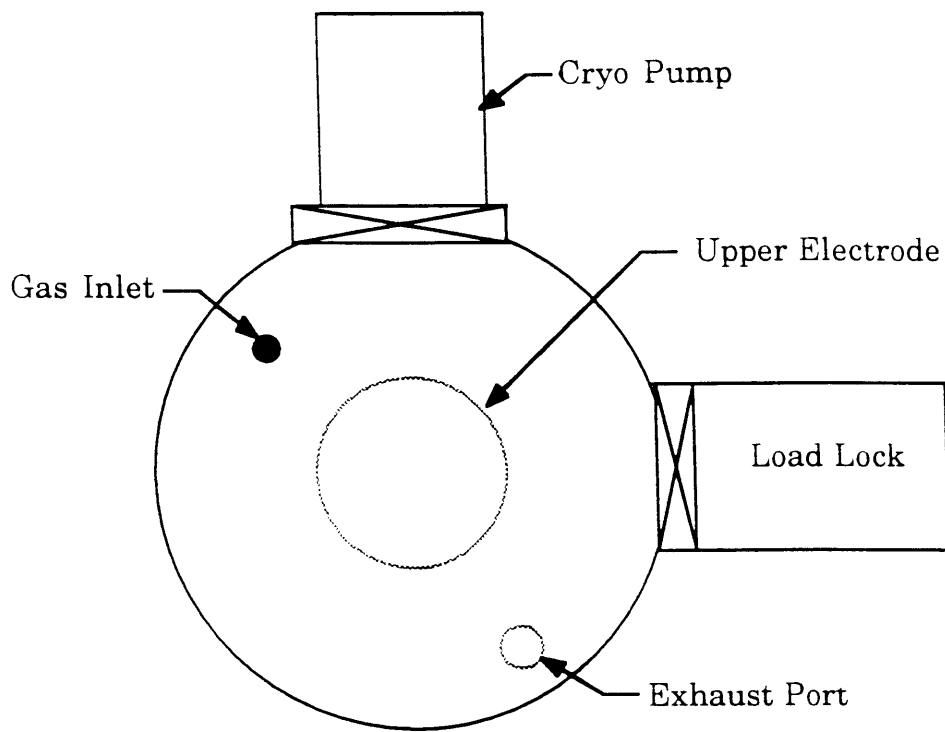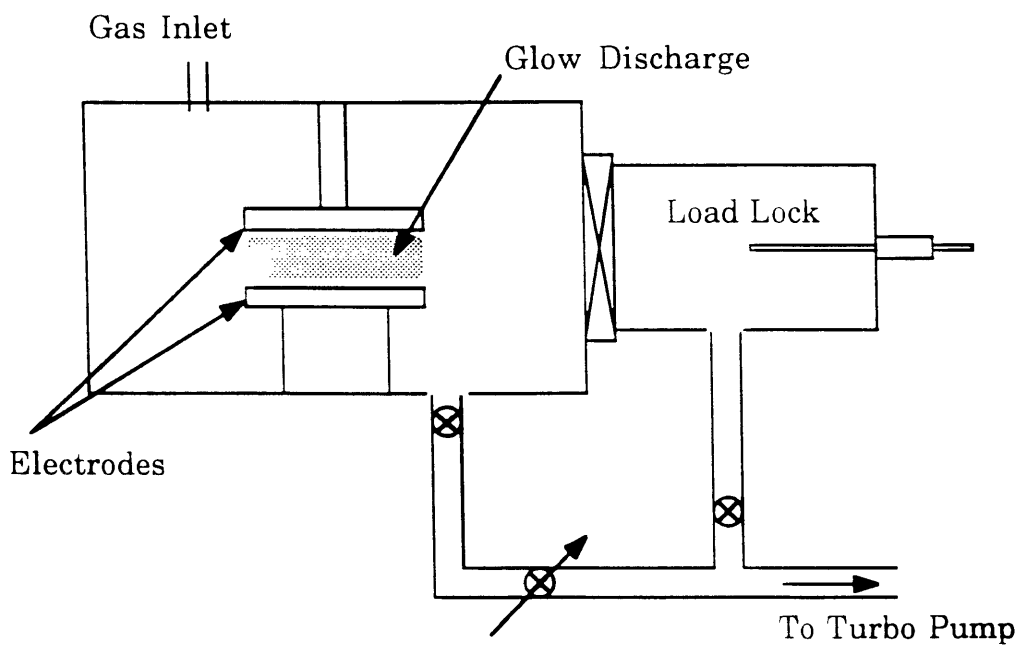
(b) Side View

Figure 3.2 Top and Side views of the plasma enhanced chemical vapor deposition reactor.
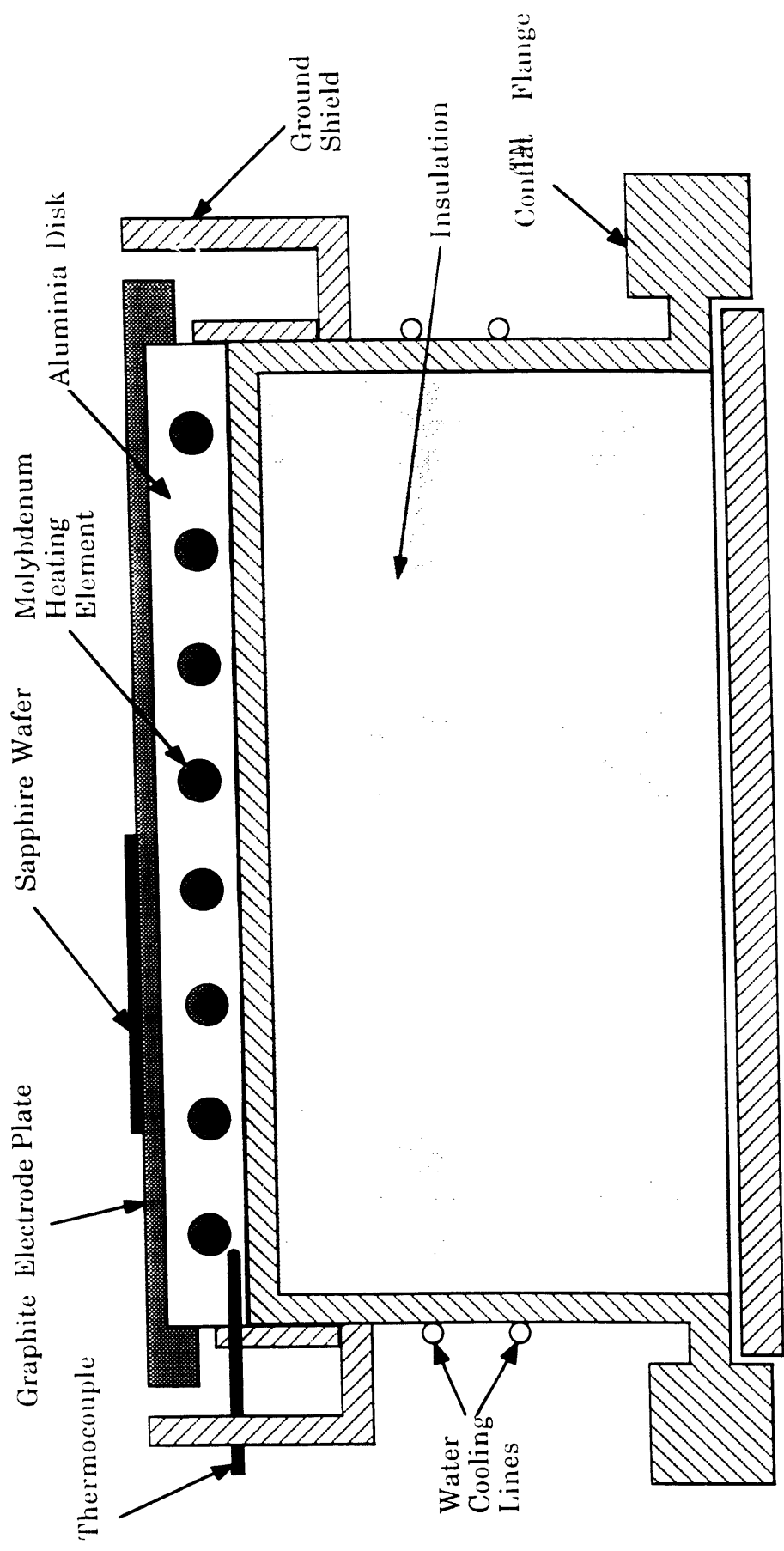
Figure 3.3. The lower electrode heater assembly with heating element installed.

56

Spring

CVD Chamber

Heater

Insulation

(a) Lower Electrode Assembly with Heating Element

CVD Chamber

Fixed Plate

Quadrupole Chamber
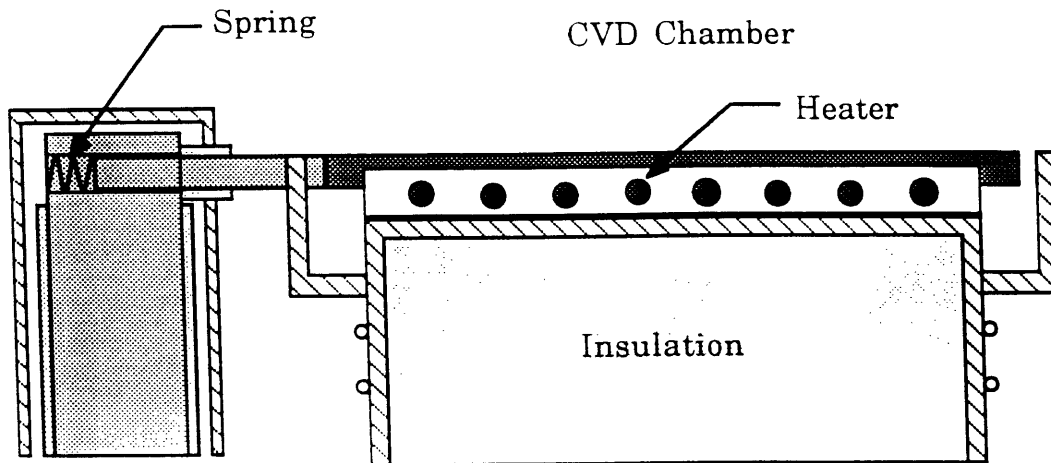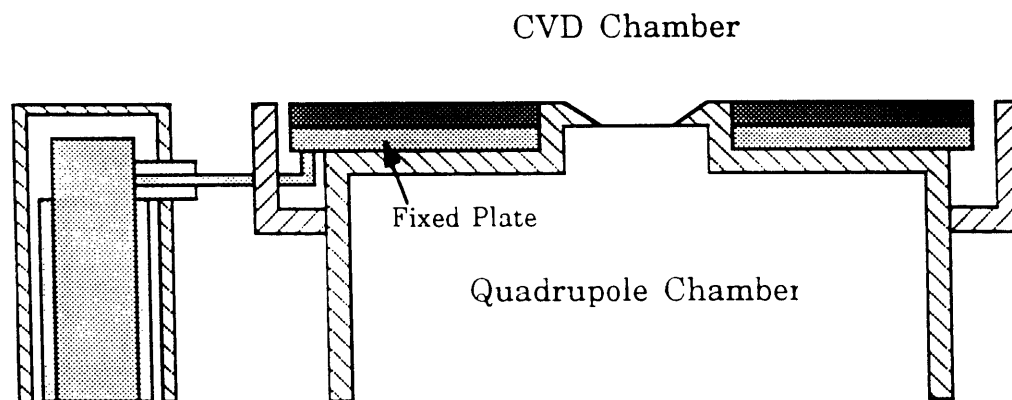
(b) Lower Electrode Assembly with Quadrupole

Key:

ground shield

electrode plate

power line

insulator
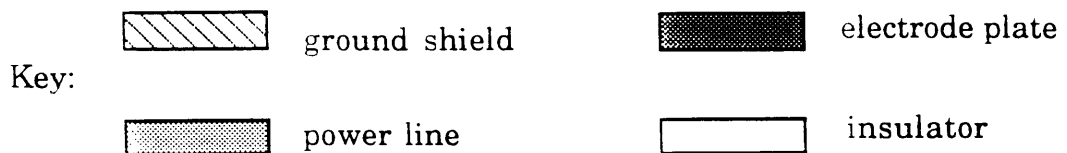
Figure 3.4 Schematics showing the delivery of rf power to the lower
electrode assembly with the heater installed (a) and with the
quadrupole mass spectrometer mounted below the lower
electrode (b).

Deposition Thickness Over the Radius of the Electrode
For Different Applied Powers
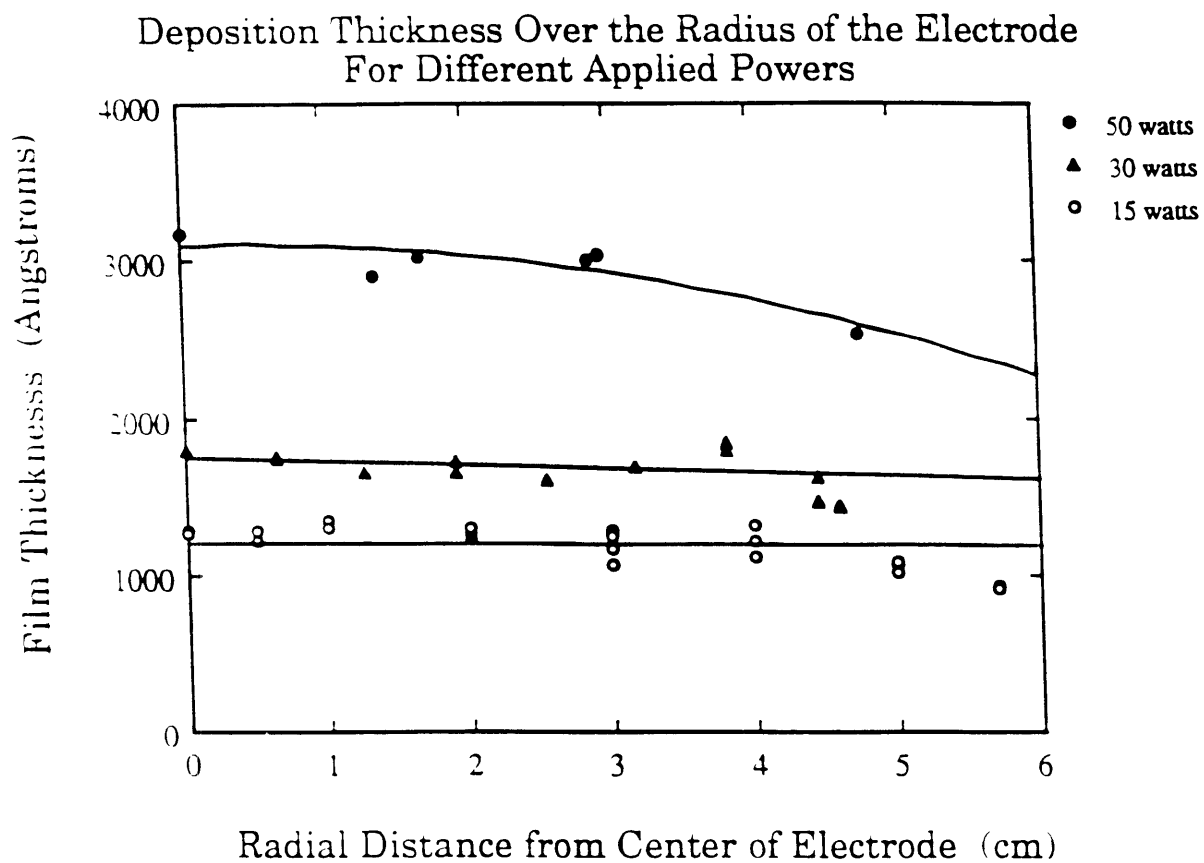
Figure 3.5 Film thickness across the radial direction of the lower electrode
for three different supplied powers with 4.2 sccm silane, 6.7
sccm methane, and 20.0 sccm hydrogen at 50 μm total
pressure.
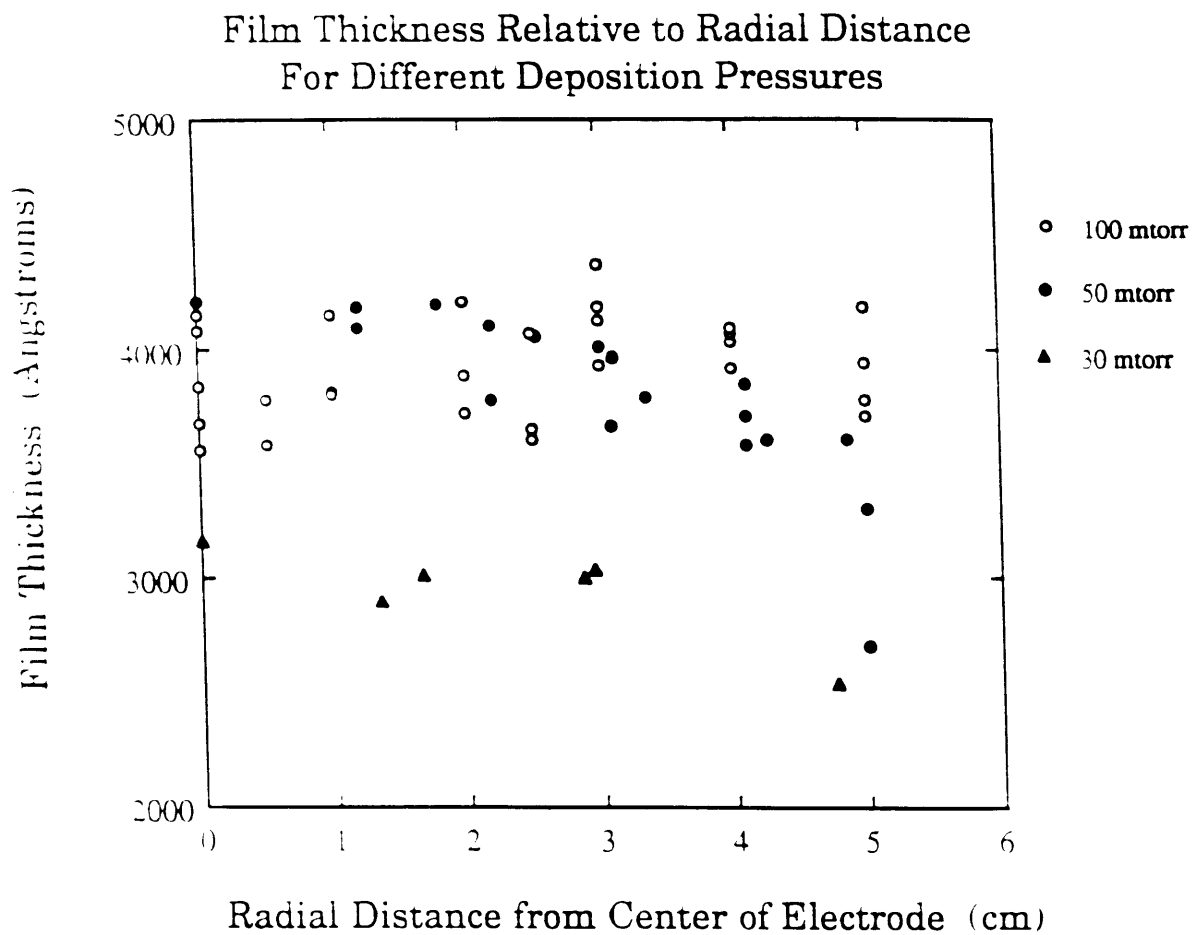
Figure 3.6 Film thickness across the radial direction of the lower electrode for three different processing pressures with 4.2 sccm silane, 6.7 sccm methane, and 20.0 sccm hydrogen. The power is 50 watts.
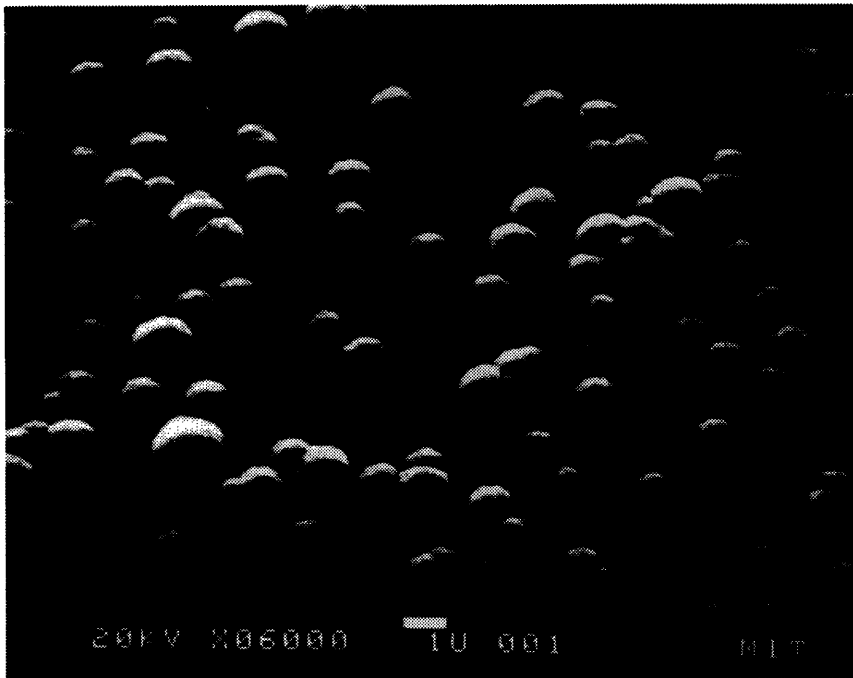
(a)
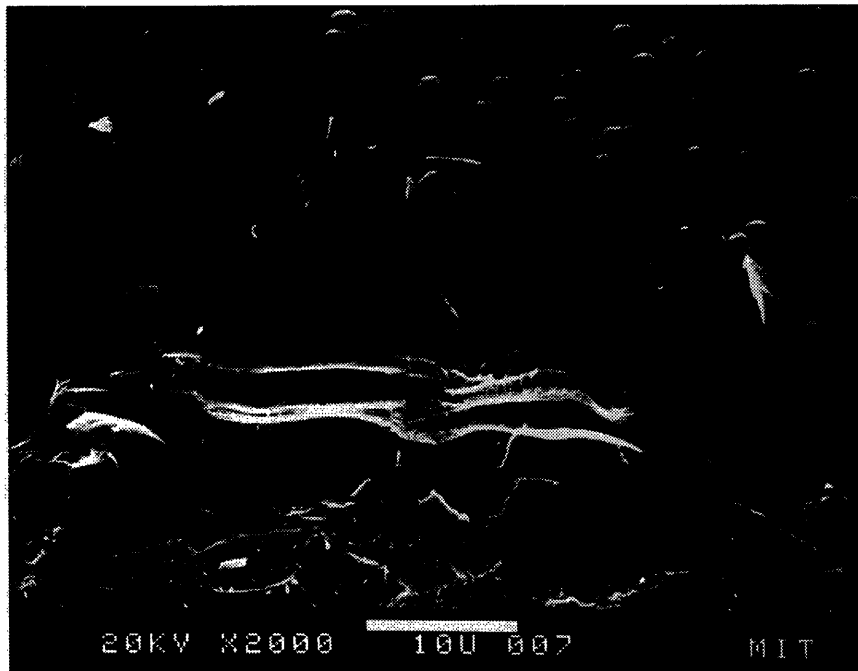
(a)

Figure 3.7   Scanning electron photomicrographs showing particles imbedded in
a SiC coating. Part (b) shows the effect of
the particles on film fracture due to laser spallation.

R. Radius of Curvature

Coating

h. Deflection

Wafer

h

Coating in Tension

Coating in Compression
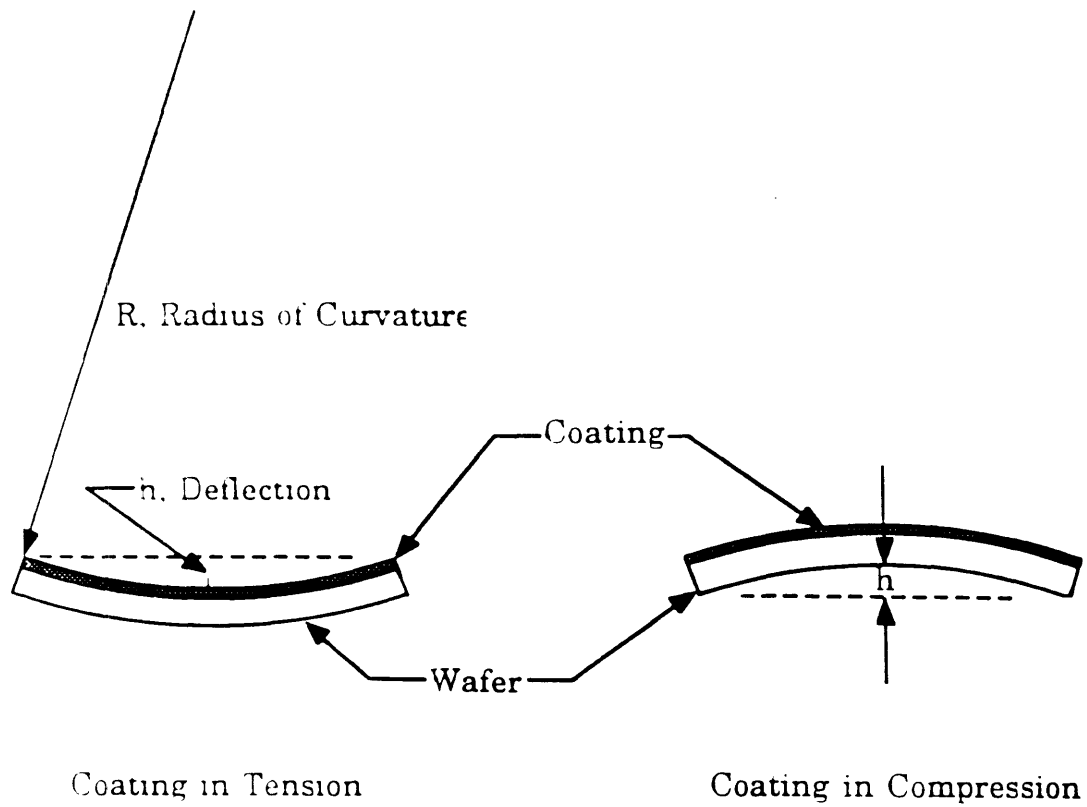
Figure 3.8 Schematic showing compressive and tensile stresses in coatings
and relevant dimensions for stress calculations.

61
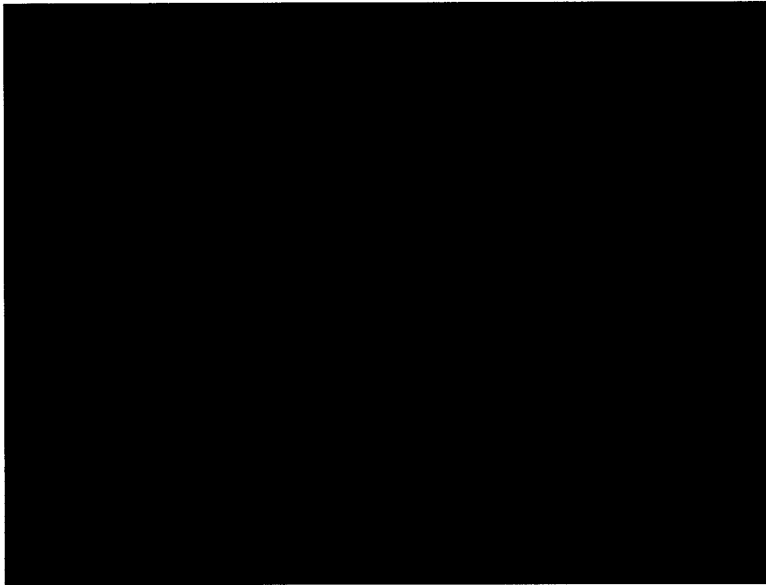
(a)
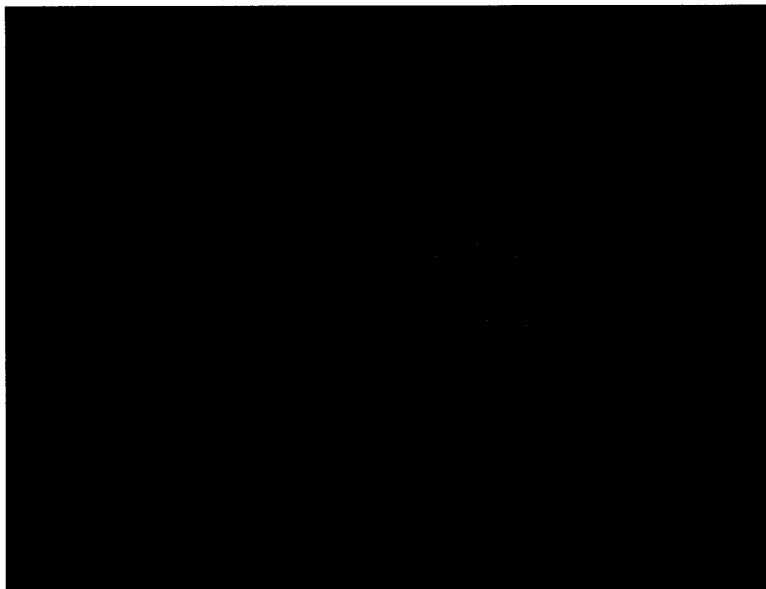
(a)

Figure 3.9 Photomicrographs with interference fringes from laser light showing the topography of concave (a) and "potato chip" (b) shaped silicon wafers.

Alignment
Scribe

Laser Mark

Wafer

Scan Line

Top View

Wafer

Knife Edge

Inner Jig

Outer Jig

Side View
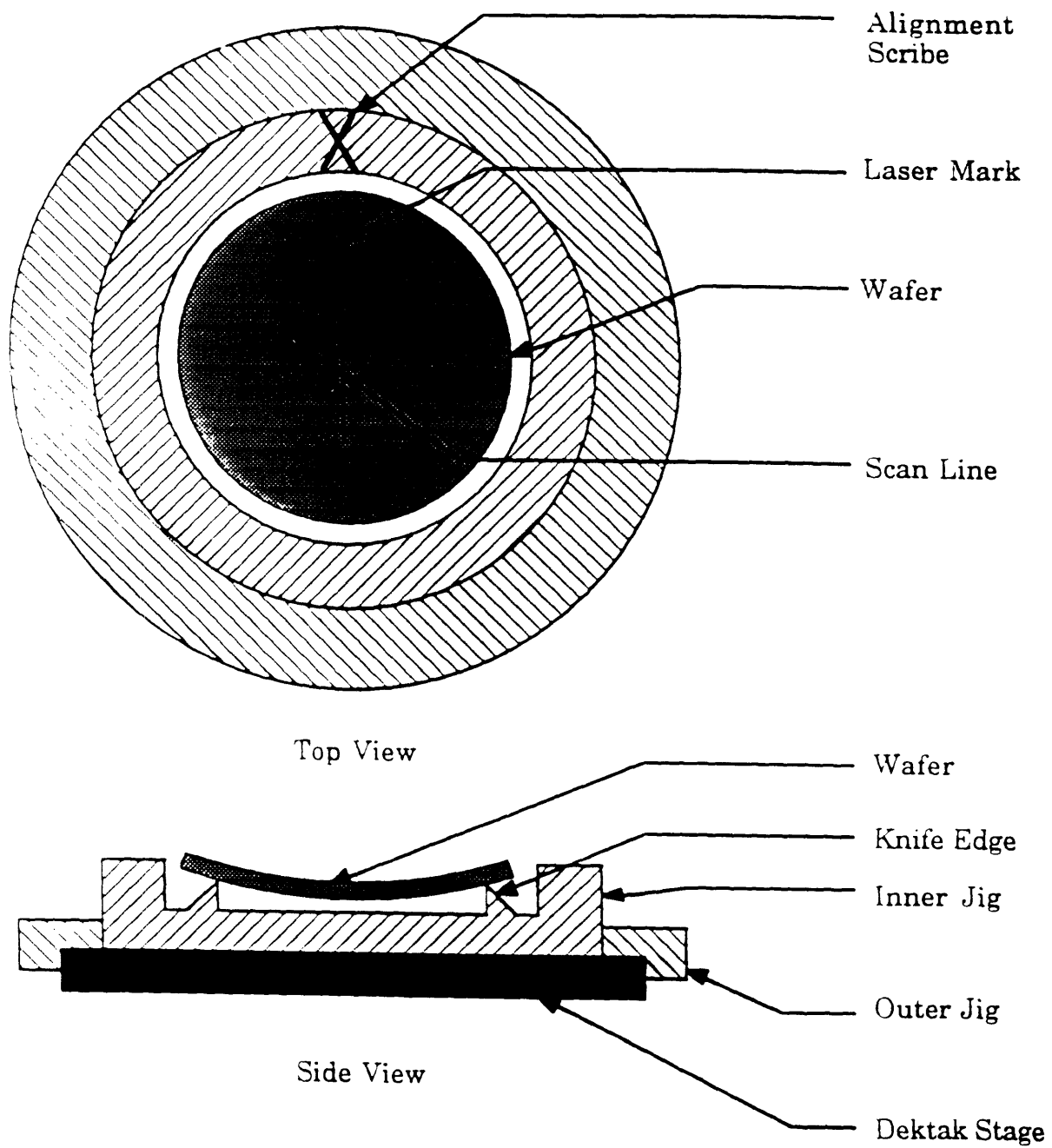
Dektak Stage

Figure 3.10 Schematic showing the jig used to hold the wafer over the
Dektak stage when measuring deflection.
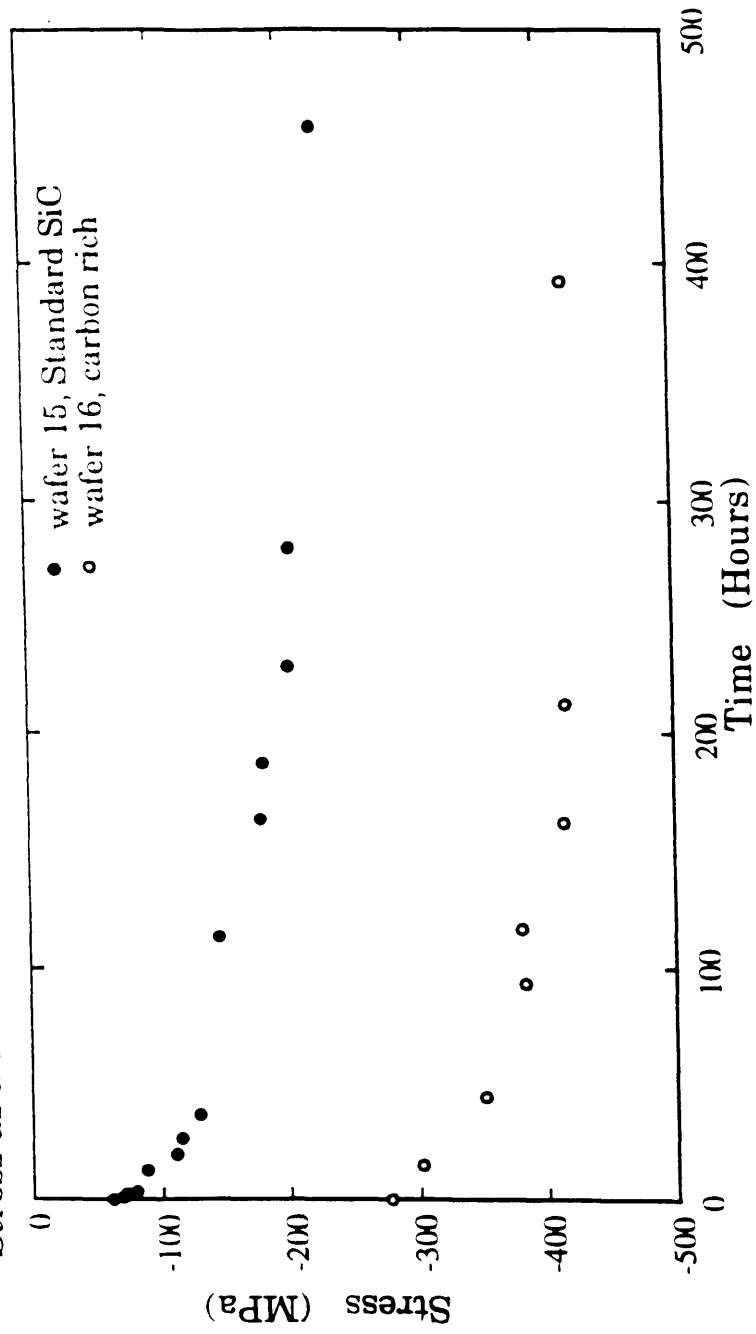
Figure 3.11 Stress as a function of time of exposure to atmosphere for standard SiC and carbon rich SiC coatings deposited at room temperature.

Stress as Square Root of Time for Coatings Deposited at Room Temperature
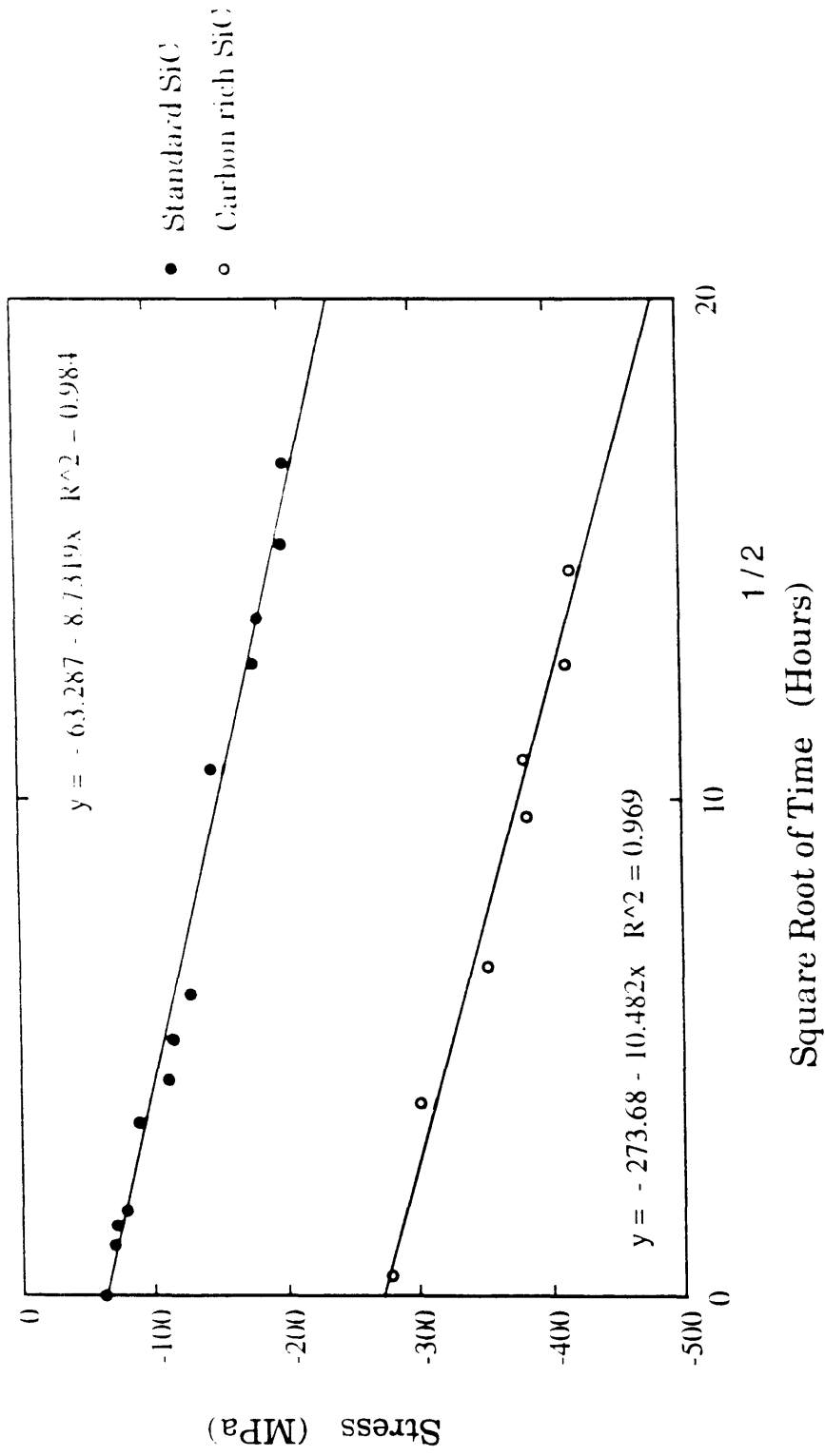
Figure 3.12 Stress as a function of the square root of time of exposure to atmosphere for standard SiC and carbon rich SiC coatings deposited at room temperature.

Stress over Time for Coatings Deposited at Elevated Temperatures
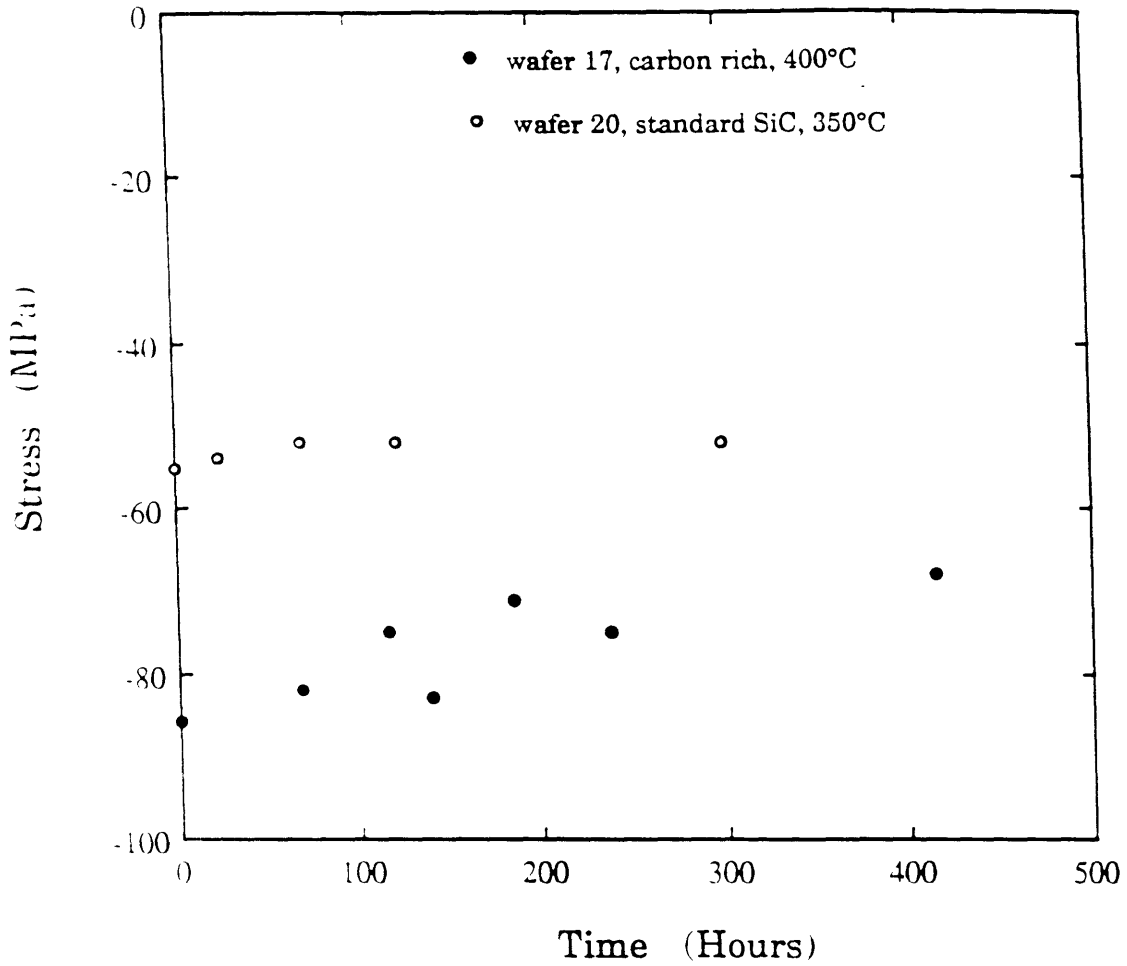
Figure 3.13 Stress as a function of time of exposure to atmosphere for standard SiC and carbon rich SiC coatings deposited at elevated temperatures.

Coating Stress as a Function of Deposition Temperature
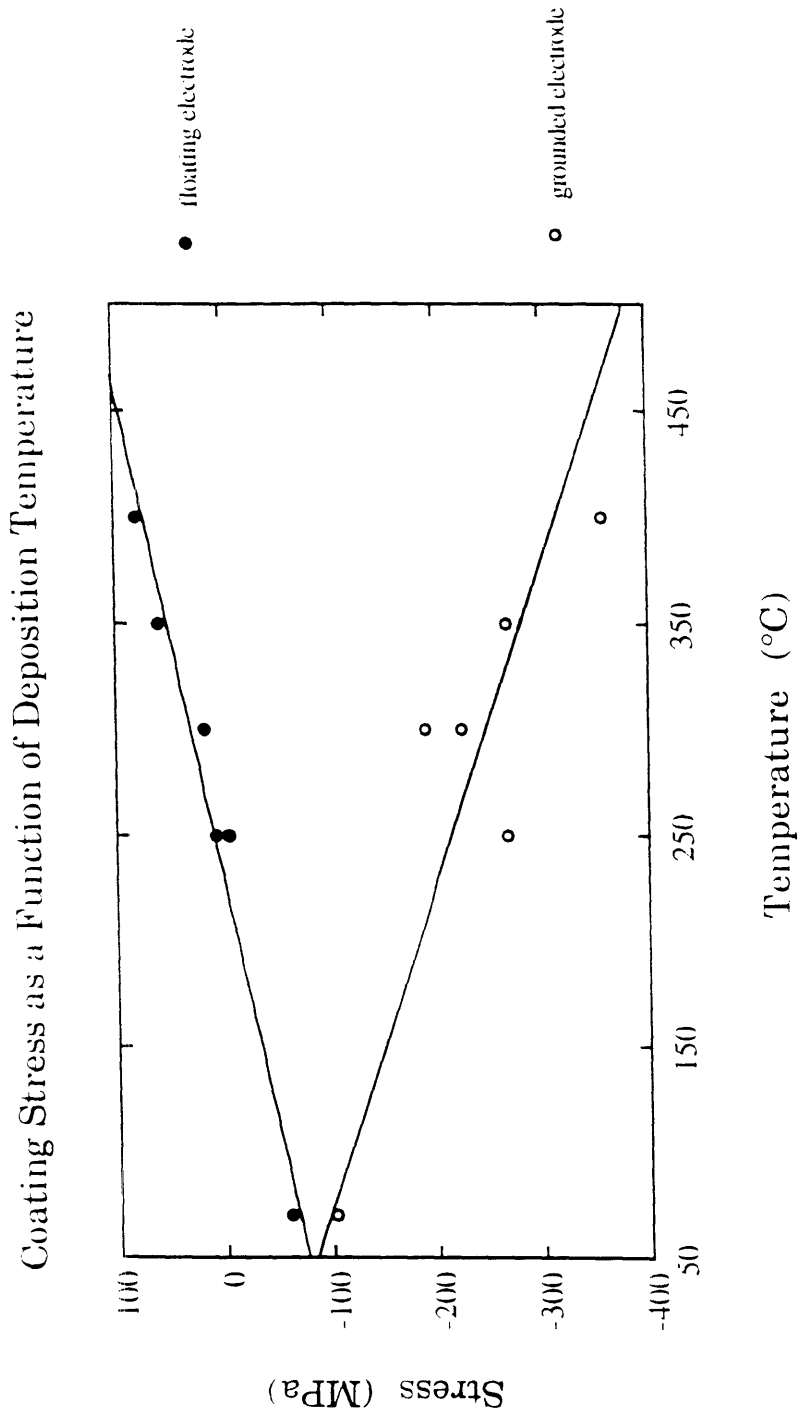
Figure 3.14   As-Deposited stress as a function of substrate temperature for grounded and floating lower electrodes.

67

Stress as a Function of Voltage at the Lower Electrode
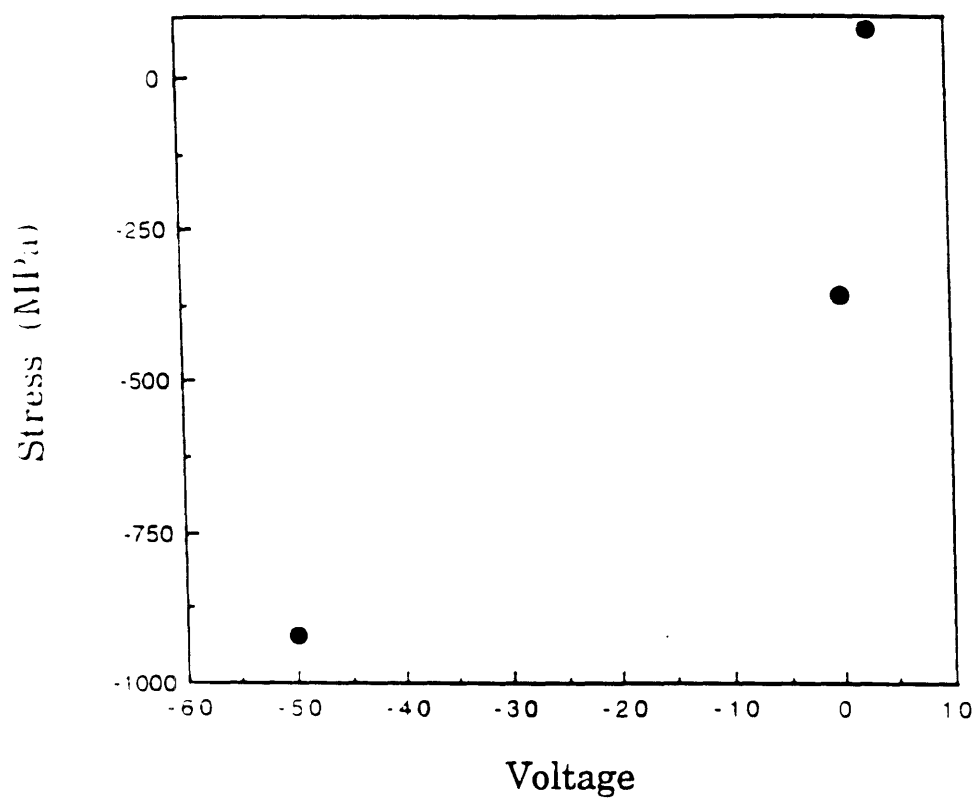
Figure 3.15 As-Deposited stress as a function of voltage at the lower
electrode for standard SiC deposited at 400°C.
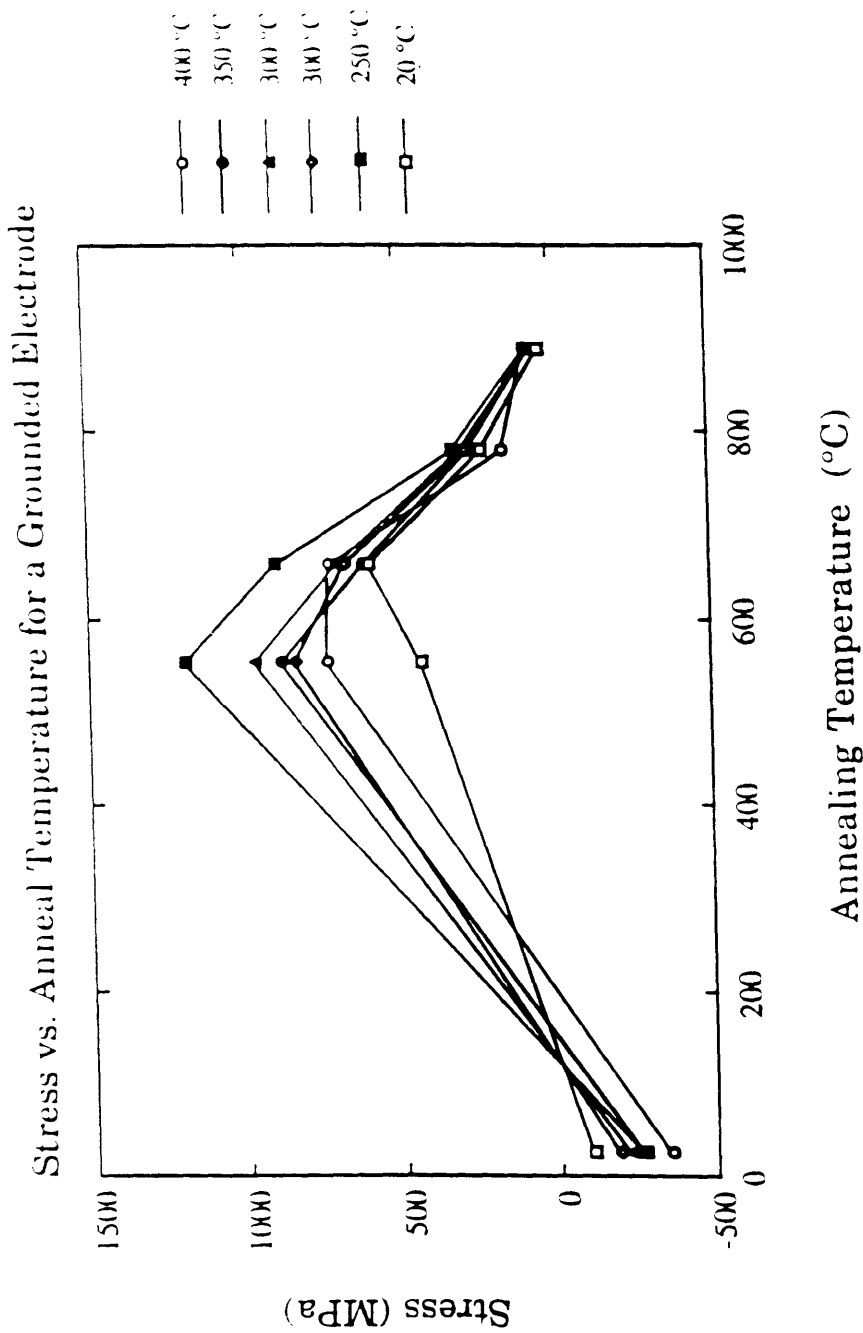
Figure 3.16 Stress in the coatings deposited on a grounded electrode at 20, 250, 300, 350, and 400°C as a function of annealing temperature for consecutive one hour anneals.
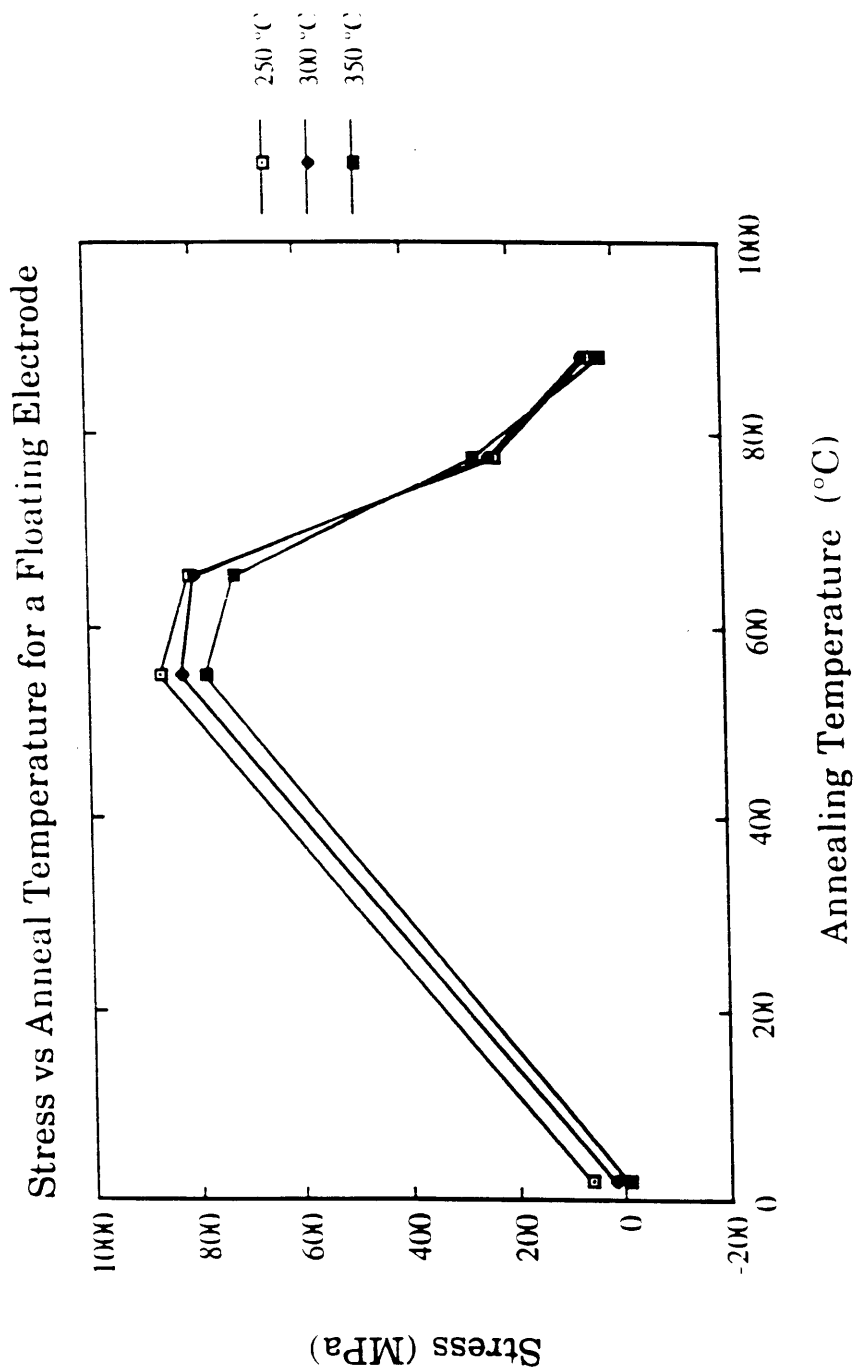
Figure 3.17 Stress in the coatings deposited on a floating electrode at 250, 300, and 350°C as a function of annealing temperature for consecutive one hour anneals.

Coating Stress as a Function of Anneal Times at 600°C
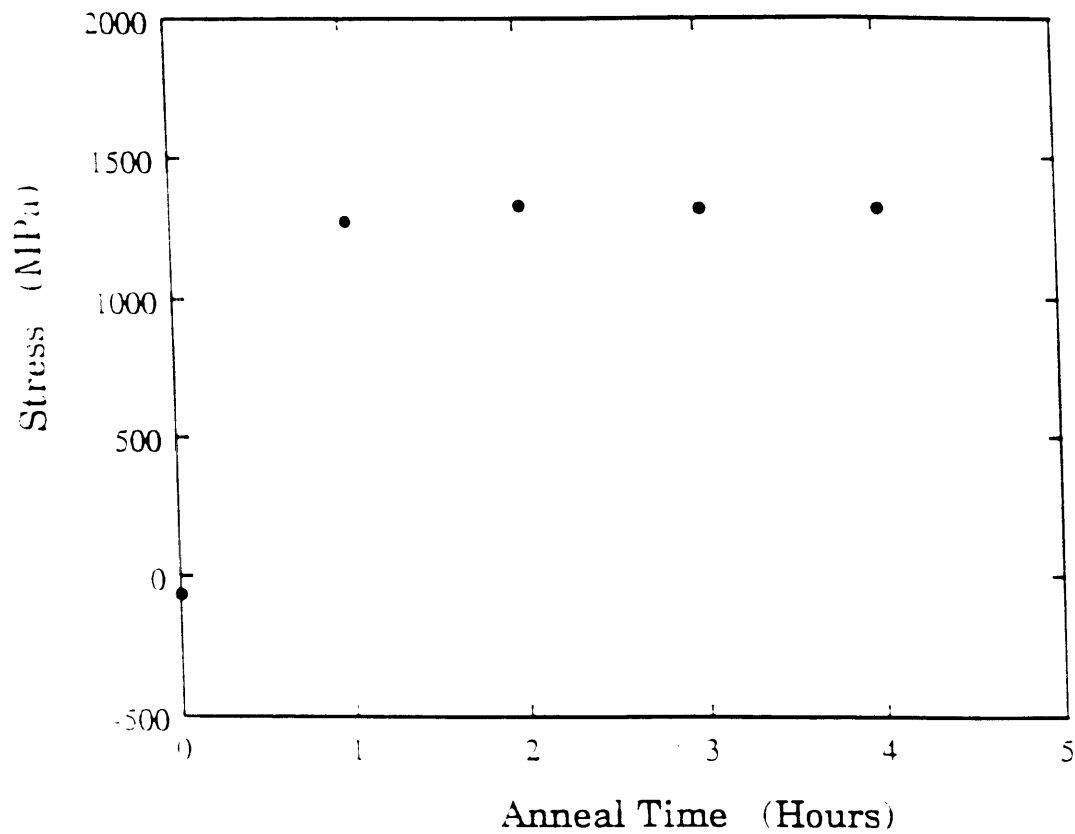
Figure 3.18 Stress as a function of anneal time at 600°C for a carbon rich coating deposited on a floating lower electrode at 400°C.

IV. Carbon Interlayers by Plasma Enhanced CVD and Low Pressure CVD

4.0 Introduction

The purpose of this chapter is to present and discuss the processing of carbon interlayers for the model test couples. This chapter will focus on processing-structure relationships. The mechanical property of the carbon coating of particular interest to this work is the tensile strength of its interface with the substrate. However, since the laser spallation experiment, used to determine tensile strength of interfaces, is not discussed until chapter 5, results regarding the effect of a carbon interlayer on the strength of the interface of the model couple will be discussed following the chapter on laser spallation.

The carbon films were deposited by both plasma enhanced CVD and low pressure CVD (LPCVD). The structure of the PECVD carbon ranged from amorphous to a microcrystalline, or turbostatic, layered structure and was examined by transmission electron microscopy. The LPCVD carbon was highly oriented and x-ray diffraction was used to differentiate its structure. (The perfectly ordered and turbostatic structures are shown schematically in Figure 4.4 a and b, respectively.) As the nature of the carbon deposited by these two methods is very different, each type of carbon will be discussed fully in turn. For each carbon type a background is first established by briefly outlining what the literature contains about the processing-structure-property relationships. For the first case this will be very short as PECVD has been described in the previous chapter. For carbon deposited by the low pressure CVD process, the literature review is

somewhat longer, focusing on the characterization of material orientation by x-ray diffraction. The background section for each carbon is followed by a detailed process procedure, results and discussion of results, and a summary.

4.1 Carbon by Plasma Enhanced CVD

4.1.1 Background

In this section we will focus on how power supplied to the plasma and substrate temperature affect film structure. The PECVD process in general and methane plasma chemistry in particular were reviewed in the previous chapter.

With an increase in plasma power the film structure changes from polymeric to amorphous, or glassy, diamond-like to graphitic [40, 76-80]. At very low power the deposit is a hydrogenated polymer with a hardness below that of graphite [79]. At higher powers there is another transition in structure from amorphous to graphitic. Berg found that films deposited at 50 watts from butane at 6 mtorr were hard and amorphous while coatings deposited at 600 watts were graphitic, described as easy to remove from the substrate having a resistivity of about 1 ohm-cm [77] while Holland cited a similar transition at 200 watts and 100 mtorr for methane [76]. Minagawa, et. al. [79] found this same amorphous to graphitic transition between 50 and 100 watts in pure methane; however, these experiments were conducted at 800°C. Shimizu, et. al. [80] cite a similar transition except that they correlate this phenomenon with relative plasma potential rather than with power achieving the same transition at 100 watts with a 100 volt DC bias applied to the substrate holder.

It is important to note that, with respect to the supplied powers quoted in the above paragraph, these numbers should be taken as qualitative indicators of processing trends. Even if one were to divide the quoted numbers by the electrode surface area, the electron energy and density distributions in the actual process conditions would still be just as elusive because the electron distributions also strongly depend on gas type and pressure, and electrode material and spacing,

This last bit of evidence from Shimizu and coworkers reveals the basis of this phenomenon. It is not power, but ion bombardment intensity that determines this amorphous carbon to graphite transition. This also explains the variation of reported threshold powers for the transition -- ion bombardment is very sensitive to reactor geometry. At very low plasma powers radicals are not extensively broken down in either the plasma or at the surface. These molecules are incorporated into the coating whole resulting in voids. At higher power, due to collisions in the plasma and ion bombardment at the surface, radicals are broken down and hydrogen is driven off. At these middling power levels hydrogen is driven off; however, the level of ion bombardment is not sufficient to give adatoms the surface mobility required for longer range ordering, and an amorphous structure results. High ion bombardment of the surface enhances both hydrogen desorption and surface mobility. This provides the energy required for forming an ordered structure.

The amorphous to graphite transition has also been observed with an increase in the substrate temperature [76, 79, 81]. Meyerson reports the transition between 250 and 400°C [81], Minagawa et. al. were able to form graphite by heating the substrate from 20 to 200°C [79], and Holland reported a 120°C transition temperature [76]. As with the effect of ion

74

bombardment, increased surface temperatures would enhance hydrogen desorption and adatom mobility.

It should be noted that the definition of graphite for these studies often simply meant "not diamond-like carbon" and that the graphite structures they discuss still contain large amounts of hydrogen and do not quite have the extensive order of carbon deposited by thermally activated processes. A highly oriented carbon has been reported deposited by PECVD from propylene (C_3H_8) at 350°C and this was confirmed by x-ray diffraction [82]. Regardless of how graphite is defined, generally, material deposited at low power and low temperature is a porous polymer containing large amounts of hydrogen while materials deposited at somewhat higher powers are hard, amorphous, transparent to visible light, and of a high electrical resistivity . At even higher temperatures and power films are graphitic and can be described as soft, optically dark, with a low resistivity and with a low adhesion to the substrate.

4.1.2 PECVD Carbon Processing Procedure

The selection of processing parameters for the interlayers of the couples was based on the results of previous workers as described above. Two sets of processing parameters were chosen such that amorphous and graphitic carbon might be produced. The exact processing parameters are listed in Table 4.1. Note that the material produced by each is denoted as "grounded" and "powered" carbon and that the only difference between them is in the power supplied to the plasma. For the first type the lower electrode is grounded during deposition while for the second type the lower electrode is powered creating an approximately -100 V bias. The objective in choosing the above parameters was to create sufficient bombardment

during deposition for the powered carbon so that it would be graphitized, while the grounded carbon would be amorphous and diamond-like.

Table 4.1

PECVD Carbon Processing Parameters

Processing Parameters	Carbon Type	
	"Grounded" Carbon	"Powered" Carbon
Substrate Temperature	400°C	400°C
Pressure	50 μm	50 μm
Methane Flow Rate	5.0 sccm	5.0 sccm
Upper Electrode	30 watts	100 watts
Lower Electrode	grounded	30 watts

The specimens were cleaned and placed in the PECVD reactor as described in the previous chapter. Couples for spallation measurements were sequentially coated with 0.2 μm of carbon and then with 2.0 μm of SiC. Specimens were also made by depositing approximately 25 nm of each carbon onto polished sodium chloride disks and (100) p-type silicon wafers.

Films deposited on salt crystals were subsequently floated off and examined by TEM at 200 KV. Carbon coatings deposited on silicon were examined by Perkin Elmer 548 x-ray photoelectron spectroscopy (XPS). A gold dot was deposited on the edge of these XPS specimens by thermal evaporation through a shadow mask. During XPS analysis the specimen was flooded with electrons to a relative potential of -10eV. The gold peak was located before and after the carbon peak was studied. All peak values were then corrected to correspond to the known gold peak at -84 eV.

4.1.3 PECVD Carbon Structure Results and Discussion

The PECVD carbon structure results can be summarized in three figures. Figures 4.1 and 4.2 contain photomicrographs of the TEM real space and diffraction patterns for the grounded and powered carbon, respectively. Figure 4.3a shows the XPS carbon 1s peak intensity as a function of electron energy for both the powered and grounded carbons. XPS standard results were also obtained for pyrolytic carbon and for carbon deposited from a thermal evaporator; these are shown in Figure 4.3b.

Neither the "powered" carbon nor the "grounded" carbon are seen by TEM to be crystalline. The "grounded" carbon is microcrystalline at best; some lattice fringes can be seen in the high resolution micrograph in Figure 4.1. The real space micrograph of the "powered" carbon shows it to be fully amorphous. The diffraction patterns of both show the distinctive ring of amorphous material; however, the ring of the powered carbon is much broader and more diffuse. The grounded carbon diffraction ring is relatively sharp.

X-ray photoelectron spectroscopy analysis yields information about the nature of the chemical bonds near the surface of a specimen. The specimen surface is illuminated with x-rays which causes the emission of electrons. Electrons emitted near the surface may have the energy necessary to escape the material. XPS analysis determines the energy required to separate these electrons from their bonds. The XPS results show that the binding energies for both PECVD carbons are shifted about -0.4 eV from the graphite standards which both fall at -284.5 eV as shown in Figure 4.3b. A smaller peak at -283.2 eV is also seen in the grounded carbon. Interestingly, this binding energy corresponds to the SiC bond [83].

At 400°C the substrate must react with the activated carbon radicals. This second peak does not correspond to the carbon-hydrogen bond, as the carbon-hydrogen bond is not discernible through XPS [84].

Regardless of the interesting XPS data, these results show that the use of this analytical technique for examining interlayers for spallation couples is of questionable value. TEM diffraction patterns of evaporated carbon deposited on salt show the structure to be completely amorphous, indistinguishable from the "powered" carbon diffraction pattern. The pyrolytic carbon standard was shown by large area x-ray diffraction to be highly oriented, yet both of them gave identical XPS carbon 1s peak positions; only the peak full-width half-max varied slightly. XPS could not differentiate these two dramatically different structures because the chemical bonds were the same regardless of their orientation. After these results, XPS was dropped as an analytical tool for the study of the couple interlayers.

These results show that the processing parameters chosen did not yield graphitized carbon. The "powered" carbon experienced sufficient ion bombardment to randomize the structure, but not sufficient to graphitize it. The "grounded" carbon was not randomized by bombardment so that the order of the initial bonding was maintained. This "grounded" carbon was microcrystalline in structure.

4.1.4 Summary of Processing of Carbon by PECVD

Amorphous and microcrystalline films were produced by PECVD to be used as interlayers for interface test couples. While large changes in processing parameters for PECVD carbon coatings produces large changes in optical and electrical properties [81], preliminary results indicated that

they would not yield the variability of structure desired for the interface couples. At this point attention was turned to the possibilities of producing carbon of widely varying structures by thermally activated chemical vapor deposition. Furthermore, XPS was found to be unsatisfactory for purposes of differentiating carbon structures.

4.2 Carbon by CVD

Carbon deposited by thermal decomposition of a hydrocarbon gas is often called pyrolytic carbon and is usually more ordered than carbon deposited by glow discharge processes. The properties of a single, highly oriented carbon crystal are highly anisotropic and therefore the bulk properties are determined by the average of the size and orientation of all crystals with their c-axis aligned parallel in the material. For this work it was hypothesized that the tensile strength of the carbon interlayers perpendicular to the substrate could be manipulated by varying the degree of order in that direction. The rest of this chapter concerns the processing of carbon by thermal decomposition of propane to obtain pyrolytic carbon layers of various degrees of orientation as determined by x-ray diffraction to produce interface couples of varying strengths.

4.2.1 Background/Literature Review Regarding Pyrolytic Carbon

Pyrolytic carbons are composed of crystallites of relatively ordered structure containing various fractions of amorphous material, misaligned layers, and cross-linking between layers [9, 85]. These layers may be thought of as giant aromatic molecules [86]. Carbon structures in which adjacent layers are not regularly oriented with respect to each other are often called "turbostatic." A more precise term would be "microcrystalline"

as the structure is crystalline, but only over very short distances; the material contains large amounts of defects. Both the perfectly ordered and turbostatic structures are shown schematically in Figure 4.4a and b. In the ideal graphite structure layers are stacked over one another in a hexagonal sequence "ababab". The microcrystalline layers are parallel, but without the ordered network structure.

The bulk material is called isotropic or anisotropic depending on the degree to which the crystallites have a preferred orientation. If the crystallites are completely random in their orientation, the material is called "isotropic." The anisotropic and isotropic deposits are shown schematically in Figures 4.5a and 4.5b, respectively. Generally, it may be said of these deposits that the anisotropic material, often called "laminar," is deposited at low temperature, usually between 1000 and 1350°C, with small crystallite sizes, and high density while the isotropic material is deposited above 1350°C and has intermediate to large crystallite sizes with a lower density [9, 87]. The processing transition temperature will vary depending on the pressure, specimen surface area, and feed gas [9, 87].

The development of laminar and isotropic structures may be understood in terms of the nucleation and growth processes involved . The laminar carbon structures are produced when film nucleation at the surface is slow compared to the growth due to radical attachment at the surface. As the intensity of reaction increases, as may happen due to increased temperature, concentration of reactants or active surface area, the formation of nuclei at the surface dominates causing film growth to proceed away from each nuclei in many directions, not just the macroscopic growth direction, and the isotropic structures are formed.

The active species which are the source material for nucleation and growth are produced when the source gas thermally decomposes at a hot surfaces [88]. The products of this dissociation react in the gas phase and also continue to break up upon contact with surfaces [89]. During these reactions carbon is both deposited at surfaces and complex carbon rings are formed in the gas phase. These aromatic molecules orient themselves with respect to surfaces and are the primary source of material for the growing crystallites [89]. The hexagonal rings tend to lay flat with respect to the surface, but if there is not sufficient thermal energy present for surface mobility, they may not line up with each other as they deposit, leading to the turbostatic structure that is not precisely crystalline [90, 91].

The deposition process is determined by the nature of the feed gas, temperature, residence time, and active surface area [87, 92]. Conditions which favor isotropic carbon formation are long contact times, high hydrocarbon partial pressures and small surface areas [87]. It should be noted that all of the studies referenced in this section, even those which reported producing highly oriented material, have all been conducted either at relatively high pressures (greater than 1 Torr) or in fluidized beds.

The majority of studies of specific hydrocarbon reactions have been conducted with methane [9, 87, 88, 91-97]; however, the decomposition and reaction of propane [98], benzene [99, 100], acetylene [101], and propylene [102, 103] have also been investigated. These studies have shown that a wide variety of species may form in the gas phase. Diefendorf showed that for methane decomposition at a surface between 1000 and 2500°C the reaction products are H_2, H, C_2H, C_3H, and CH_4 [70, 91]. He also showed that deposition does not occur from the parent molecule but from an active intermediate. Lieberman found that for methane based reactions over a

similar temperature range the dominant species formed are C_2H_2, C_2H_4, C_2H_6, C_3H_8, and C_3H_6 [95], i.e., acetylene, ethylene, ethane, propane and proplyene, respectively. Powell found C_2H_6, C_2H_4 and C_2H_2 to be the intermediates of methane decomposition and determined that the break up of methane is slower than the other steps in the process [89, 97]. Peirson's studies of deposition from methane on carbon fibers between 1200 and 1450°C showed that the transition between oriented and isotropic material correlated with the ratio of acetylene, C_2H_2, and benzene, C_6H_6, produced in the CVD chamber [92]. As the relative amount of acetylene increased, the transition from anisotropic to isotropic deposition occurred at lower temperatures.

Studies of the reactions in systems with other hydrocarbon source gases have also shown that the parent hydrocarbons break up into radicals at surfaces and recombine to form intermediates which then decompose at surfaces leaving carbon and evolving hydrogen [9]. For example, Hoffman showed that propylene decomposes to form ethylene and methane [102, 103]. The methane would then decompose as described above. Note also that ethylene is a product of methane decomposition and the problem again reduces to one of balancing the relative amounts of acetylenic and aromatic species [96]. The idea that these hydrocarbons dissociate and deposit carbon through similar reaction paths is reinforced as workers have been able to produce identical carbon structures with different feed gases by varying the temperature and pressure of the system [9].

The structure of the deposit is determined by the relative rates and dominant reactions of the processes as described above and the properties of the bulk material are a sensitive function of the size and degree of preferred orientation of the crystallites [9]. This is because the crystals themselves

have very direction sensitive properties. The carbon-carbon bond energy within the layers is 477kJ/mole as compared with an energy of only about 17kJ/mole for the van der Waals interaction between the layers [9] This same disparity between properties in plane and between the planes is seen in the thermal conductivity, thermal expansion coefficient, and modulus of elasticity. These values are listed in Table 4.2 and the modulus is shown as a function of crystallographic orientation in Figure 4.5.

Table 4.2 The In-Plane and Between Plane Properties of Pyrolytic Carbon

	In Plane	Between Planes
Bond Strength[9] (kJ/mol)	477	17
Thermal Conductivity[90] (J/m/s/°K)	2000	2.0
Thermal Expansion[90] (°K^{-1})	6.7×10^{-6}	5.5×10^{-7}
Modulus[90] (GPa)	910	38

Average crystallite size and the degree of orientation have been the primary parameters used to describe carbon deposits and are usually determined through the use of x-ray diffraction. The crystallite size L_a is determined by measuring the broadening of the diffraction peak as given by Warren [104]:

$$L_a = \frac{0.9\,\lambda}{B_{hkl}\cos\theta} \qquad (4.1)$$

where λ is the wavelength of the x-rays used and B_{hkl} is the extra broadening of the x-ray peak, measured as the full peak width at half of the maximum peak intensity. The broadening is not simply the difference between the peak width and that of a standard, but is a difference of their squares:

$$B_{hkl}^2 = B_M^2 - B_S^2 \qquad (4.2)$$

where B_M is the measured breadth and B_S is the breadth of a standard.

The degree of preferred orientation is quantified through a technique developed by Bacon [105] which gives a value of 1.0 for perfectly isotropic material with the "Bacon Anisotropy Factor" (BAF) increasing with the degree of preferred orientation. The BAF is explained with the aid of Figure 4.6.

Figure 4.6a is a schematic of a single crystallite showing the layers in the material perpendicular to the c-axis and defines an angle, ϕ, as the angle between the c-axis and the normal to the deposition plane. The material property, a, of an individual crystal in the ϕ direction would then be:

$$a_\phi = a_c \sin^2\phi + a_a \cos^2\phi \tag{4.3}$$

where a_c and a_a are the material properties in the a and c directions in a perfect carbon crystal. If the z direction is defined as perpendicular to the substrate, then the average of material property, $\overline{\alpha}_z$, in the z direction due to the sum of the crystallites would be given by [9]:

$$\overline{\alpha}_z = \frac{\displaystyle\int_0^{\pi/2} \alpha(\phi)\, I(\phi)\, \sin\phi\, d\phi}{\displaystyle\int_0^{\pi/2} I(\phi)\, \sin\phi\, d\phi} \tag{4.4}$$

where $I(\phi)$ is shown in Figure 4.6b as the relative diffracted x-ray intensity from the specimen tilted from 0 to 90 degrees signifying the density of layer-plane normals per unit of solid angle [9]. (It should be noted that it is necessary to measure integrated intensity, not simply peak intensity.)

Combining equations 4.2 and 4.3 it may be shown that the average material property, $\overline{\alpha_z}$, in the z direction may then be given by:

$$\overline{\alpha_z} = \alpha_a R_z + \alpha_c (1 - R_z) \tag{4.5}$$

where R_z is defined as:

$$R_z = \frac{\displaystyle\int_0^{\pi/2} I(\phi) \sin^3\phi \, d\phi}{\displaystyle\int_0^{\pi/2} I(\phi) \sin\phi \, d\phi} \tag{4.6}$$

Similarly, a weighted average for material properties in the plane of deposition may be defined as:

$$\overline{\alpha_{xy}} = \alpha_a R_{xy} + \alpha_c (1 - R_{xy}) \tag{4.7}$$

where R_{xy} is:

$$R_{xy} = \frac{2 - R_z}{2} \tag{4.8}$$

The Bacon Anisotropy Factor is then defined as:

$$BAF = \frac{2}{R_z} - 2 \tag{4.9}$$

Note that R_z ranges from zero to 2/3. Therefore, when the material is perfectly random in orientation, R_z is 2/3 and the BAF is 1.0. As the degree of orientation increases, R_z approaches zero and the BAF becomes infinite for the perfectly oriented material.

The effect of processing parameters on the preferred orientation of the deposit has been extensively investigated. A typical relationship between BAF and processing parameters for a fluidized bed at one atmosphere pressure is shown in Figure 4.7 from Bokros [87]. Here BAF is

plotted versus bed temperature and methane concentration. At lower bed temperatures near 1000°C the deposits are highly oriented with BAF's around 5.5. As the processing temperature is increased, the deposits become isotropic by 1500°C for most methane concentrations. At a given temperature preferred orientation was found to increase with methane concentration and decrease with an increase in bed surface area. Pierson [92] studied the deposition of pure methane on carbon fibers from 1200 to 1450°C between 20 and 630 Torr and reported a similar trend in anisotropy; however, he found the transition from laminar to isotropic carbon to be complete by 1350°C. He was also able to induce this transition at 1275°C at 630 Torr by changing the carbon to hydrogen ratio from 1:4 to 1:14 in the feed gas. Akins and Bokros [98] found that the transition temperature could be extended down to 1100°C using propane as a source gas at atmospheric pressure and Kobayashi, et. al. reported producing anisotropies between 1.0 and 1.8 at 1000°C using acetylene [101].

The average crystallite size in the deposit is usually reported with the Bacon Anisotropy Factor and has been found to have an inverse relationship with orientation [105] and deposition temperature [98]. Tesner [88] showed that the log of crystallite size is linear with respect to the inverse of temperature indicating that the crystallite growth is the result of a process controlled by thermal activation. However, Bokros [87] reports an increase of crystallite size with deposition temperature from 3.5 nm at 1300°C to 10 nm at 1900°C at 5 percent methane in argon and a decrease from 3.5 to 2.5 nm at 40 percent methane in argon. He also reports a general decrease in crystallite size with an increase in methane concentration between 1300 and 1900°C. Kaae [93] showed by cross-sectional

TEM that the crystallite size for an isotropic material deposited from methane at 1300°C is 3.0 nm.

In summary, crystallite size is determined by the balance of the nucleation and growth rates. If a change in processing conditions causes the nucleation rate to increase with respect to the general growth rate, crystallite size will decrease.

The density of carbon deposits has also been determined as a function of processing variables. The usual method of determining density is by a sink-float method whereby a piece of coating is dropped into a cylinder of liquid that has a density gradient due to a temperature gradient induced in the column. The position at which the material ceases to sink is used to calculate density. Another, less precise, technique is to titrate one low density fluid into a high density fluid until a piece of deposit at the surface just begins to hang suspended below the surface. The density of the fluid is then measured. The density of the deposit is generally increases with an increase in preferred orientation [9]. Kaae [93] and Ubbelohde [86] attribute this type of relationship to the large volume fraction of clefts and micropores incorporated with the isotropic crystallites during film growth. Akins and Bokros [98] report little dependence of density on gas composition at a constant deposition temperature. Kobayashi, et. al. [101], however, found that coating density decreased with an increase in acetylene concentration, but they also attributed low densities to poor crystalline alignment and incorporation of soot-like crystallites during rapid growth. The ideal theoretical density of perfectly oriented carbon is 2.26 gm/cm^3 [86].

In summary, carbon deposited by CVD may be processed to have a wide spectrum of structures and properties. It should also be possible to produce carbon layers with tensile strengths over a wide range depending

on such structural characteristics as degree of preferred orientation and cross-linking between layers, crystallite size, and density.

4.2.2 Low Pressure CVD (LPCVD) Carbon Processing Procedure

The LPCVD apparatus was designed and constructed to attach to the PECVD reactor in such a way as to share gas flow controllers and pumping system. This is shown schematically in Figure 4.8. The CVD chamber itself consisted of an alumina tube with a 3.2 cm internal diameter running through a Lindbergh 3-zone SiC glowbar furnace. The hot zone was 46 cm long. Temperature was measured at the outside diameter of the alumina tube with a Type S thermocouple. Specimens were fixed to a polished graphite boat with molybdenum screws to insure good thermal contact and the boat always located in the center of the hot zone.

The substrate used for the x-ray diffraction tests was microcrystalline SiC produced by Morton International through a CVD process. Thick carbon coatings could be deposited on the SiC substrates as the difference in thermal expansion between SiC and carbon is very small. Coatings thicker than a few hundred nanometers spalled from the sapphire substrates used to produce the spallation test couples. The SiC was received in a ground condition and polished with 600 grit SiC paper.

Figures 4.9 and 4.10 contain x-ray diffraction results pertaining to the SiC substrate. Figure 4.9 is an intensity versus two-theta scan of the substrate and Figure 4.10 contains a pole figure of the substrate at a two-theta angle of 26.0 degrees. From these figures it may be seen that the substrate is microcrystalline with little preferred orientation. The pole figure shows that diffraction from the SiC substrate does not interfere with measurements of the carbon peak at 26.0 degrees until the specimen is

tilted to an angle of ϕ = 30 degrees. (All carbon two-theta scans were measured between ϕ = 90 and 35 degrees.)

Deposition procedure was as follows: Substrates were cleaned with tri-ethane, acetone and then methanol, blown dry with nitrogen, and fixed to the boat. The boat was placed in the alumina tube so as to be at the center of the hot zone, the reactor was pumped down with both the cryo and the turbo pumping systems, and the furnace was turned on. After the furnace had reached the set temperature and the pressure was less than 5×10^{-6} Torr, the cryo pump and the CVD chamber were isolated from the main system and each other. Gas flow was initiated and the turbo pumping system was used to pull the gases through the reactor. Gas flow for all depositions was 5.0 sccm propane and 50.0 sccm Argon for a pressure of 200μm in the reactor tube. After the gas flow had stabilized, the valve at the bottom of the PECVD reactor was closed and the valves at both ends of the CVD reactor were opened. The deposition was timed and at the end of the run the gas was shut off and the cryopump was immediately opened to quickly remove the process gases present. In this way deposition could be suddenly ended and 0.2 μm thick films deposited consistently. The specimen was cooled under vacuum inside the furnace to at least 500°C. After removal from the CVD system, the sapphire substrates were exposed to air, and then SiC was deposited as described in the previous chapter.

Substrates of SiC were found to be best suited for use while examining carbon coatings by x-ray diffraction. Because of the great mismatch in thermal expansion between sapphire and carbon, coatings of carbon on sapphire thicker than 1.0 μm spalled from the substrate upon cooling. It was desirable to have a carbon coating of several microns thickness to increase the diffracted x-ray signal. Tantalum, molybdenum,

tungsten, platinum, boron nitride and silicon carbide were all tested for compatibility with carbon processing by CVD. The first three metals formed carbides and the platinum interdiffused with the carbon. The carbon neither reacted with the BN or delaminated from it; however, BN does have a large x-ray peak at a two-theta value of 27.3 degrees. The carbon (002) peak is at 26.0 degrees. It was not possible to differentiate the two peaks. None of the above difficulties were experienced while using SiC substrates.

The carbon coatings deposited on SiC were studied by x-ray diffraction using copper radiation on a Rigaku™ RU 200 difractometer with the voltage set at 60 KV and the current at 180 mA. The diverging, receiving, and scatter slits were 1.0, 1.0 and 0.6 degrees, respectively. Scans were conducted over the two-theta range from 20 to 30 degrees at a 1.0 degree per minute scan rate to examine the (100) carbon peak at 26.0 degrees. Specimens were mounted in a pole-figure goniometer which was concentric with the diffractometer. During the first scan the specimen was oriented in the usual mode for x-ray diffraction. After this scan, the specimen was tilted forward 5.0 degrees and the same two-theta range was scanned again. The specimen was tilted forward 5.0 more degrees and this procedure was repeated until the total tilt measured 55.0 degrees. At this point a peak from the substrate began to interfere with the carbon peak. A Rigaku™ software package was used to determine the peak area for each tilt angle. These area intensities were then normalized with respect to the largest peak and plotted versus tilt angle as shown in Figure 4.11. Matlab™ software on Athena™ was used to fit this data to the hyperbolic secant function and Maple™ software, also on Athena™, was then used to

numerically solve the integrals in equation 4.6 for R_Z. The Bacon Anisotropy Factor was then calculated using equation 4.9.

The crystallite size was determined from the broadening of the carbon (001) peak with respect to the silicon (001) from a National Bureau of Standards single crystal specimen. Crystallite size was calculated using equations 4.1 and 4.2 above.

The density of the coatings was measured by a sink-float technique whereby the material to be tested floated on bromoform, BCH_3, and ethanol was titrated into the bromoform until the coating hung suspended in the solution. Bromoform and ethanol are completely miscible. A volume of the solution was then weighed and the density of the coating determined from the density of the liquid solution. As a check to this procedure beakers containing bromoform/ethanol solution with densities of 1.6, 1.7, 1.8, 1.9, and 2.0 gm/cm3 were mixed. Pieces of coating were floated in each one until it sank. The results of the two procedures matched.

4.2.3 LPCVD Carbon Results and Discussion

Results of the processing of carbon are displayed in Table 4.3 and plotted in Figure 4.12. Table 4.3 lists Bacon Anisotropy Factor, crystallite size, peak position and density for carbon deposited at 1100, 1200, 1300, and 1400°C. Bacon Anisotropy Factor is plotted versus deposition temperature in Figure 4.12a; crystallite size is plotted versus temperature in Figure 4.12b; and density is plotted versus temperature in Figure 4.12c.

Table 4.3 Structure and Property Results for Pyrolytic Carbon

Deposition Temperature (°C)	Anisotropy Factor	Crystallite Size (nm)	Lattice Parameter* (Å)	Density (gm/cm³)
1100	4.5	4.6	3.514	1.70
1200	5.5	4.8	3.514	1.68
1300	6.2	5.3	3.520	1.85
1400	6.6	7.9	3.514	1.90

*between layers.

From these results it may be seen that the degree of preferred orientation, average crystallite size, and density all increase with increasing deposition temperature while the lattice parameter remains constant. At 1100°C the deposit is already very oriented with an anisotropy factor of 4.5. At 1400°C this factor has increased to 6.6. Over this same temperature range the average crystallite size roughly doubles from 4.6 to 7.9 nm and the density increases by 12 percent from 1.7 to 1.9 gm/cm³. The increased deposition temperature produces a more oriented, denser deposit.

These trends are opposite to that which is reported in the literature as discussed previously in this chapter. In the temperature range from 1000 to 1500°C deposits are reported to decrease in degree of orientation, average crystallite size and density with an increase in deposition temperature. This is graphically shown in Figure 4.13 where the present results are plotted on the same axis with Bokros' [9] results.

The difference between the results of the present work and that of previous workers may be explained by a difference in rates of nucleation at the surface. At the lower temperatures deposition in past work has been

controlled by the kinetics of radical attachment at the film surface while at the higher temperatures radical attachment to existing nuclei is overwhelmed by the creation of new crystallites. The structure is determined through the fastest process at the surface, addition of radicals to existing nuclei or heterogeneous nucleation of new crystallites. As the nucleation rate increases with temperature the average crystallite size decreases and the decrease in density is associated with the increase in porosity; crystallites are nucleated so rapidly that the free radical reactions cannot fill the inter-crystallite voids with carbon. In the present work the reduced processing pressure suppresses nucleation events favoring radical attachment to existing crystallites. As the process temperature is increased radicals have even more surface mobility allowing formation of larger and more dense crystallites.

While it was not possible to determine the actual surface nucleation rates in the past and present works, some relevant processing parameters may be calculated. Table 4.4 contains a list of processing variables for the pertinent experiments and the processing characteristics for the same experiments are listed in Table 4.5. Gas diffusivity was calculated using equation (11-11) from Reid [106]:

$$D_{12} = 0.001858 \ T^{3/2} \left[\frac{M_1+M_2}{M_1 M_2}\right]^{1/2} \frac{1}{P\sigma_{12}^2 \Omega_D}$$

where T is the absolute temperature in Kelvin, M1 and M2 are the atomic masses of the gases, P is the pressure in atmospheres, σ_{12} is the Lennard-Jones force constant for the mixture, and Ω_D is the collision integral for the two gases. The force constant and collision integrals were determined from

tables provided by Reid. The mean free path for each system was determined using equation (1.4-3) in Bird [107]:

$$\lambda = \frac{1}{\sqrt{2}\pi d^2 n}$$

where d is the atomic diameter, here taken from the tables in the appendix in Reid, and r is the density. The collision frequency is calculated as the average gas velocity divided by the mean free path. The average molecular gas velocity was calculated as:

$$\bar{c} = \left(\frac{8kT}{\pi m}\right)^{1/2}$$

where m is the atomic mass and k is Boltzmann's constant. The residence time was calculated as pressure times volume over gas flow rate. These last two equations were taken from chapter 1 of Chapman [108]. Comparing processing characteristics it is clear that the rate of nucleation must be substantially less in this present work than earlier works.

Table 4.4 Processing Parameters of Present and Previous Workers

Author	Temperature	Gas 1	Gas 2	Pressure
	(°C)			(Torr)
Bokros[9], 1969	1300 - 1700	CH_4	He	760
Akins[98], 1974	1100 - 1300	C_3H_8	Ar	760
Kobayashi[101], 1974	1100	C_2H_2	Ar	760
Lahaye[100], 1974	1000 - 1100	C_6H_6	N_2	760
Pierson[92], 1975	1200 - 1300	CH_4	H_2	20 - 630
Kaae[93], 1985	1200 - 1500	C_3H_6	He	760
Hoffman[102], 1988	1100 - 1200	CH_4	H_2	150 - 400
Present Work	1000 - 1673	C_3H_8	Ar	0.2

Table 4.5 Processing Characteristics of Present and Previous Workers

Author	Diffusivity	Residence Time	Mean Free Path	Collision Frequency
	(cm^2/s)	(seconds)	$(cm \times 10^{-6})$	$(seconds^{-1})$ $(x\ 10^{10})$
Bokros[9], 1965,69	15 - 22	1.2	8.4	1.1
Akins[98], 1974	1.5 - 2.0	0.4	4.4	2.1
Kobayashi[101], 1974	2.2	1.4	5.8	1.5
Lahaye[100], 1974	0.33 - 0.37	0.5	4.0	2.1
Pierson[92], 1975	12 - 500	0.06 - 0.23	9.3 - 300	0.33 - 1.0
Kaae[93], 1985	10 - 12	0.61	6.2	1.6
Hoffman[102], 1988	16 - 47	$10^3 - 10^4$	15 - 39	0.23 - 0.59
Present Work	5600 - 7600	0.0044	20,000	.00046

It should be noted that even in the present system the deposition process is not completely surface reaction controlled. This is demonstrated in Figure 4.14 where the log of the growth rate is plotted versus the inverse of temperature. Two processing regimes may be seen in the figure. Below 1200°C the system is kinetically controlled by surface reactions. Above this temperature the growth rate is limited by gas diffusion through a boundary layer above the film surface. These two control regimes are defined independent of nucleation [109, 110]. The presence of kinetic control at the surface at low temperature gives support to the above explanation of the deposition process: it is at 1100°C where the system is completely kinetically controlled at the surface that the present orientation data, derived from material deposited at low pressure, matches the materials of previous workers, deposited at high pressure [9, 87]. At this relatively low

temperature the nucleation rate must be less than the surface reaction rate, even at atmospheric pressure.

4.2.4 Summary Regarding Deposition of Carbon by LPCVD

Pyrolytic carbon films were produced by low pressure CVD to be used as interlayers for interface test couples. Coatings were processed between 1100 and 1400°C at 200 mtorr pressure. It was determined that the degree of preferred orientation in the coating, average crystallite size, and coating density all increased with increasing deposition temperature. These trends were explained by the increased surface mobility during deposition with an increase in temperature and decrease in nucleation rates through the use of low processing pressure.
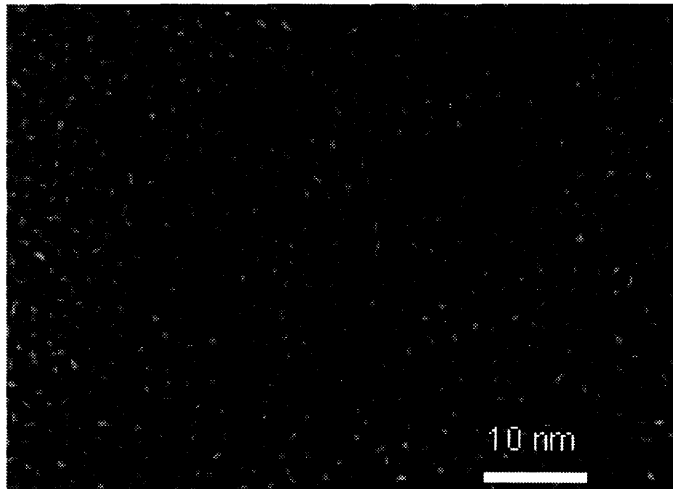
(a)
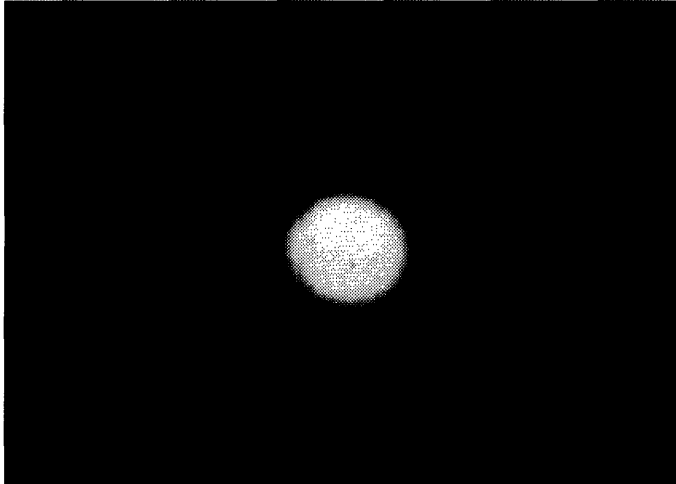
(a)

Figure 4.1   TEM real space photomicrograph and diffraction pattern for "powered" carbon deposit on salt. (See Section 4.1.2)
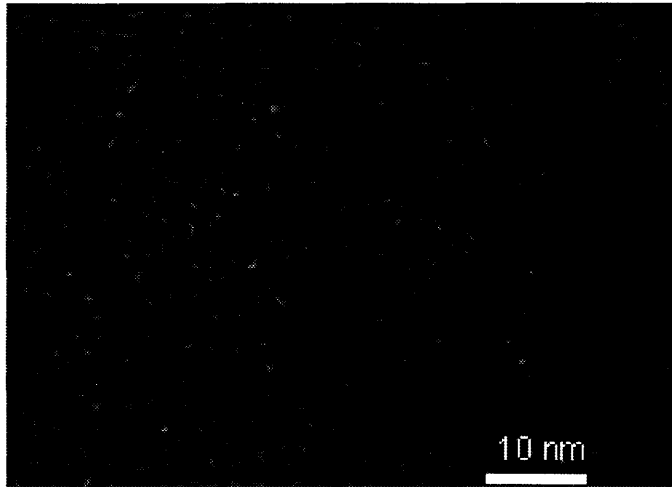
(a)
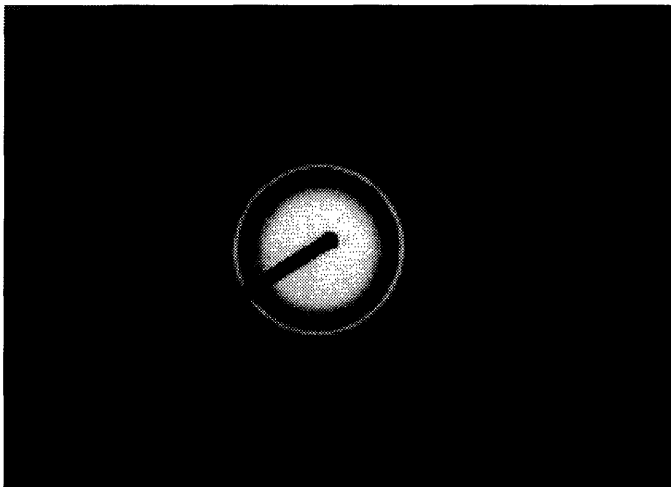
(b)

Figure 4.2   TEM real space photomicrograph and diffraction pattern for
            "grounded" carbon deposit on salt.

Carbon XPS 1s Peaks
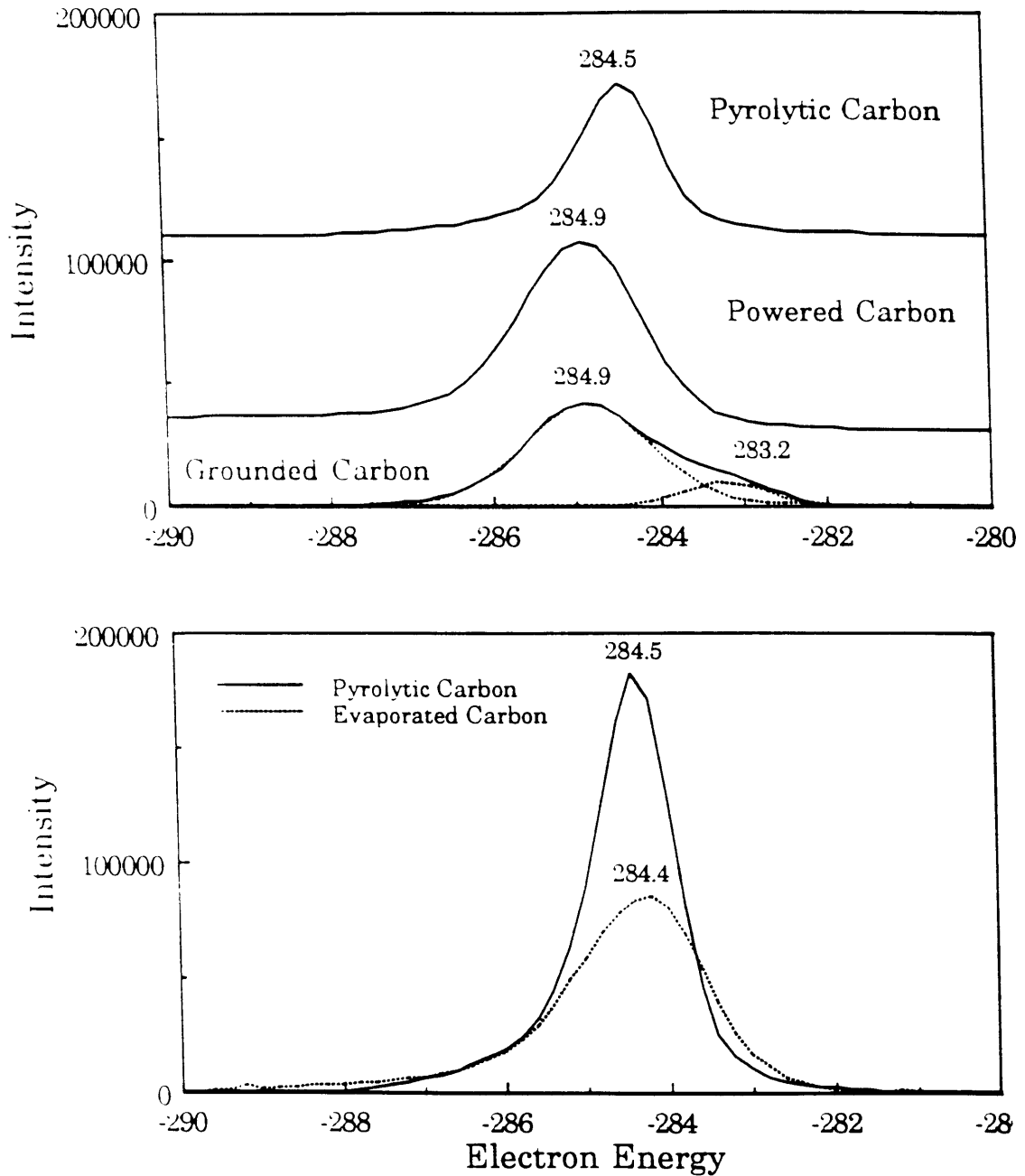
Figure 4.3 Carbon XPS 1s peaks for powered and grounded carbon as well as for highly oriented pyrolytic carbon and carbon deposited by thermal evaporation. The peaks in the upper figure are shifted for ease of comparison.
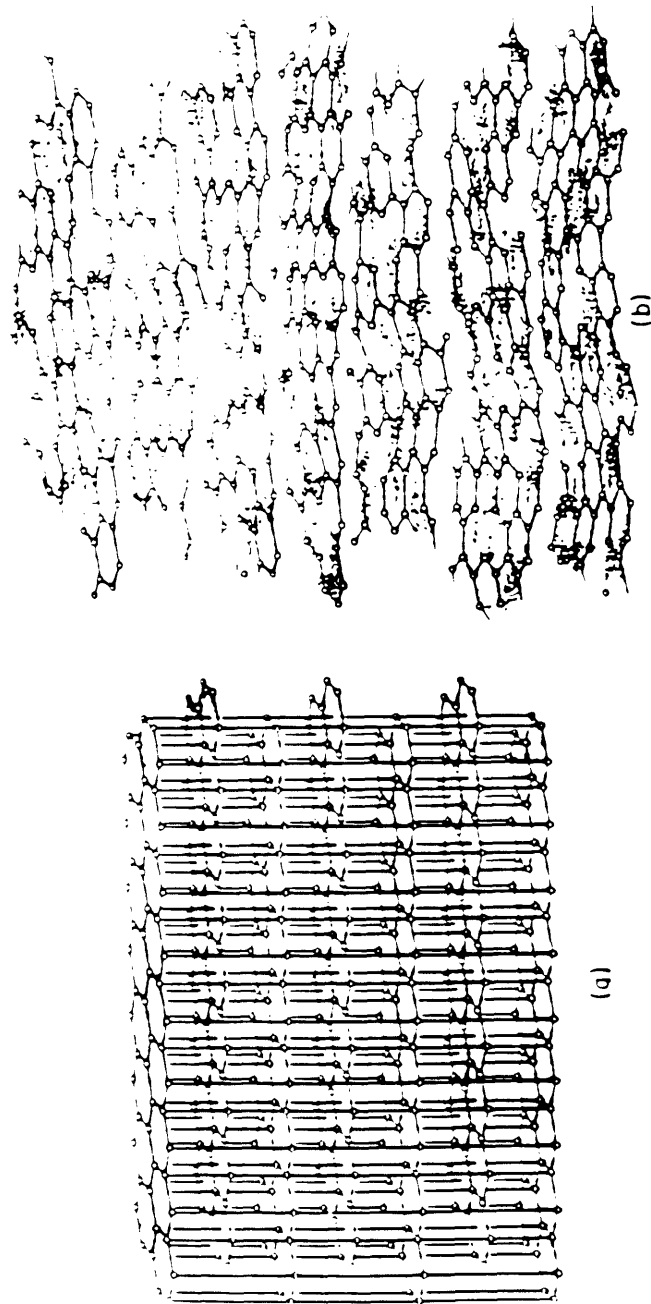
Figure 4.4   Schematic diagram of the structure of perfectly oriented (a) and turbostatic (b) graphite.
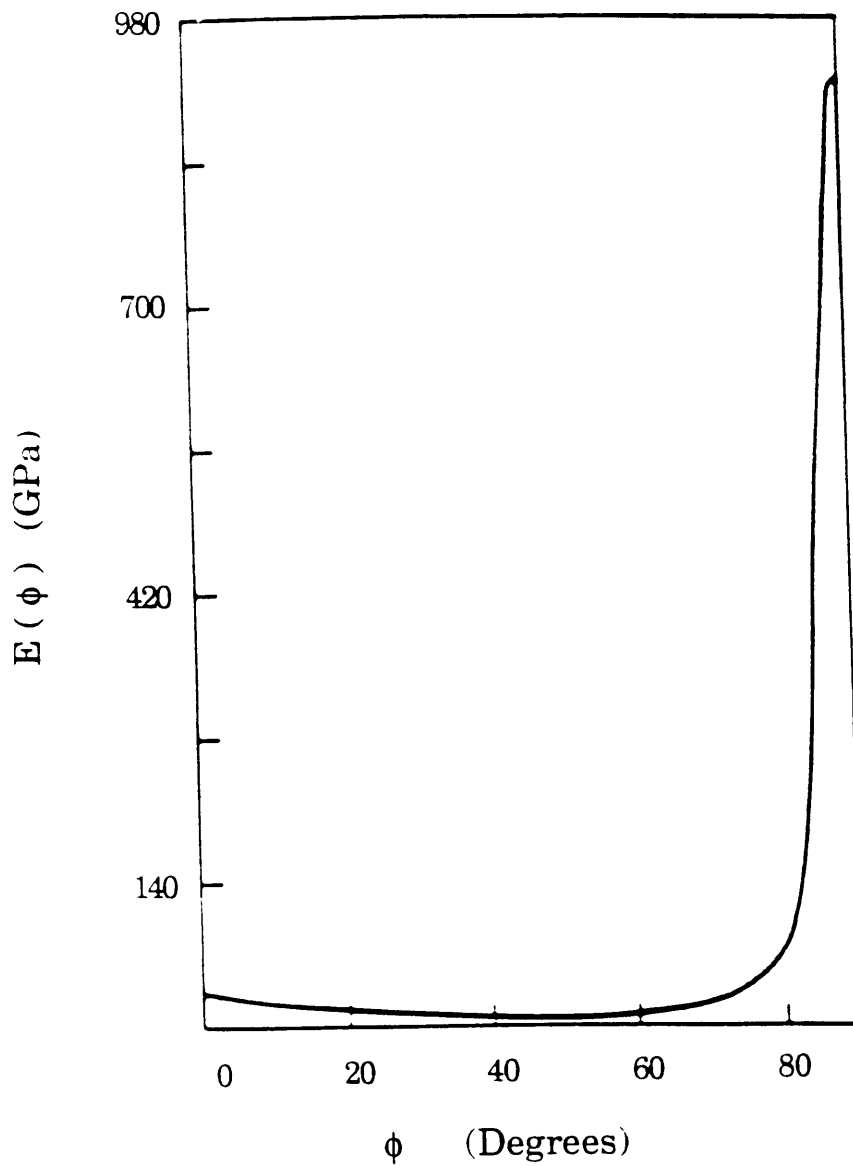
Figure 4.5   The elastic modulus of a graphite crystal as a function of
direction within the crystal. φ is the angle between the
normal of the deposition plane and the c axis of the
crystallite. See Figure 4.7.
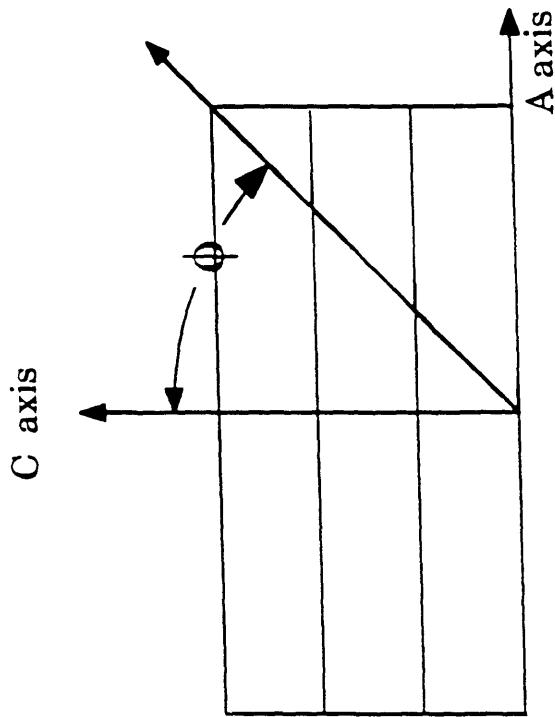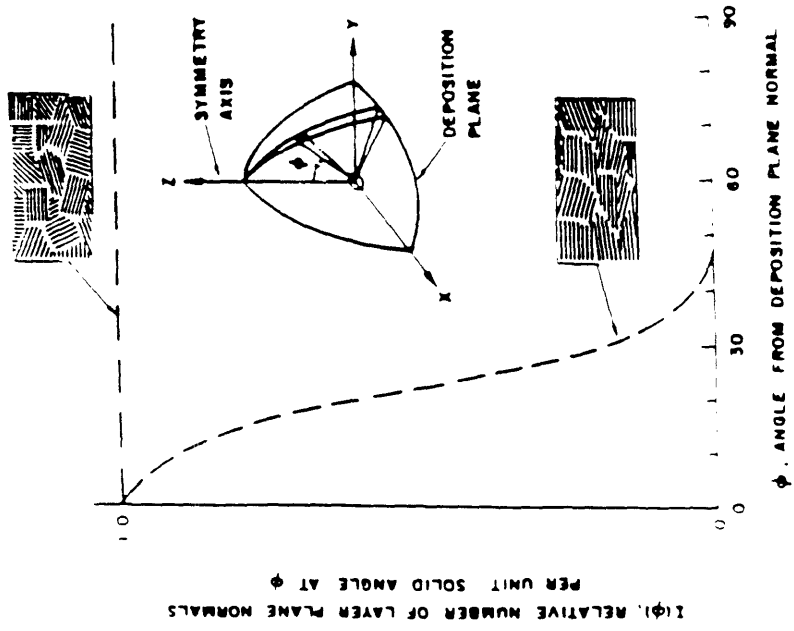
Figure 4.6   Schematic defining φ as the angle between the normal of the deposition plane and the c axis of the crystallite (a). Schematic showing the diffracted x-ray intensity versus angle from the deposition plane normal for isotropic and oriented carbon.

102
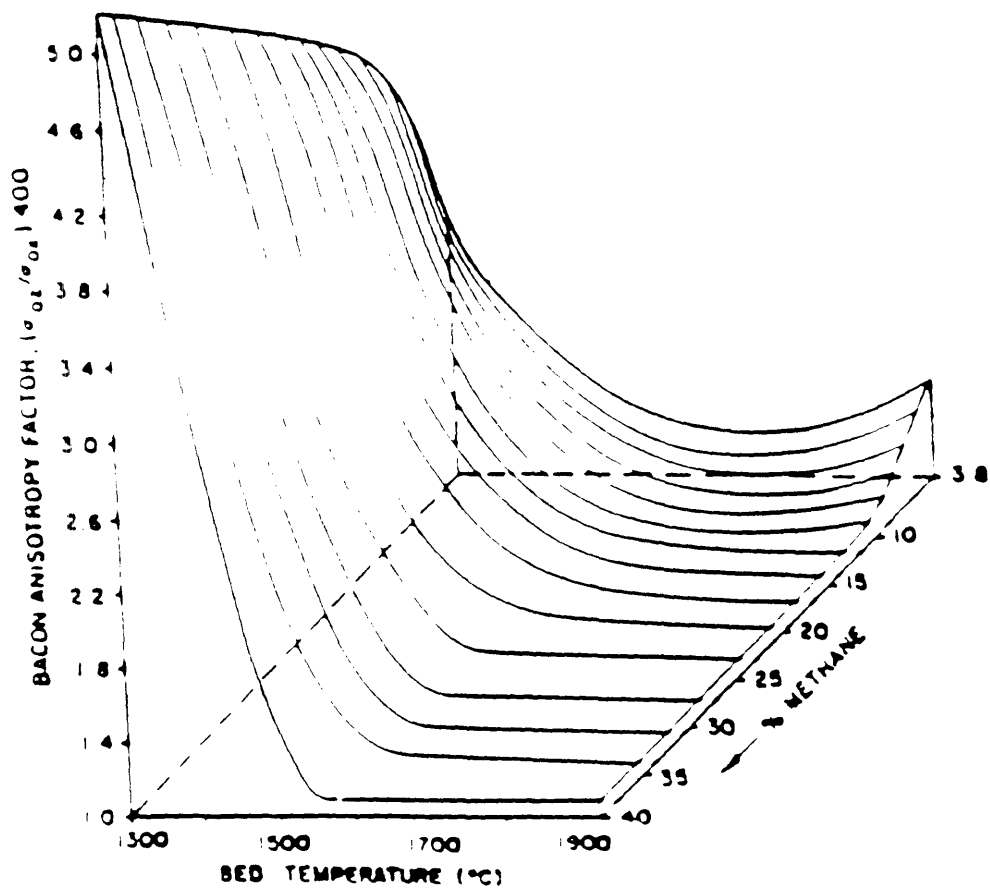
Figure 4.7 Bacon Anisotropy Factor of carbon deposited in fluidized beds from 1300 to 1900°C and 3.8 to 40 percent methane at atmospheric pressure, from Bokros [9].

Plasma CVD Reactor

Thermal CVD Reactor

Load Lock

gas inlet

Substrates

Furnace

to turbo pump
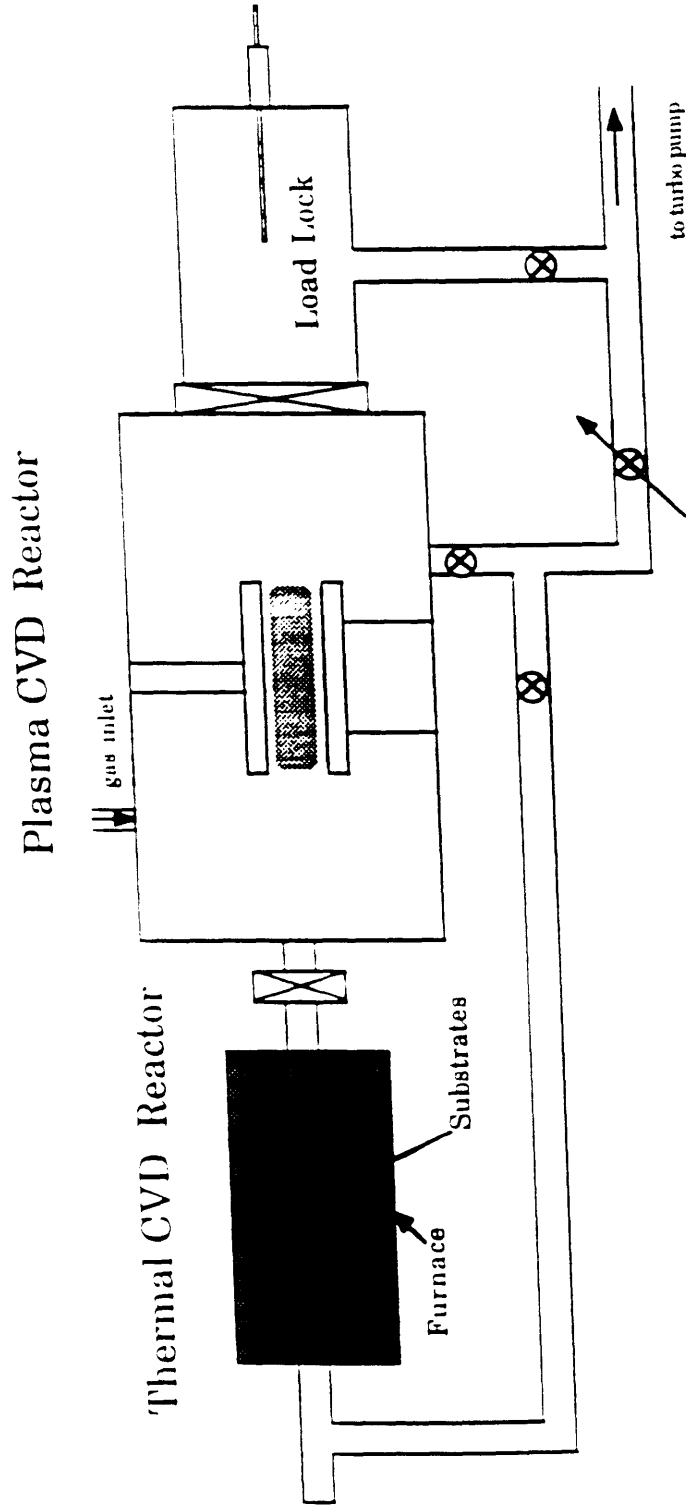
Figure 4.9 Schematic of low pressure CVD reactor connected to the plasma enhanced CVD reactor. The two reactors share gas delivery and pumping systems.

104
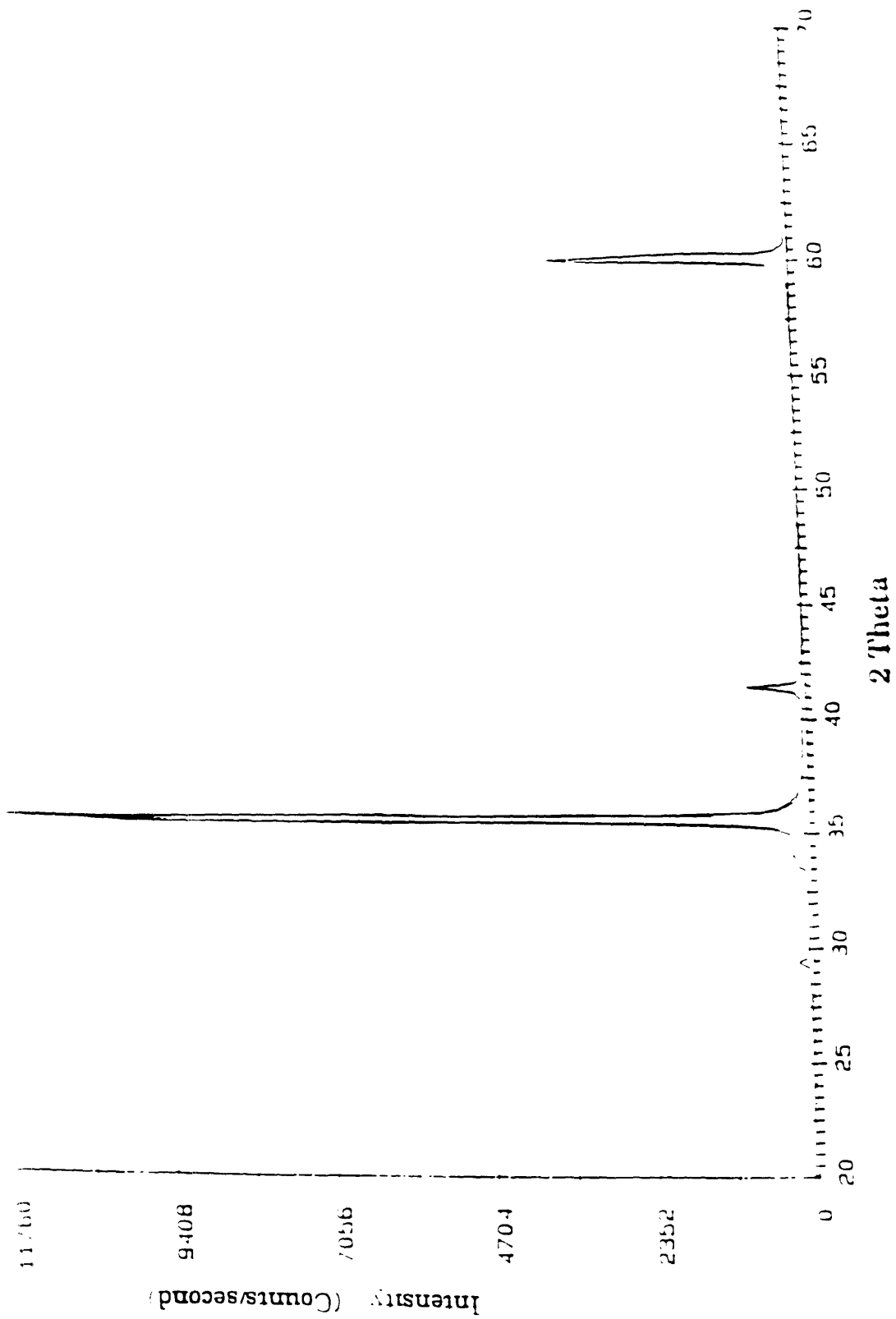
Figure 4.9   Diffracted x-ray intensity versus 2 theta for the SiC substrate
using Cu k-a radiation at 60 kV and 180 mA.

File: StO: CHA051 PFG
Sample:
17-FEB-93 17:53:06
H= 2 K= 0 L= 0

62.5% I_{max}, 1622 cps

87.5% I_{max}, 2272 cps
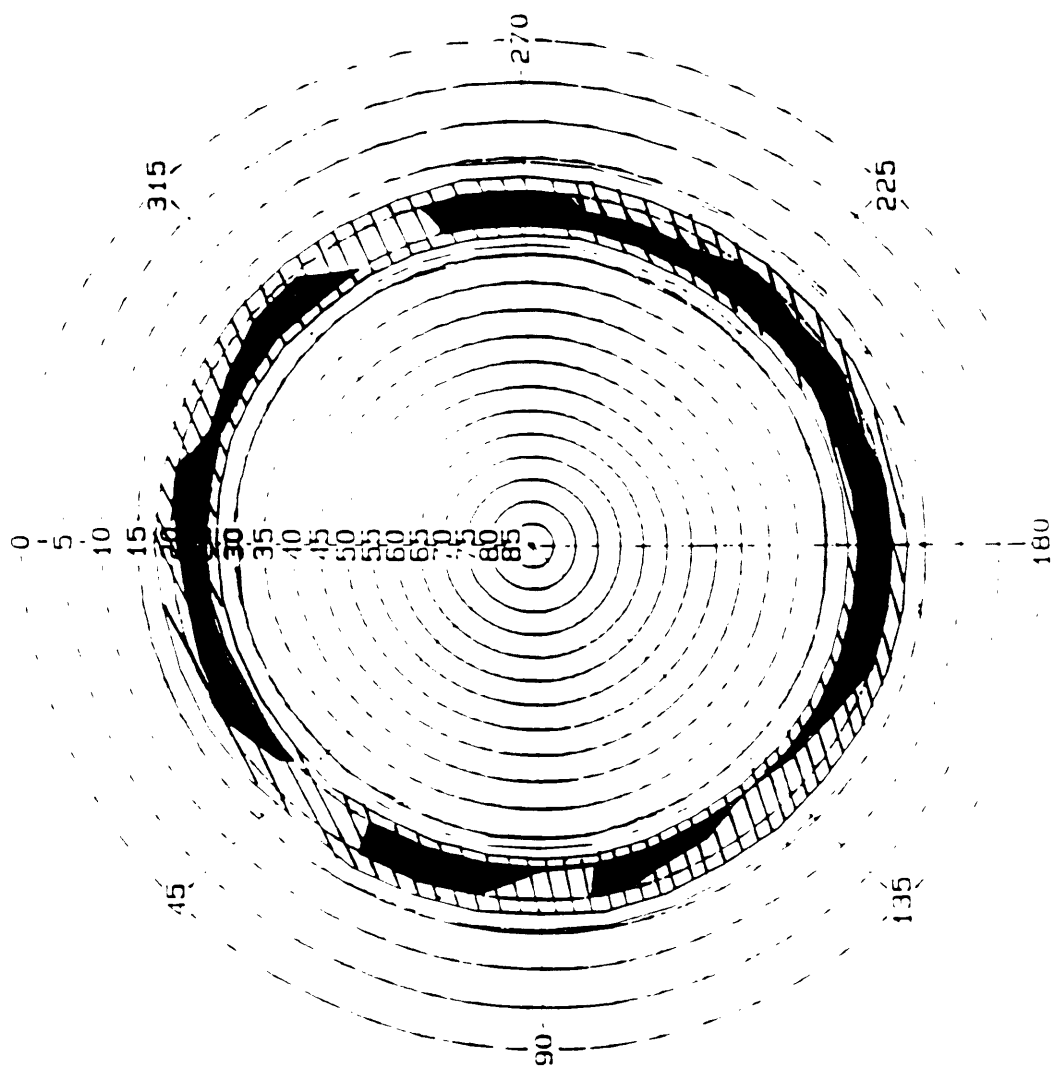
Figure 4.10 X-ray diffraction pole figure for the SiC substrate using Cu k-a
radiation at 60 kV and 180 mA.

106

Relative Intensity for Round and Rectangular Aperatures
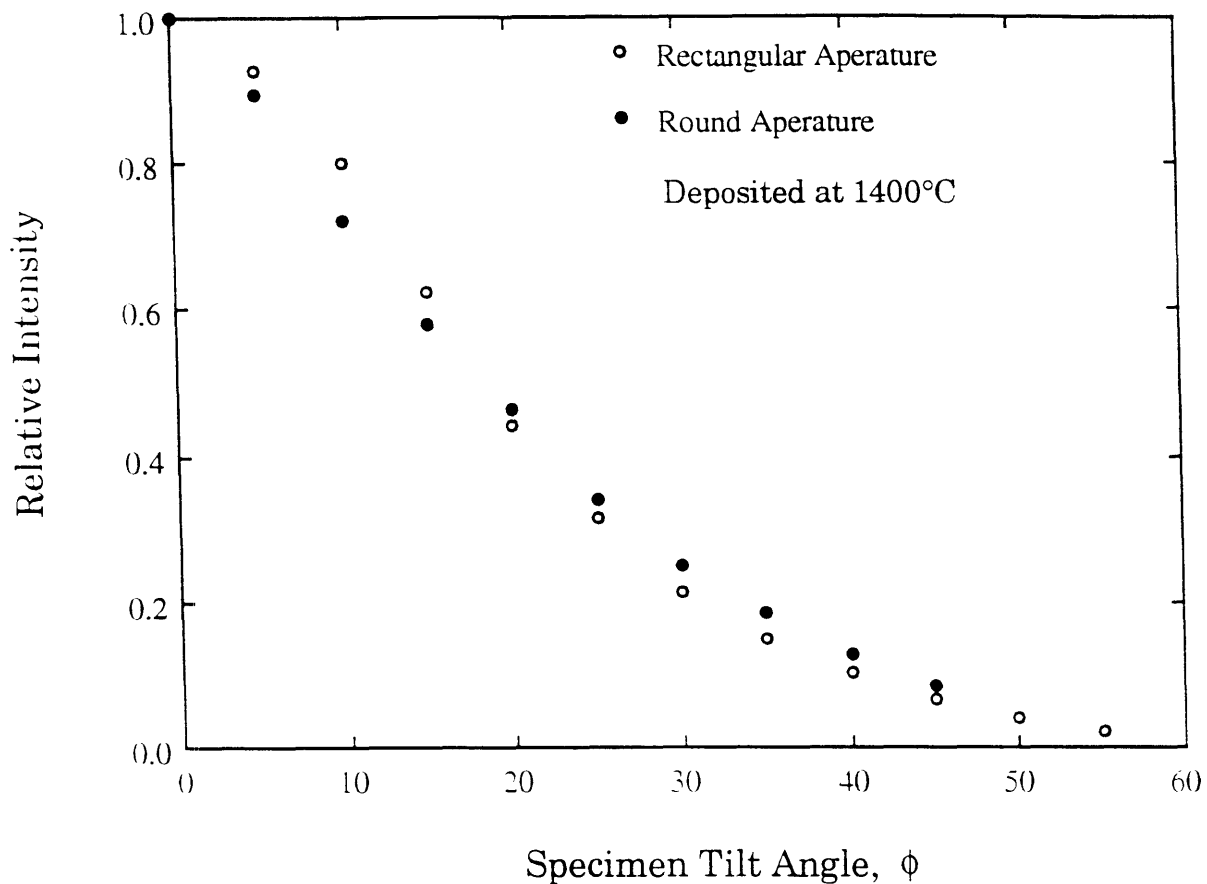
Figure 4.11 Relative diffracted x-ray intensity versus ϕ for carbon deposited at 1400°C on a SiC substrate using both round and rectangular diverging slits on the diffractometer.
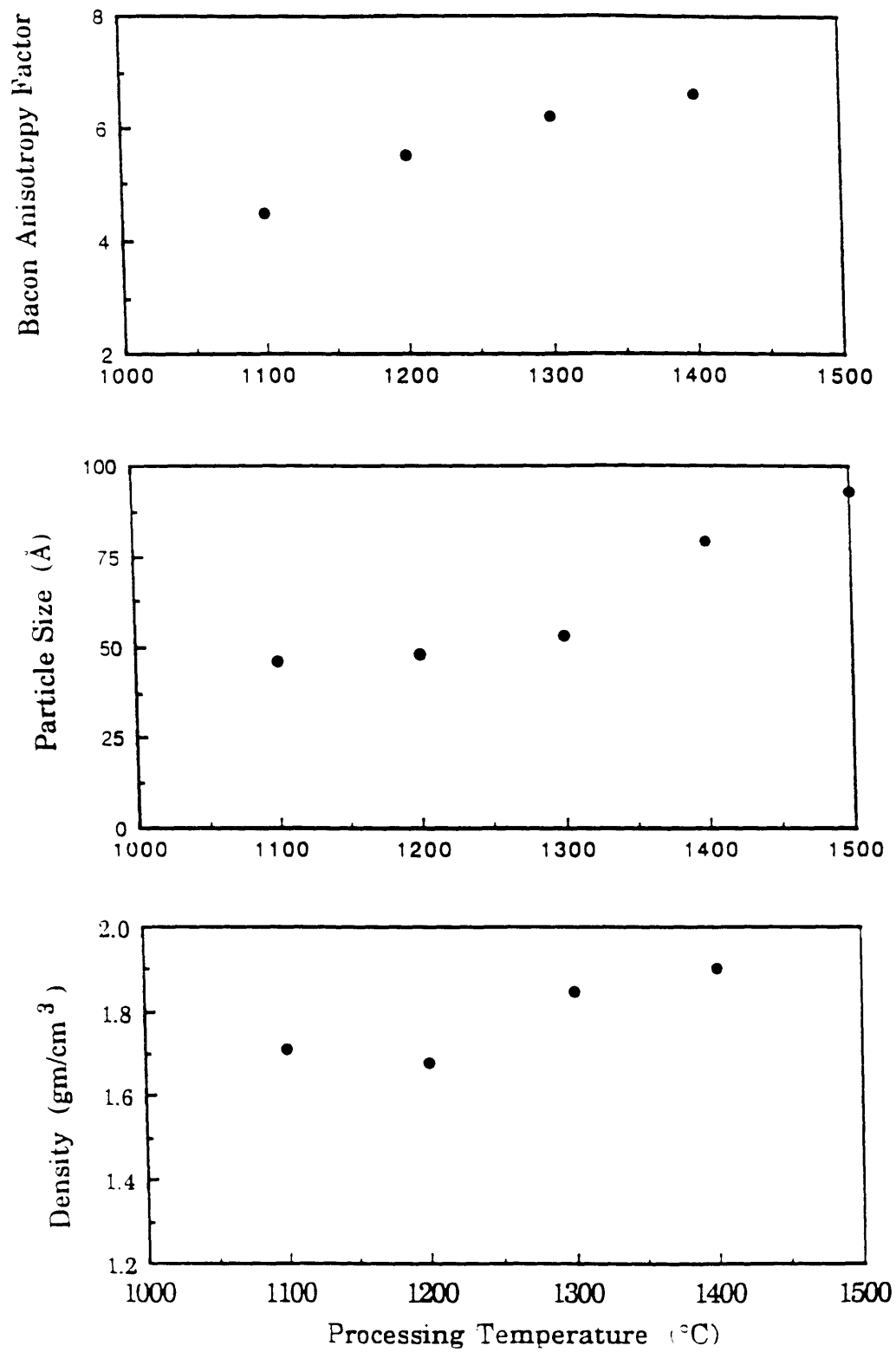
Figure 4.12 Bacon Anisotropy Factor, average crystallite size, and coating
density versus deposition temperature.
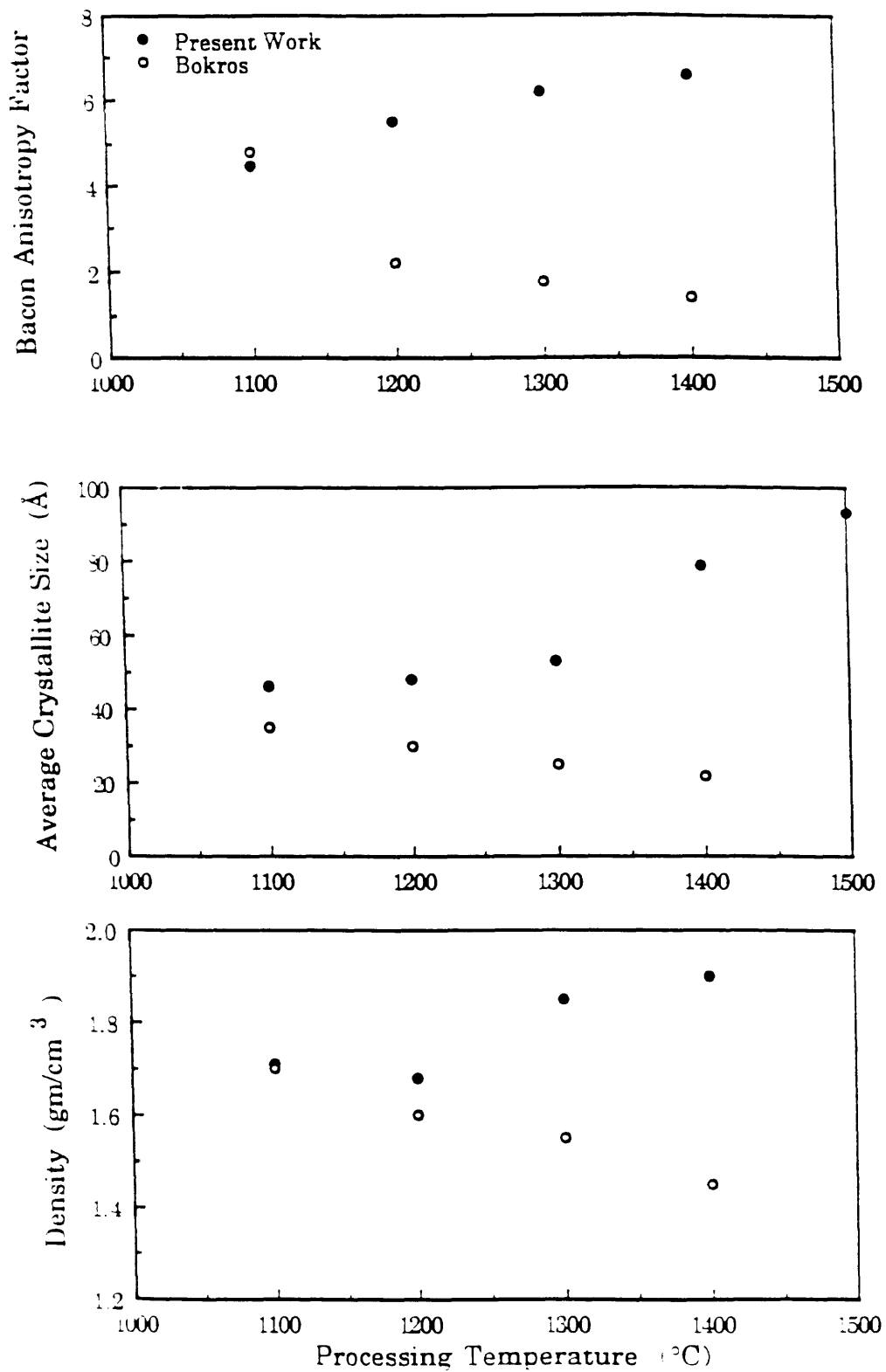
Figure 4.13 Bacon Anisotropy Factor, average crystallite size, and coating density versus deposition temperature from the present work and also from the review of Bokros [9].
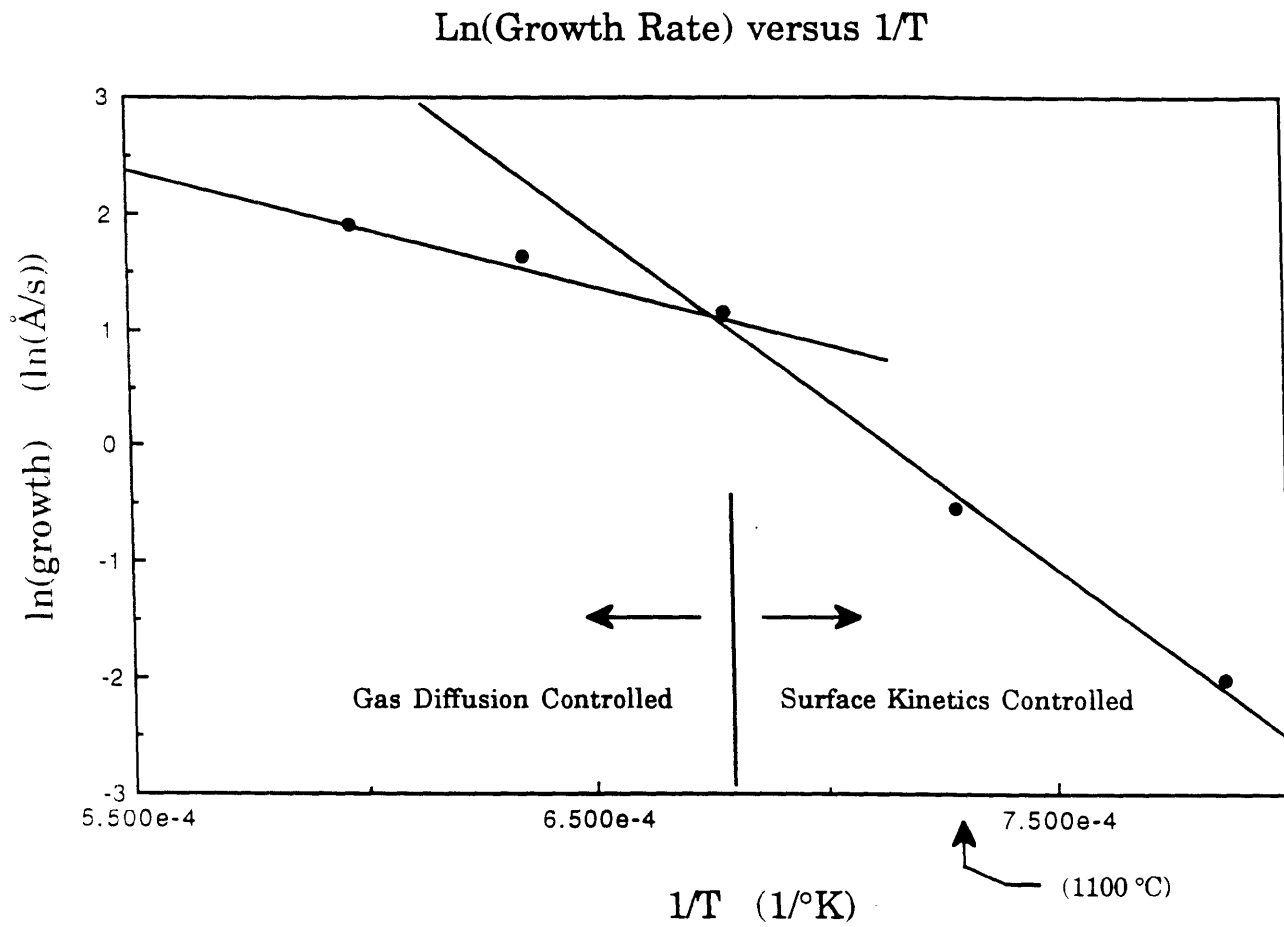
Figure 4.13 The log of the deposition rate versus the inverse of processing
temperature for the LPCVD system at 200 mtorr, 5.0 sccm
propane, and 50.0 sccm argon.

V. Mechanical Evaluation of Couples by Laser Spallation

5.0 Introduction

This chapter will focus on the determimation of the tensile strength of the bimaterial interface between the coating and the substrate of the model couples by a technique called laser spallation. With this technique a short laser pulse induces an elastic shock wave in a substrate which propagates as a relatively short stress pulse. If this stress pulse is of sufficient intensity, a solid film may be spalled from the opposite surface of the substrate when the compression wave turns into a tension wave upon reflection from the free surface. Knowledge of the threshold stress pulse intensity at which coating delamination occurs allows determination of the bimaterial interface strength. This type of interface test is particularly valuable as shock wave loading provides stresses propagating with the speed of sound in the substrate material and can theoretically produce fracture by the collective separation of atomic bonds rather than through crack initiation and propagation as during fracture caused by any other, relatively slow, loading.

The chapter includes two main parts. The first part of the chapter concerns development of the spallation experiment, while the second part presents some experimental results obtained using the developed methodology and a discussion of these results. Please note that before the development of the experiment is begun in this chapter, a general overview of the practical experiment is given.

The development of the laser spallation experiment is also broken into two parts. The first step in the development requires measurement of the induced shock wave peak intensity as a function of laser fluence used to generate the shock wave. The typical spatial and temporal profiles of the generated stress pulse are also determined in this part of the development. The second part of experimental development concerns the mathematical calculation of the propagation and reflection of the experimentally determined shock wave. The functional dependence of the stresses probing the bimaterial interface upon the laser fluence has been calculated. Therefore, results from the first part of the development, coupled with performed calculations, have led to a relation between the threshold laser fluence for delamination and the stresses which were developed at the bimaterial interface for substrates composed of x-cut quartz.

For our use of laser spallation as a measurement tool with substrates other than quartz, the laser-induced pressure shock wave is generated in the substrate of our model interface couples (here single crystal silicon or sapphire) as described above. The generated compressive pressure pulse in the model couple substrate is assumed to be identical to the pulse in the piezoelectric material used previously. Under this assumption the main parameters of the generated compressive pressure pulse are completely determined by the level of laser fluence and are known from the first stage of the experimental development.

5.1 General Outline of Experiment

The set-up is shown schematically in Figure 5.1a and an enlargement of the test specimen in its holder is shown in Figure 5.1b. The test specimen consists of a substrate coated with a test material on one side

and a laser absorbing film on its side facing the laser. In this work the absorbing film is 1.0 μm thick tin deposited by rf sputtering, the substrate was either sapphire or quartz, and the coating was SiC deposited as discussed previously. The coated substrate is pressed against a polished, fused quartz disk that is transparent to laser light. (This quartz disk is used to confine the expansion of the laser absorbing film and should be distinguished from the x-cut piezo electric quartz crystal used to determine the shape of the laser induced shock waves.) A pulse of laser light is emitted from the laser and is focused onto the absorbing film on the reverse of the substrate. The film is rapidly heated upon absorbing the flux of laser energy, melts, and even evaporates, causing a compressive, elastic wave to propagate "forward" into the substrate bearing the coating and also "backwards" into the confining fused quartz disk. See Figure 5.1b. The fused quartz disk confines the expansion of the melting and evaporating layer leading to a sharper stress pulse. The compressive pulse travels through the substrate, bimaterial substrate-coating interface, and then the coating. This compressive pressure pulse reflects from the coating free surface, becomes a tensile pressure pulse, and then loads the bimaterial interface in tension. It is necessary that both materials of the substrate and the coating are non-dissipative, and brittle, with their strength in tension being much lower then their strength in compression. The same must also be true of their interface. It is assumed that the interface is of lower strength then either individual material. The interface strength is determined by relating the threshold laser fluence that causes film delamination to the shock wave intensity at the interface. Figure 5.2 contains two photomicrographs of the delamination of 2.0 μm thick SiC

coatings from a polished sapphire substrate; note the secondary delamination in Figure 5.2b due to residual stress in the coating.

The laser used was a Spectra-Physics DCR-3 operating in the pulse mode with a rise time of 2.5 nanoseconds in the infrared at 1.06μm wavelength. For all experiments cited in this chapter the nominal beam diameter of 12 mm was focused to an average diameter of 1.6 mm at the laser-absorbing surface. The spot size was set using the micrometer on the translation stage upon which the jig containing the test specimen was mounted. The spot size was initially determined by measuring the impact on photographic paper. This spot size determination set the position of the stage holding the test couples. Subsequent variations in spot size would only come from the slight variation due to laser intensity. There was some spot size dependence on total laser fluence. Spot size used in the stress calculations was determined for each impact by measuring the diameter of the melted tin layer.

The experimental method was as follows: The laser was set to a pulse mode at 10 Hz and the energy was measured on the full beam diameter with a Scientech™ 365 power meter with a Scientech™ 3800101 silicon head calibrated at 1.06μm wavelength. These instruments measured the average energy over 10 shots, or over a one second time interval. The energy was recorded and the laser control was switched to the individual pulse mode. The power head was removed from the beam path and a pulse of energy was released into the specimen. The specimen was examined to see if spallation had occurred. The process was repeated until the lowest energy at which delamination occurred was determined. This concluded the test of the interface strength.

Determination of the shock wave intensity and peak shape in x-cut quartz was slightly different from the above procedure and is describe below.

5.2 Experiments with X-cut Piezo-electric Quartz Crystals

The shape and the intensity the shock waves generated by thin film melting and evaporation were measured using piezo-electric quartz. Graham and coworkers [111] have shown that the instantaneous time variant stresses in x-cut quartz electrodes which are in a short-circuit mode produce an instantaneous current that is proportional to stress intensity:

$$\sigma_0 = \frac{l}{fAU_s} i \tag{5.1}$$

where l is the thickness of the crystal, A is the area of impact, U_s is the wave propagation velocity, and f is the piezo-electric polarization coefficient. U_s and f are 5720 m/s and 2.15×10^{-12} $C/m^2/Pa$, respectively for x-cut quartz [111].

The top and side views of the x-cut electrode fixture is shown in Figure 5.3. The x-cut crystal has a 1.0µm tin coating on its front surface and a 0.1 µm gold coating on its reverse surface. The tin coating was deposited by rf sputtering and the gold coating was deposited by electron beam evaporation. During the gold deposition the crystal was masked so that only the center 2.0 cm of the disk surface was coated. This gold coating was used solely as a pick-up electrode and was not a laser absorbing material. Note that a wire is glued to the gold coating with a silver-containing epoxy (Tracon™ Tra-duct 2922). Earlier connections to the gold electrode were made by mechanical contact and found to be a source of

electrical noise in the measurements. The electrical connection between the laser absorbing film and the grounded case of the fixture was enhanced using a silver containing paint to produce a line between the edge of the x-cut quartz crystal and the fixture case across the optical quartz. The access port through which this was done is shown in the top view of Figure 5.3. A Lecroy 1.2 GHz digitizer with a 50 ohm internal impedance was connected to the BNC outlet of the electrode assembly to measure the transient voltage induced by the shock wave.

The shock wave measurement procedure was as follows: The laser beam was focused to a nominal diameter of 1.6 mm at the tin surface. The beam intensity was measured on the unfocused beam with the laser in a 10 Hz continuous pulse mode. The laser was switched to the single shot mode and the power meter was removed from the beam path. A single laser pulse was fired into the tin coating; the digitizer was simultaneously trigged by the laser. The digitizer recorded the transient voltage signal. This information was stored, the digitizer's memory was reset, and the procedure was repeated.

An example of the pulse shape as recorded by the digitizer is shown in Figure 5.4. Results showed this same peak shape regardless of the maximum peak intensity. The voltage peak intensity was used to calculate the peak stress using equation 5.1. The peak stress versus laser fluence is shown in Figure 5.5. The data was found to fit a second order polynomial expression:

$$\sigma_{Peak} = -238 + .00778 \, \Phi - 4.61 \times 10^{-9} \, \Phi^2 \qquad (5.2)$$

where Φ is the laser fluence in J/m^2 and the stress is measured in MPa. This relationship will be used later in the chapter to determine the

116

threshold stress intensity for the sapphire/SiC couples. It is assumed that the peak shape and intensity of the pressure pulse generated at the surface of the substrate is the same for quartz substrates, in which the pulse can measured, as for sapphire substrates, which cannot be measured .

5.3 Laser Energy Absorption and the Absorbing Material

The laser spallation experiment utilizes a pulse of laser energy to deliver extremely high levels of power to small volumes of material in very short time intervals. The delivered energy is partially absorbed and partially reflected. Absorbed energy of the laser pulse generates a number of processes in the energy absorbing material, including melting, vaporizing and ionization [112]. The fraction of the total energy of a laser pulse absorbed in the energy absorbing material depends on absorption characteristics of the surface, which are changing rapidly during all the processes mentioned above. A brief description of the history of processes of absorption is given below.

The laser energy pulse passes through a confining fused quartz disk and reaches the surface of the metallic energy absorption layer. The intense light of a laser beam excites free electrons in the metallic film and these free electrons nearly instantaneously transfer the energy to the lattice [112]). (The time constant of this process is of order of 10^{-14} seconds.) This absorption of energy produces a rapid rise in the "temperature" of a surface layer of nanometer thickness with the exact thickness depending on the specific absorption characteristics of the coating. For example, for 99% pure aluminum, energy absorption is confined to a layer 0.8 nm thick [112]. Because of the small actual thickness of the energy absorbing layer in

metals, the absorbed energy density becomes well in excess of what is needed for melting and evaporation of the impacted area, even taking into account the high initial reflectivity of metallic surface. Therefore, evaporation and subsequent ionization of metal, with the formation of a thin trapped layer of plasma above the metallic surface, rapidly occurs [112]. (The ionization time is estimated to be of the order of 10^{-13}s) The reflectivity of this plasma cloud is much smaller then the cold metallic surface. The absorbtivity is also markedly enhanced due to the development of roughness resulting from the melting and evaporation. As the laser pulse duration (2.5 ns) is very long compared to the ionization time, it may be assumed, that most of the energy is absorbed by the plasma cloud above the illuminated metallic surface. Up to 10^8 watts of laser energy are absorbed in a volume of material of approximately 10^{-12} m^3 generating a highly pressurized plasma that issues out radially in the narrow gap. In this process a pressure pulse of substantial amplitude is generated.

Tin was found to be best suited for use as a laser absorbing material for the present experiments. Gold had initially been used as the laser absorbing material; however, it was determined that with gold it was difficult to produce a pressure pulse of uniformly increasing amplitude with an increase in laser fluence. The gold film reflected much of the initial incident energy until it was heated to its melting point and then it would "explode" in the manner described above. Tin melts quickly and then the liquid metal expands almost linearly with temperature. The volumetric expansion of tin and gold are shown in Figure 5.6. Clearly, the beneficial volumetric misfit occurs with Sn much earlier in time than with Au. The approximate pressure pulse intensity versus laser fluence for a 1.0 μm gold film is overlaid on the tin response curve in Figure 5.7. It is

clear that tin films produce a much more controllable shock wave, especially at the lower fluences used with the test couples containing pyrolytic carbon interlayers.

5.4 Calculation of the Transmission and Reflection of the Shock Wave

The voltage-time profile corresponding to the shock wave in x-cut quartz is shown in Figure 5.4. This profile was normalized and fit to two exponential functions using Matlab™ on Athena™ as is shown in Figure 5.8. The pressure pulse, p(t), normalized by dividing by the peak maximum, is thus described:

$$p(t) = 0 \qquad \text{for} \quad 0 \le t \le 10 \text{ ns}$$

$$p(t) = 1.0 - 0.448 \exp(-.080\, t) \qquad \text{for} \quad 10 < t \le 35 \text{ ns}$$

$$p(t) = 0.648 \exp(-.050\,(t\text{-}34)) + 0.248 \qquad \text{for} \quad 35 < t \le 300 \text{ ns}$$

where t is the time in nanoseconds.

It is seen from Figure 5.8 that the rise time of the shock wave is 25 ns. This implies that the rising part of the shock wave has a spatial length of 250 μm; therefore, the stress at the substrate/coating interface as a function of time will be determined by the superposition of the oncoming shock wave with the wave reflected at the free surface of the coating in an intricate way.

Part of the oncoming shock wave is also reflected at the coating/substrate interface, while further interactions at this interface also occur from the coating side with the reflected wave. Achenbach [113] gives the coefficients of shock wave transmission, C_t, and reflection, C_r, at an internal interface as:

$$C_t = \frac{2\, \rho_c c_c / \rho_s c_s}{\rho_c c_c / \rho_s c_s + 1} \qquad (5.3)$$

$$C_r = \frac{\rho_c c_c / \rho_s c_s - 1}{\rho_c c_c / \rho_s c_s + 1} \qquad (5.4)$$

where ρ_c, ρ_s, c_c and c_s are the densities and speeds of sound in the coating and substrate, respectively.

For the situation in which the substrate and coating had identical density and modulus, the transmission coefficient would be unity and the reflection coefficient zero, and the net tensile stress at the interface would then be simply:

$$\sigma(t) = p(t) - p(t - \tfrac{\delta}{c}) \qquad (5.5)$$

where δ is the coating thickness and c is the speed of sound in the coating.

For the case where the coating modulus and density do not match, the stress at the interface is determined as the sum of reflected components of the original wave:

$$\sigma(t) = C_t \left[p(t) - p(t - \tfrac{2\delta}{c}) + C_r\, p(t - \tfrac{2\delta}{c}) - C_r\, p(t - \tfrac{4\delta}{c}) + C_r^2\, p(t - \tfrac{4\delta}{c}) \dots \right.$$

$$\left. \dots C_r^{n-1}\, p(t - \tfrac{2n\delta}{c}) + C_r^n\, p(t - \tfrac{2n\delta}{c}) \right] \qquad (5.6)$$

This collection of terms is due to the superposition of the shock wave multiple interactiosn of the oncoming and reflected waves with the interface. The wave reflections within the coating are shown schematically in Figure 5.9. Note that for the present situation with sapphire and SiC, C_r is 0.021, so that negligible error is introduced in ignoring second order and larger terms.

Equation (5.6) was evaluated ignoring second order terms using Mathematica™ with δ equal to 2.0 μm and material properties as shown in

120

Table 5.1 for sapphire and SiC [8]. The results are shown in Figure 5.10 where the stress at the interface as a function of time is graphed. It is seen that the interface is first loaded in compression, this load gradually decreases and then the interface is suddenly loaded in tension. The peak tensile stress is shown to be 0.0122 of the peak intensity of the pressure pulse input at the tin absorbing film.

Table 5.1 Selected Properties of Sapphire and SiC

	Sapphire	SiC
Modulus (GPa)	400	460
Density (Kg/m^3)	4000	3200
Speed of Sound (m/s)	10,000	12,000

The peak tensile stress at the interface is such a low fraction of the initial pressure pulses because the thickness of the coating is very small compared to the spatial length of the pressure pulse. As the thickness, δ, is increased, or as the depth from the free surface is increased, the maximum tensile stress of the stress history increases also. This is shown in Figure 5.11 where the maximum tensile stress is plotted versus depth from the free surface. It is seen that the maximum tensile stress increases with depth to 0.6 of the pressure pulse input at 300μm from the surface.

5.5 Results with Sapphire/Carbon/SiC Couples

The test couple is shown schematically in Figure 2.4 and the spalled SiC coating is shown in Figure 5.2. The SiC was processed as described in Chapter 3 and the carbon interlayers, if present, were processed as described in Chapter 4. The results are presented in Table 5.1 and also in

Figures 5.12 and 5.13 Figure 5.12 is a bar graph showing all of the interface

strengths listed in Table 5.1. Figure 5.13 shows the couple strengths for

those containing CVD carbon interlayers with strength plotted versus

Bacon Anisotropy Factor, average crystallite size, and density of the carbon

layer.

Table 5.2 Tensile Strength Results for Various Depositions on Sapphire

Couple	Run	Fluence (kJ/m^2)	Interface Strength (MPa)
SiC/sapphire	682	118.8	10.0
SiC by LPCVD*/sapphire	624	181.0	14.7
SiC/powered carbon/sapphire	680	53.9	2.1
SiC/grounded carbon/sapphire	672	39.6	1.25
SiC/grounded carbon/sapphire	674	42.0	1.21
SiC/1100°C carbon/sapphire	648	47.5	1.00
SiC/1200°C carbon/sapphire	650	40.9	0.81
SiC/1200°C carbon/sapphire	651	42.1	0.81
SiC/1200°C carbon/sapphire	623	41.6	0.73
SiC/1300°C carbon/sapphire	653	35.7	0.62
SiC/1400°C carbon sapphire	676	33.8	0.56

*all SiC coatings except this one were produced by PECVD as describe in

chapter 3.

5.6 Discussion of Results Regarding Sapphire/Carbon/SiC Couples

The tensile strength data of the test couples may be understood by examining the relationship between strength and the test couple interface, or interphase, structure. From Figure 5.12 it is quite clear that carbon interlayers reduce the strength of the interface couple by an order of magnitude from roughly 10 to 15 MPa to 0.5 to 2.0 MPa. It should also be noted that the SiC deposited by low pressure CVD had an interface strength 50 percent greater than the SiC deposited by plasma enhanced CVD. The material deposited at low pressure by thermal decomposition would not contain hydrogen and, therefore, would make more covalent bonds with the surface.

Of the couples with carbon interlayers those containing "powered" or amorphous carbon were the strongest at 2.0 MPa and those containing pyrolytic carbon interlayers were the weakest approaching 0.5 MPa. The couples containing "grounded", or microcystalline, carbon interlayers had a strength of 1.25 MPa and were weaker than those containing amorphous carbon, yet stronger than all of those containing pyrolytic carbon. This makes sense as turbostatic carbon is a transition between the amorphous and pyrolytic structure.

The tensile strength of the model couples is plotted versus the deposition temperature for the carbon deposition in Figure 5.13. The curve is a straight line and shows that the variation in processing temperature does cause a change in tensile strength. This would indicate that the structural change due to the processing variation is either at the interface between the sapphire substrate and the carbon coating or within the coating itself.

If the interface between the sapphire wafer and carbon film has been changed due to the processing, the large decrease in the tensile strength observed would come from either the production of extremely weak bonds or the creation of extremely large flaws. The probable reaction product between sapphire and propane would be aluminun carbide. Aluminum carbide would certainly not be as weakly bonded with either aluminum oxide or carbon to the extent measured. If the weakening of the interface was due to the creation of a flaw, possibly a distribution of carbides or pores, these would be visible as they would have to be of micron or even millimeter size. It is therefore probable that the change in structure responsible for the reduction of couple strength lay within the carbon interlayer.

From the knowledge of the processing / structure relationships determined in the work of chapter 4, a possible explanation for the strength results may be speculated upon. Figure 5.14 shows the strength of the couples versus the structure data obtained at the same processing temperature, but with SiC substrates instead of sapphire substrates; the couple strengths are plotted versus Bacon Anisotropy Factor, crystallite size, and density. The couple tensile strength would then decrease with increasing anisotropy factor, crystallite size, and density; however, only the relationship between strength and orientation seems to be proportional. It is interesting that strength might increase with density. This implies that the decrease in strength is not due to an increase in porosity, that less porous films lead to weaker couples. That couple strength would decrease with an increase in average crystallite size implies that strength decreases with a decrease in grain boundary area. It is therefore suggested that the separation between the planes inside each crystallite consumes a very small amount of the fracture energy and that most of the energy is

consumed between crystallites during the rupture of the nearly amorphous grain boundaries and in changing crack direction between one crystallite and the next. Therefore, if the deposition of carbon on sapphire and SiC are similar, it seems that the strength of the couples most reasonably scales with orientation over a broad, intermediate range of Bacon Anisotropy Factors.

5.7 On the Dissipation of the Shock Wave

Questions have arisen regarding the dissipation of the shock wave as it propagates through the substrate. If the dissipation is negligible, then the reflection problem may be considered one-dimensional in nature and may be solved as above. Lev [114] has numerically calculated the analytical solution of Eason [115] for the problem of the propagation of a shock wave produced by a sudden pressure pulse at the surface of a semi-infinite solid. In his solution the pressure is uniformly applied over a circular area of radius, a, as shown in Figure 5.15a. The temporal profile of the pulse is shown in Figure 5.15b. The results of the numerical calculations regarding the propagation of the shock wave are shown Figure 5.16. The radius and depth are marked in units of 0.05a, where a is the initial impact diameter, and the time is normalized in units of (a/c) where c is the speed of sound in the substrate. Time increments of 0.2, 0.6, 1.2, 1.6, 2.0, and 2.6 are shown in sections a through f.

These figures show that the pressure pulse essentially maintains a uniform shape through time equal 1.2(a/c) to a depth of 1.5 times the initial radius of impact. At a depth of 1.5a and at time 1.2(a/c) three-dimensional dispersal effects and reflections from the surface break up the shock wave's initial shape. For this work, the spot radius used was 0.8 mm with a

substrate 0.5 mm thick. This corresponds to a depth of 0.625 the initial radius of impact. In summary we may say that for the test couples conducted in this work, the propagation and reflection of the pressure pulse may be considered as one dimensional.

5.8 Summary

A method to test the strength of an interface between a coating and a substrate by way of laser induced shock waves has been developed. This technique has been applied to evaluated model couples for inorganic matrix composite applications. It has been determined that insertion of carbon interlayers into sapphire/SiC couples reduces the strength of the couple by roughly an order of magnitude from 15 MPa to less than 2.0 MPa. Furthermore, the strength of couples with carbon interlayers has been correlated with the structure of the carbon in the interlayer with the strength of the couple inversely proportional to the degree of orientation in the carbon. It has been demonstrated that interfaces with strengths ranging over an order of magnitude may be synthesized through thin film processing techniques; however, all of the test couples produced had tensile strengths significantly less than those proscribed by theory to maximize composite transverse strength while maintaining composite toughening through controlled interface delamination.

Laser

Lense

(a)

Specimen
Fixture

Shock Wave

Optical Quartz

Sapphire

SiC Coating

Sn Film

Laser Fluence

(b)
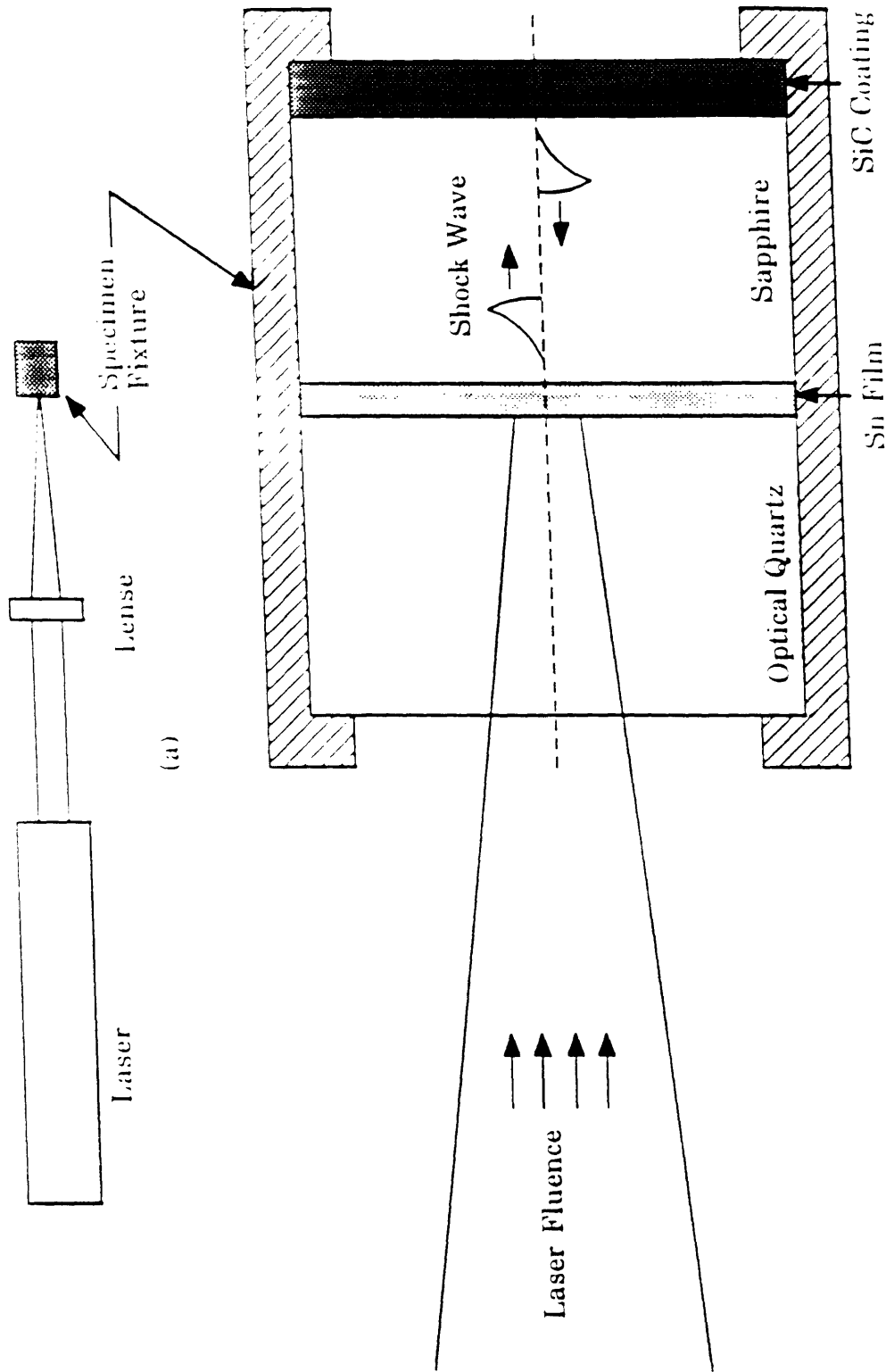
Figure 5.1 Schematic of experimental set-up of the laser spallation experiment; (a) shows the laser, lens, and specimen on the lab bench, and (b) is an enlargement of the specimen in its holder.

(a)
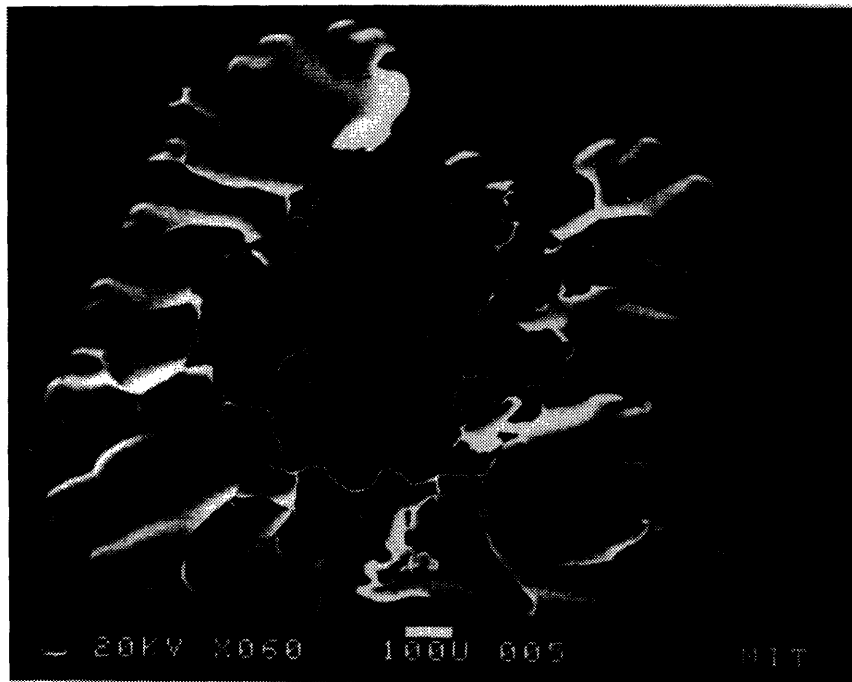
(b)

Figure 5.2   Photomicrographs of SiC spalled from polished sapphire without
and with substantial residual stress in the SiC coating.

Optical quartz visible to silver
paint Sn film to grounded case

O-ring

Wire

BNC
Connector

Conductive Epoxy

Gold Pick-up Electrode

X-cut Quartz

Sn Absorbing Film

Optical Quartz

(a) Side View

(b) Top View
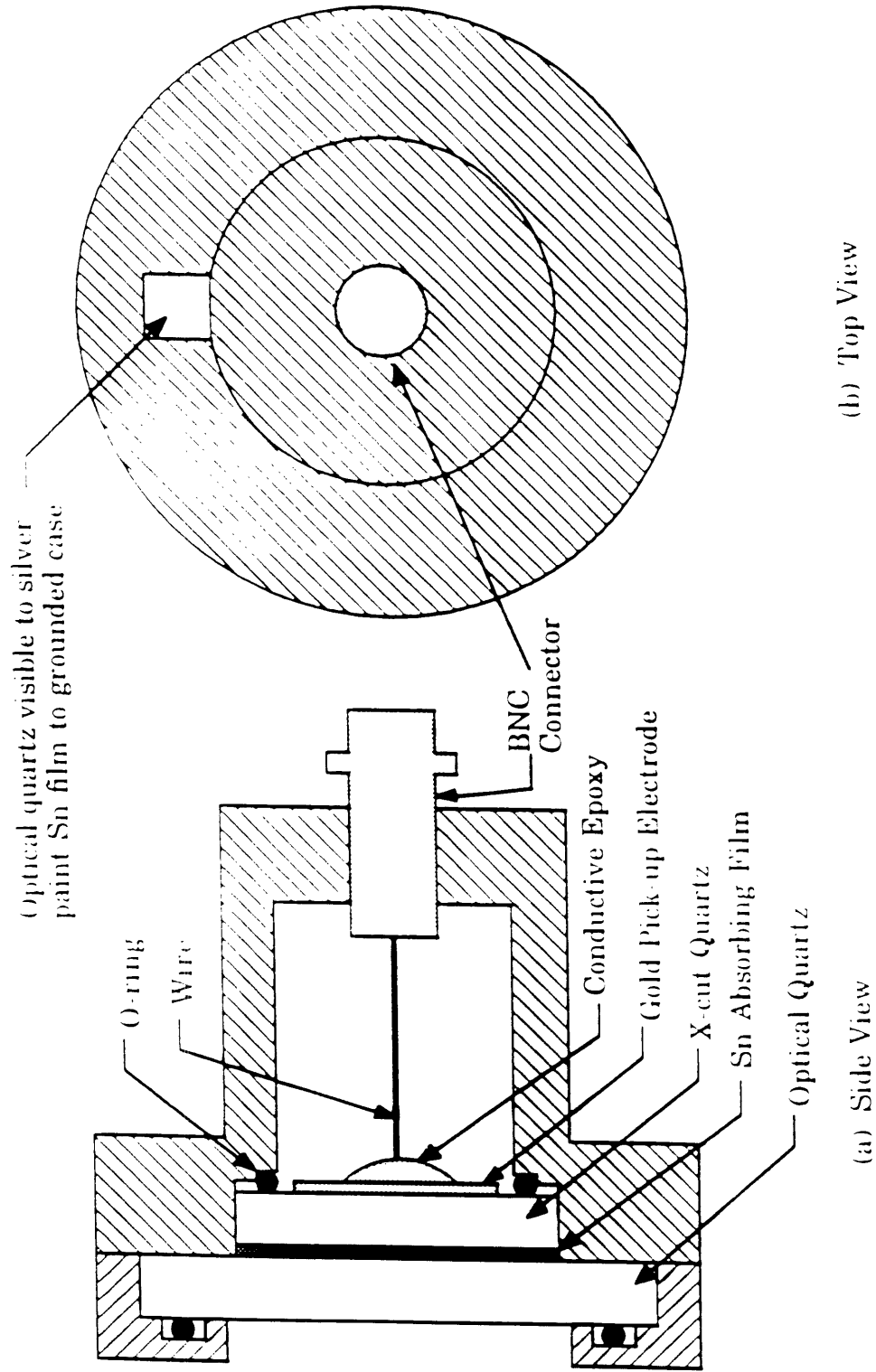
Figure 5.3   Schematic of electrode containing piezo-electric x-cut quartz.

129

Piezoelectric Displacement Voltage for a Laser-Induced Shock Wave
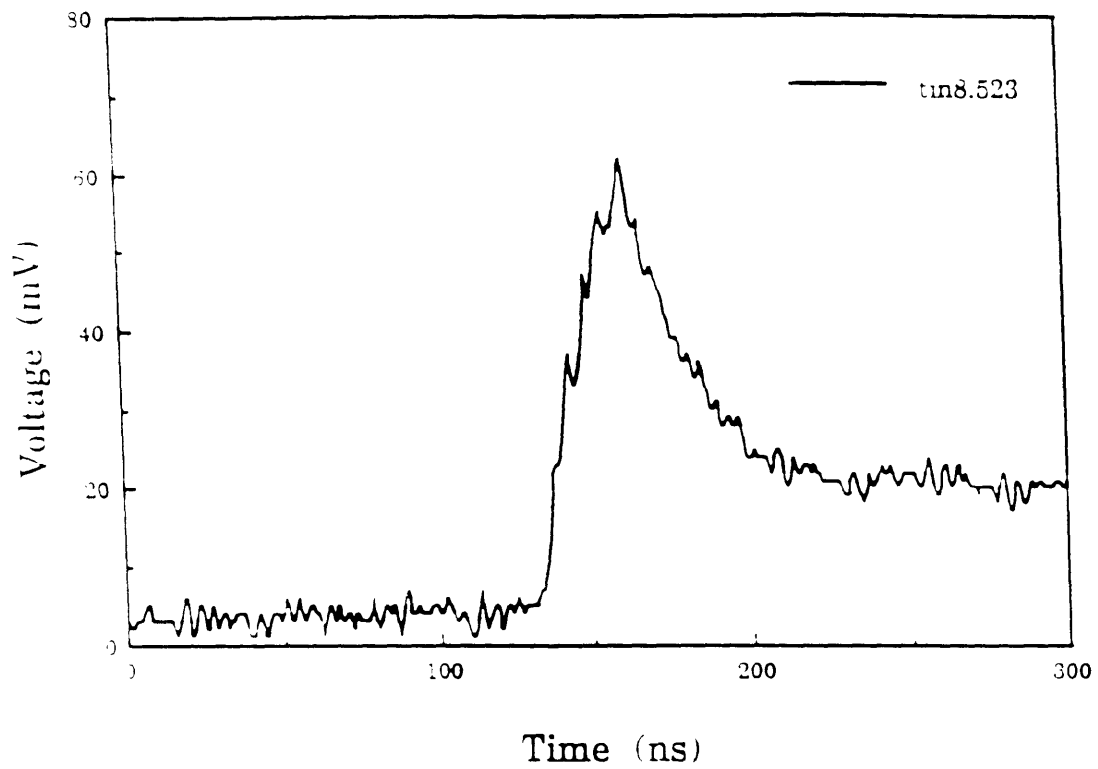
Figure 5.4 A typical voltage peak from the piezo-electric quartz electrode showing the pressure pulse generated upon laser impact.

Peak Stress in X-Cut Quartz versus Laser Fluence
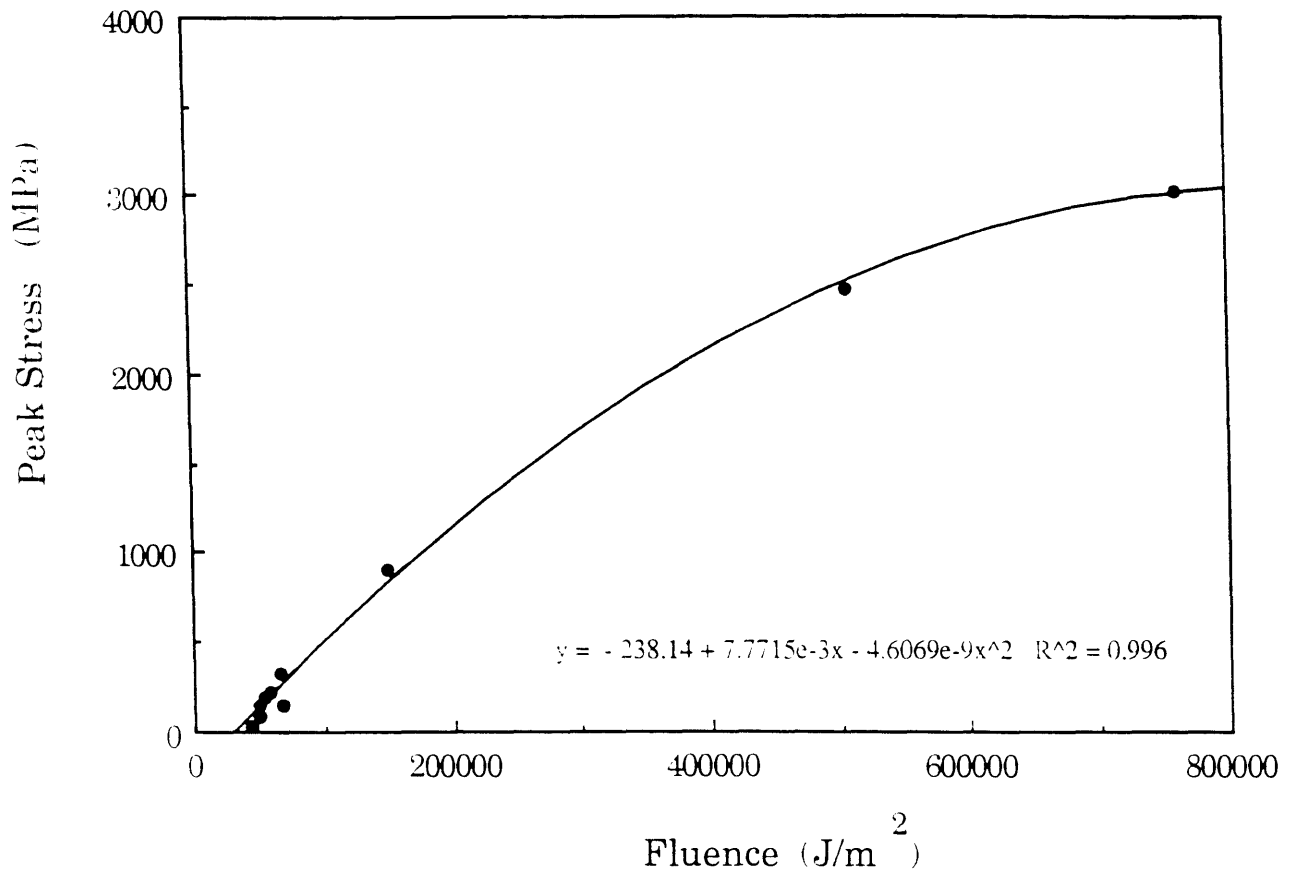
Figure 5.5   Peak stress generated in the piezo-electric electrode as a function of laser fluence.
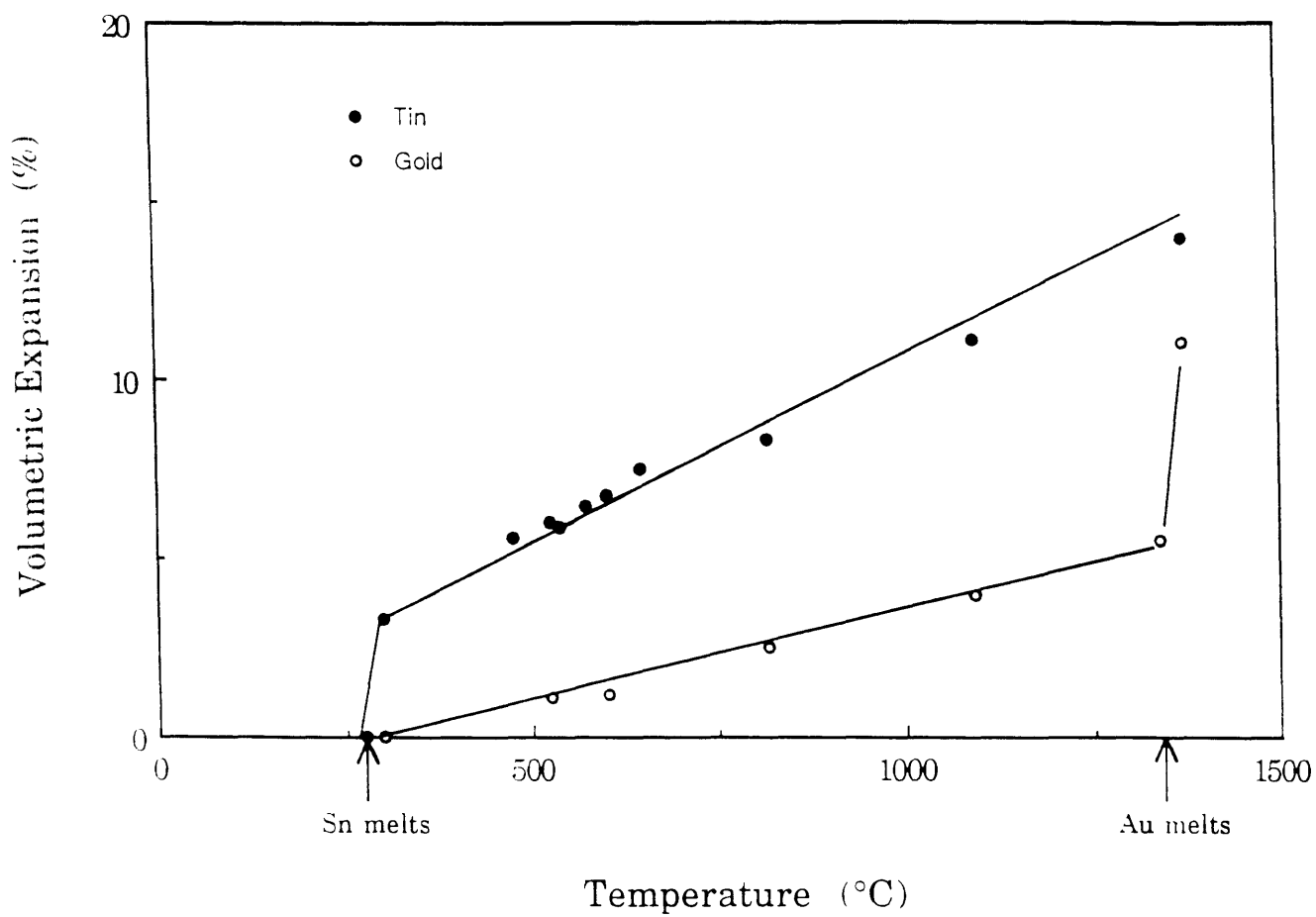
Figure 5.6 Volumetric expansion of tin and gold as a function of temperature.

Comparison of the Response of Gold and Tin to Laser Illumination

Approximate response with
a gold absorbing film

Peak Stress (MPa)

● Tin

· Approximate Gold Curve

Fluence (J/m ^{2})
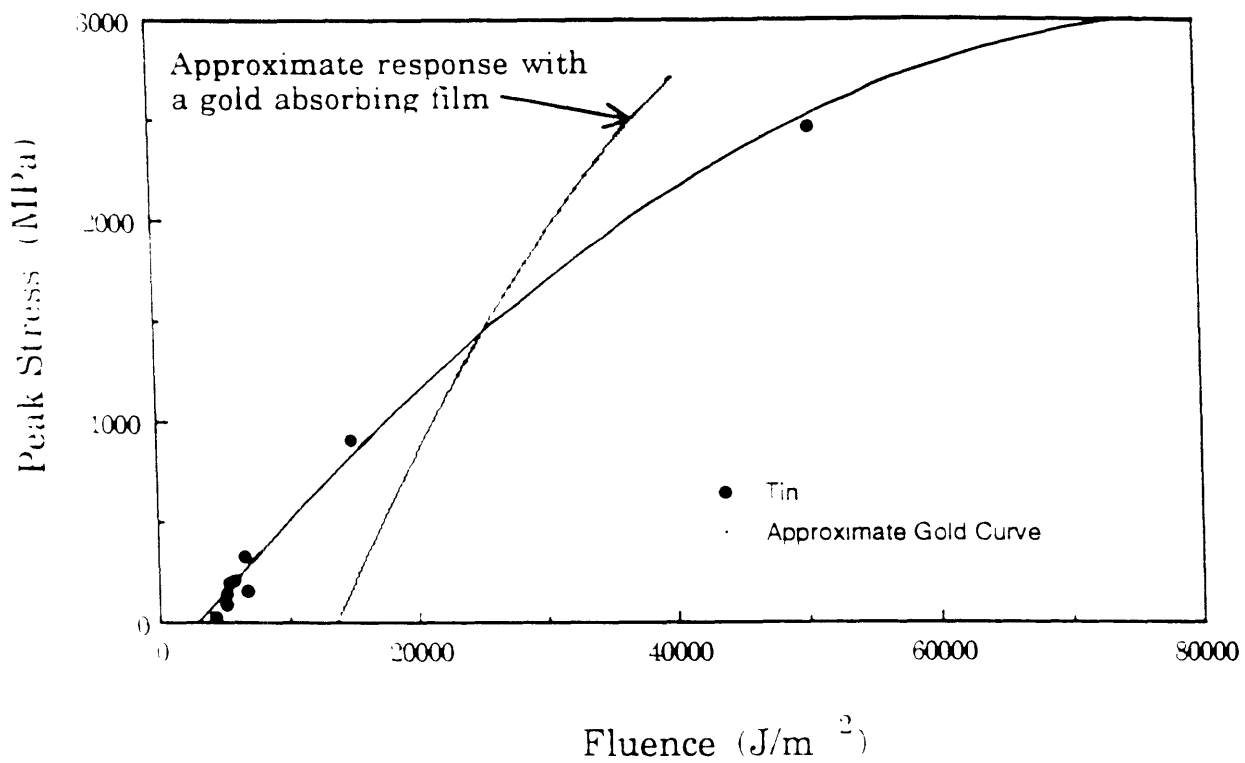
Figure 5.7 A comparison of peak stresses in the shock waves produced by
laser impact into both tin and gold absorbing films. The curve
representing the response of gold films is an approximation
based upon results with sapphire, not x-cut quartz, substrates.

A Normalized Pressure Pulse Produced with a Tin Coating
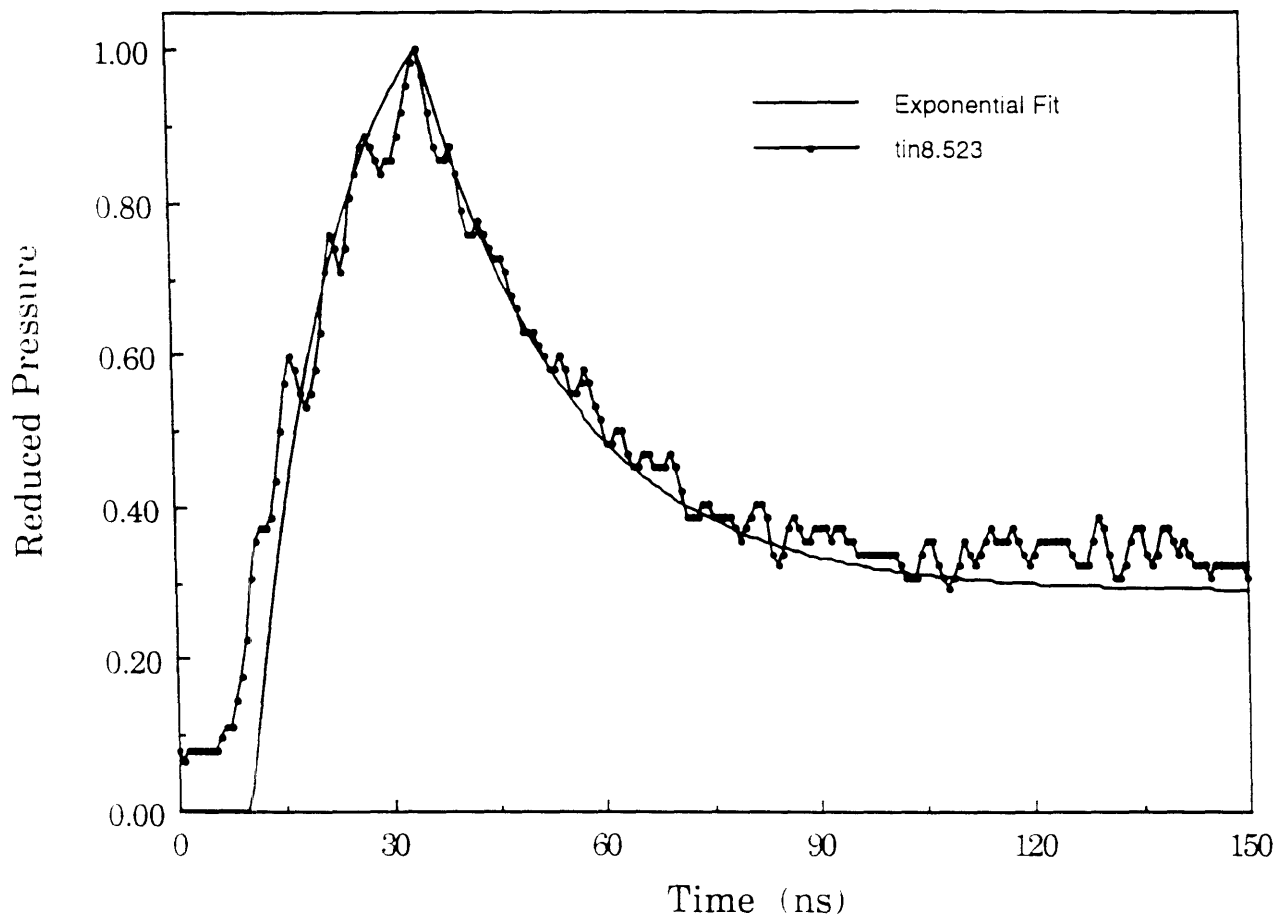
$$p(t) = 0 \qquad \text{for} \quad 0 \leq t \leq 10 \text{ ns}$$

$$p(t) = 1.0 - 0.448 \exp(-.080\, t) \qquad \text{for} \quad 10 < t \leq 35 \text{ ns}$$

$$p(t) = 0.648 \exp(-.050\,(t\text{-}34)) + 0.248 \qquad \text{for} \quad 35 < t \leq 300 \text{ ns}$$

Figure 5.8 A normalized pressure pulse and exponential curve fit.

$$\sigma(t) = C_t \left[p(t) - p(t - \tfrac{2\delta}{c}) + C_r\, p(t - \tfrac{2\delta}{c}) - C_r\, p(t - \tfrac{4\delta}{c}) + C_r^2\, p(t - \tfrac{4\delta}{c}) \cdots \right.$$

$$\left. \cdots C_r^{n-1}\, p(t - \tfrac{2n\delta}{c}) + C_r^n\, p(t - \tfrac{2n\delta}{c}) \right]$$

Figure 5.9 Schematic showing internal reflections within the coating and the equations describing them.

Stress at the Interface Versus Time
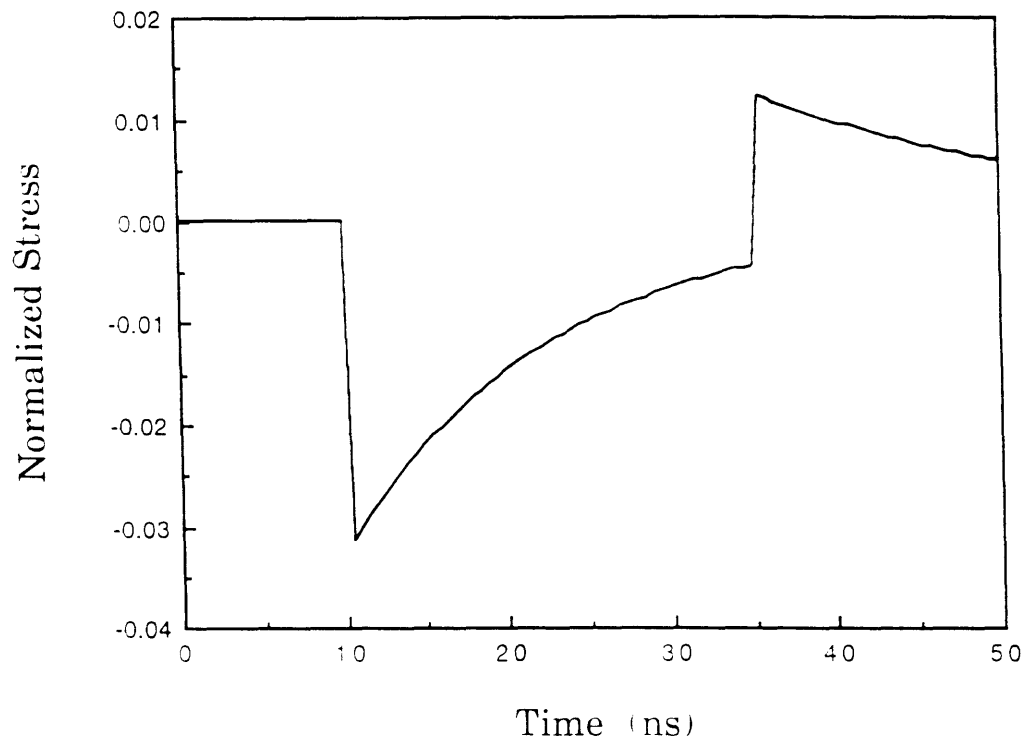
Figure 5.10 The stress history at the interface due to reflection of the shock wave.

Maximum Stress Versus Depth From Free Surface
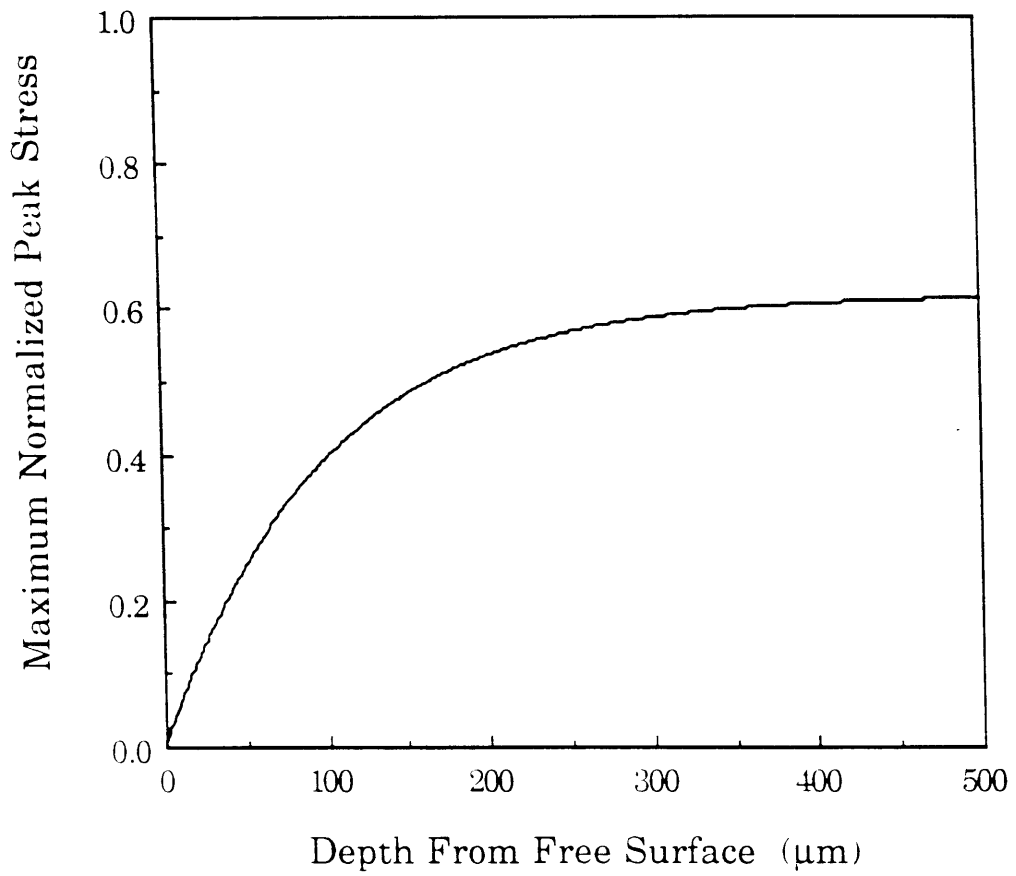
Figure 5.11 Maximum stress experienced in the substrate or coating
versus depth from the free surface.

Tensile Strengths for Various Couples
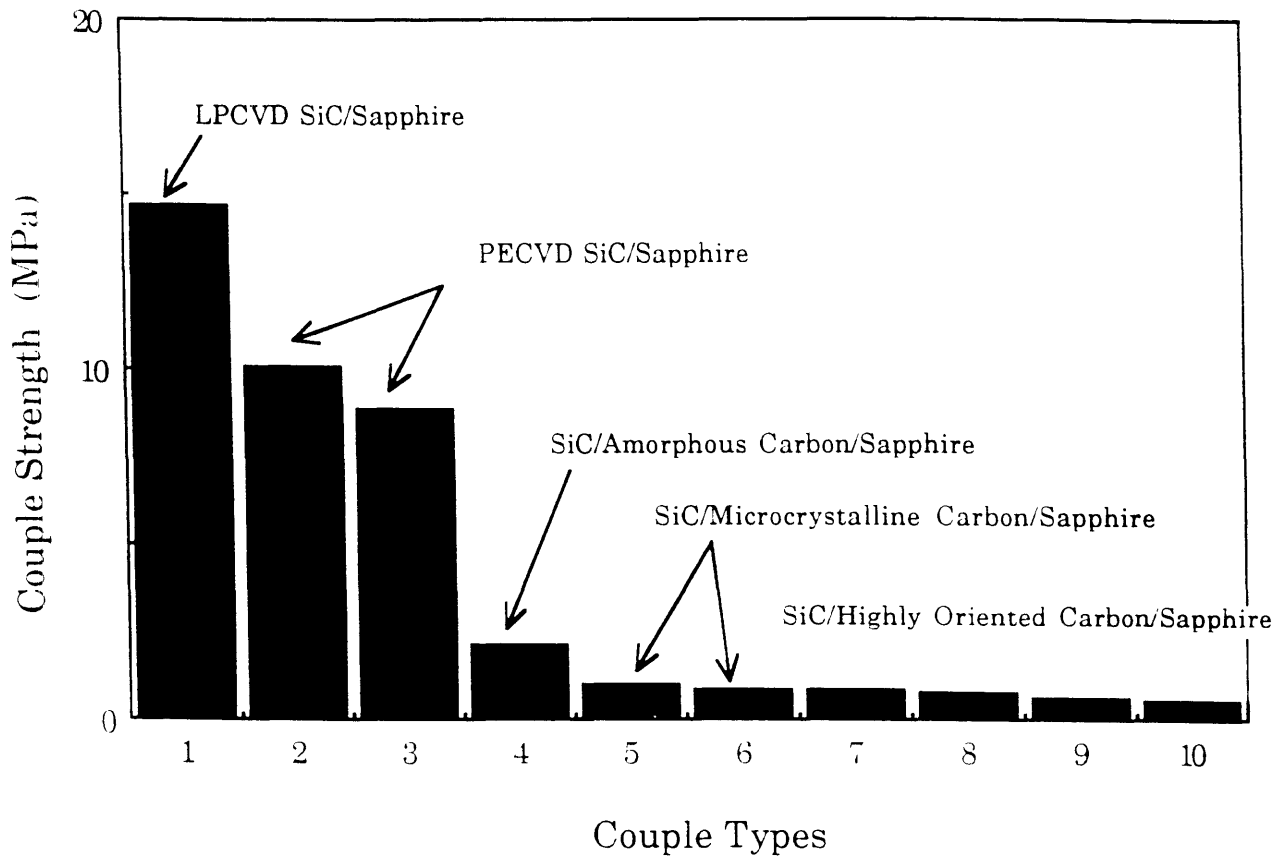
Figure 5.12 Tensile strengths for the various couples with and without
carbon interlayers.

Couple Tensile Strength Versus Carbon Processing Temperature
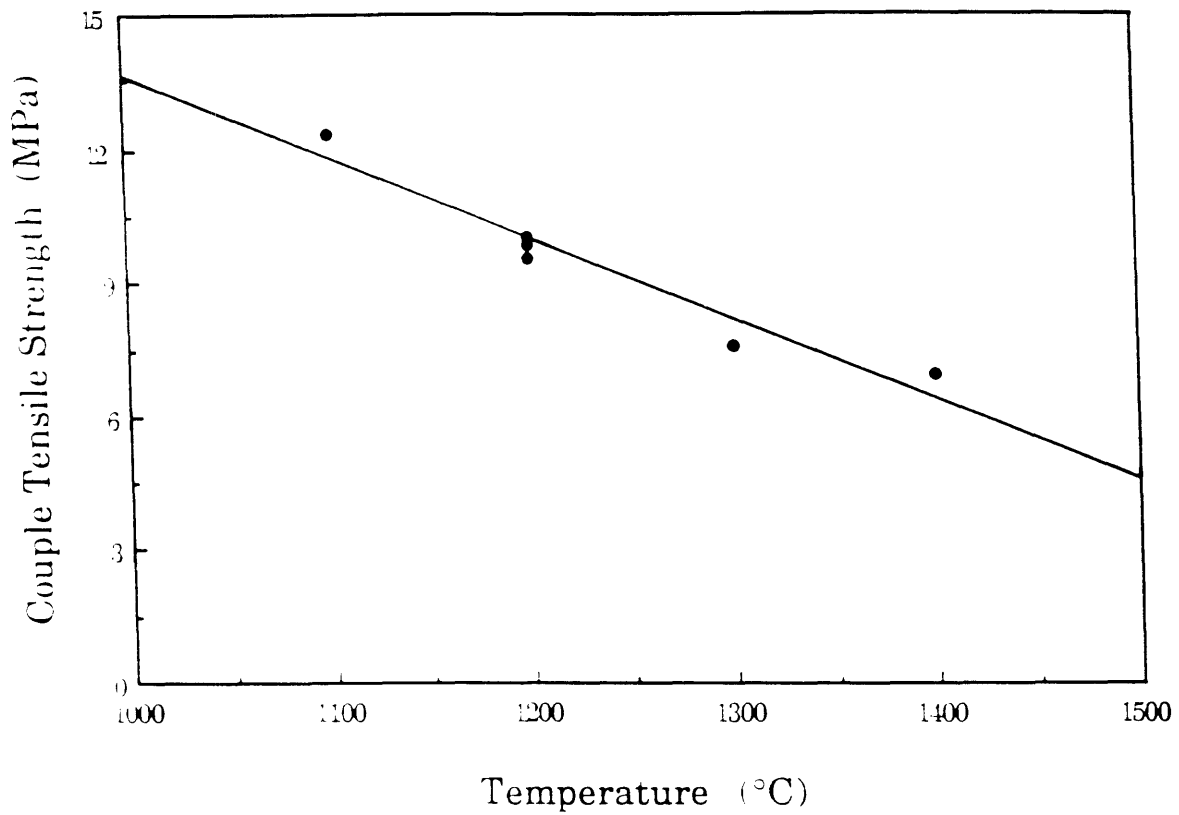
Figure 5.13   Tensile strength of the model couples versus deposition
temperature during processing of the carbon interlayer
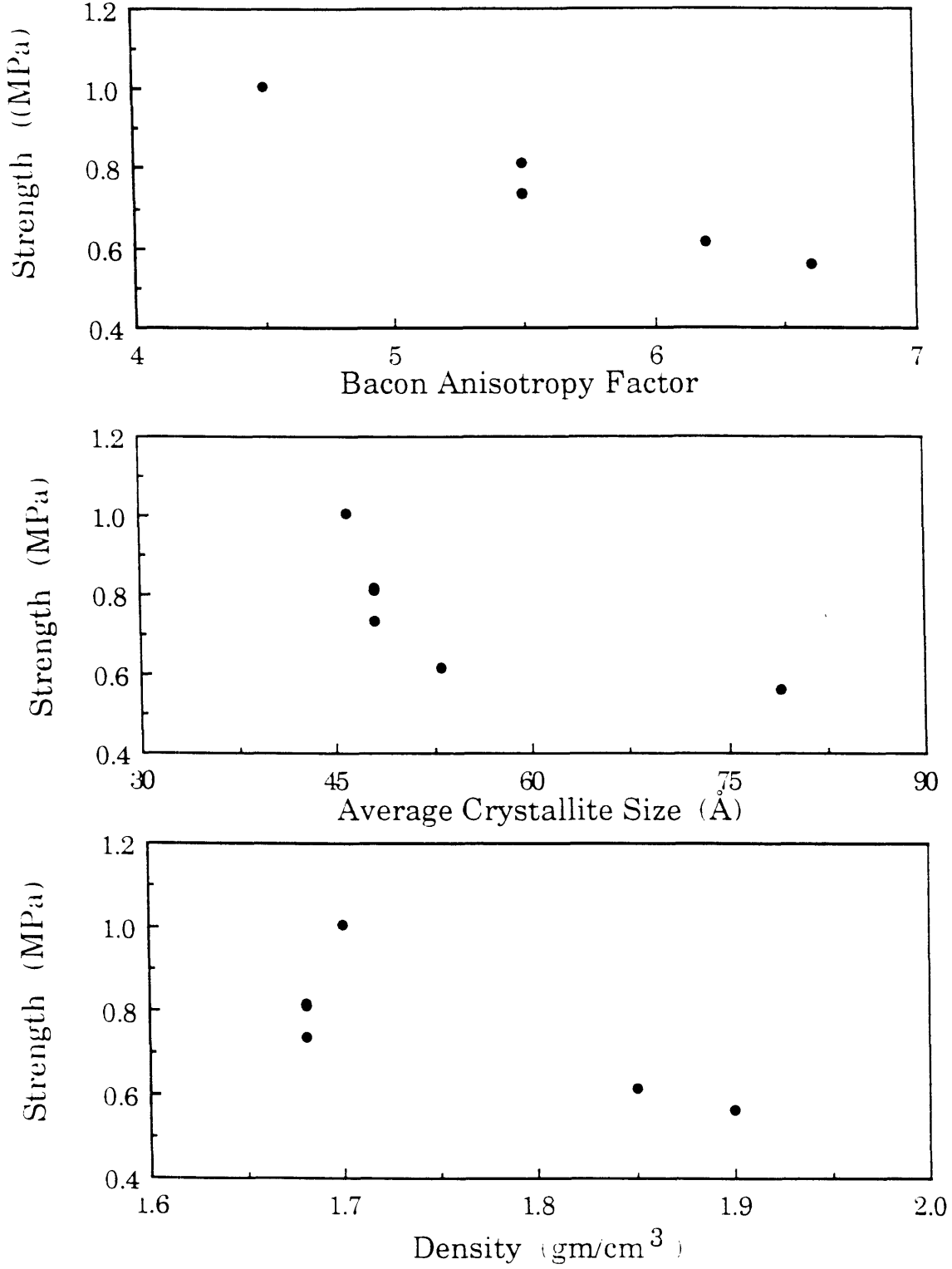
Figure 5.14 Couple tensile strength versus orientation (BAF), average crystallite size, and density of the LPCVD carbon material deposited on SiC.

Pressure Pulse

|←—2a—→|

(a)

Pressure

1.0
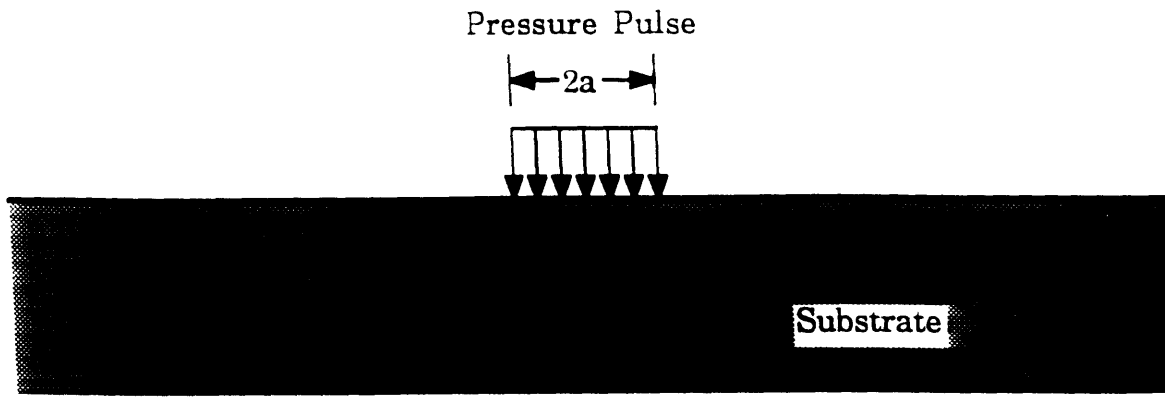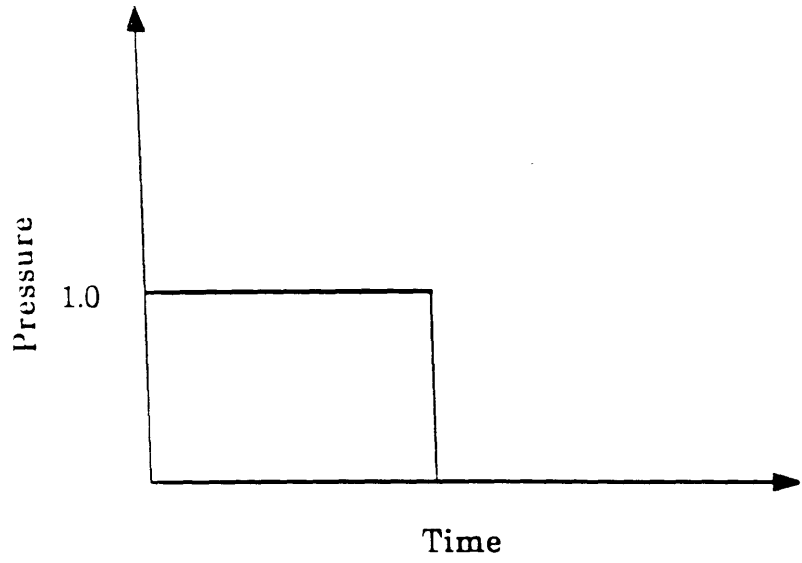
Time

(b)

Figure 5.15 Schematic showing the pressure pulse shape and temporal history used in the calculations of Lev.

Normalized Stresses as a Function of Time, Radius, and Depth
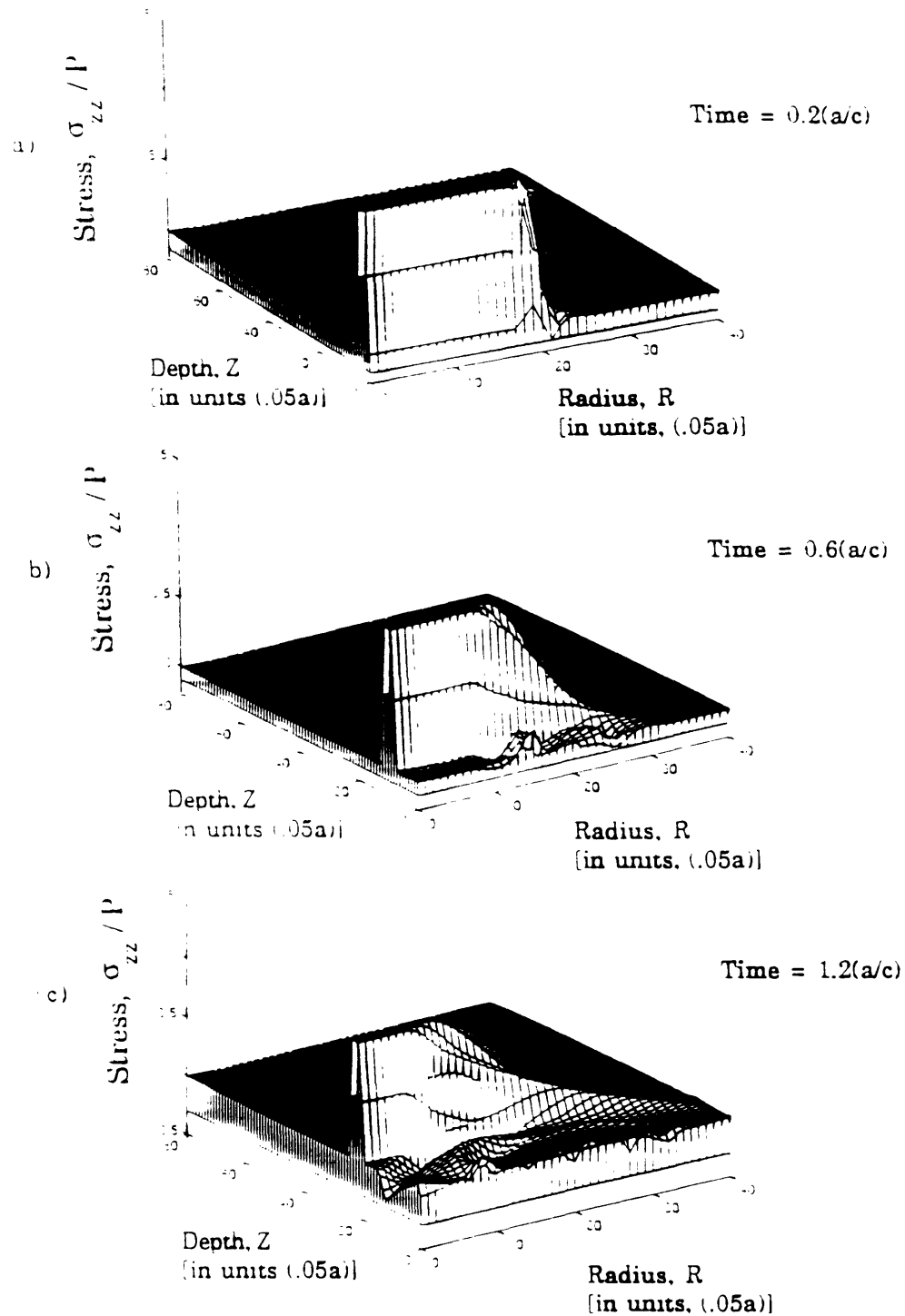
Figure 5.16 Normalized stresses as a function of radius and depth at times, T=0.2, 0.6, and 1.2 (a/c) due to a uniform pressure pulse applied to the substrate surface.

Normalized Stresses as a Function of Time, Radius, and Depth

(d) Stress, σ_{zz}/P

Time = 1.6(a/c)

Depth, Z
[in units (.05a)]

Radius, R
[in units, (.05a)]

(e) Stress, σ_{zz}/P

Time = 2.0(a/c)

Depth, Z
[in units (.05a)]

Radius, R
[in units, (.05a)]

(f) Stress, σ_{zz}/P

Time = 2.6(a/c)

Depth, Z
[in units (.05a)]

Radius, R
[in units, (.05a)]
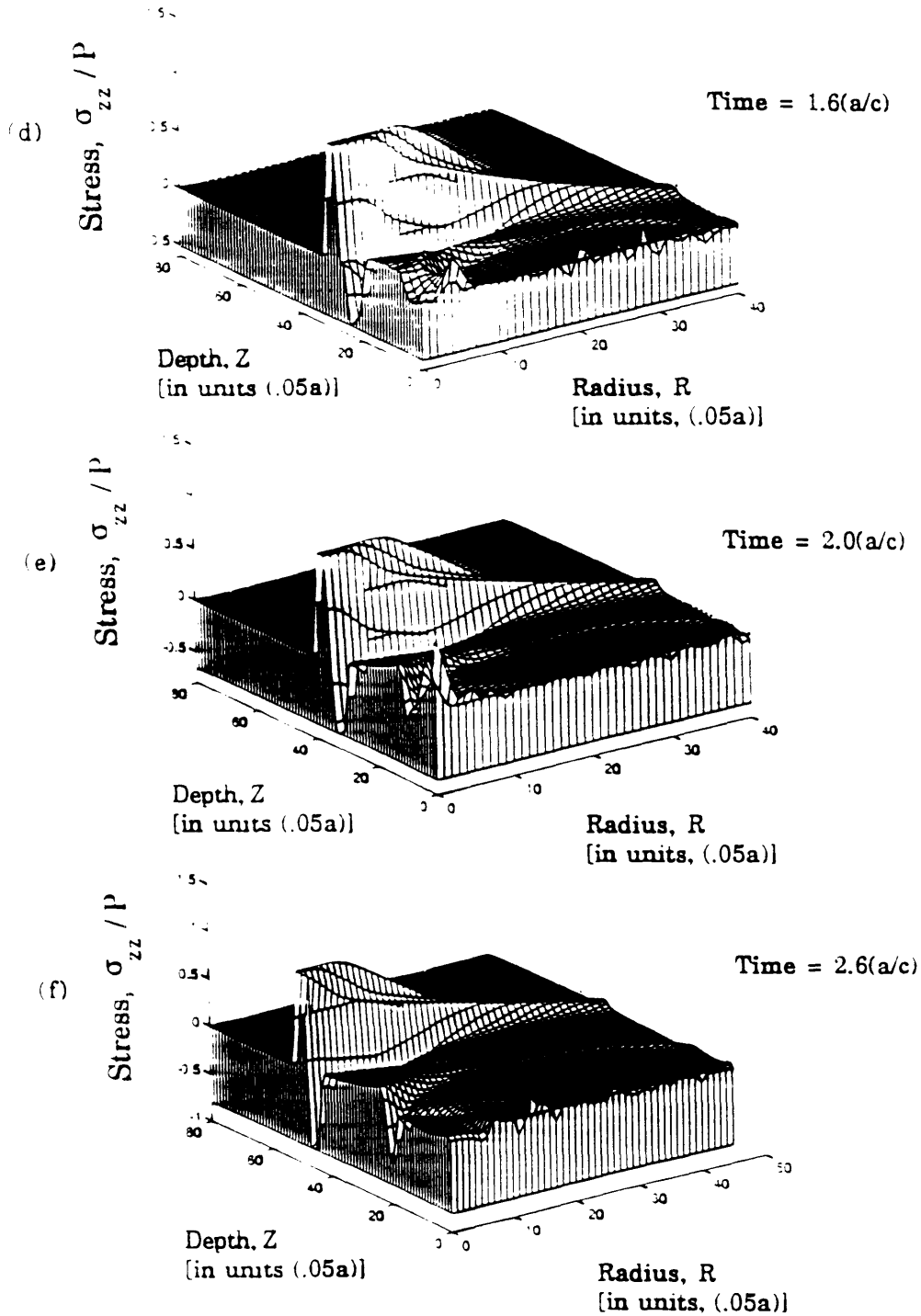
Figure 5.16   Normalized stresses as a function of radius and depth at
times, T=1.6, 2.0, and 2.6 (a/c) due to a uniform pressure pulse
applied to the substrate surface.

Discussion

The original intent of this project was to process flat specimens that would be representative of the interfaces in composite materials. The target properties were provided by mechanistic considerations which prescribed the material properties for composite optimization, i. e. maximizing transverse strength while maintaining axial fracture toughness. The processing developments encompassed the production of a stable overlayer, representing the chemically inert layers often used in composites, and the manipulation of an interlayer between the inert layer and the fiber which would act as the mechanical fuse required for composite toughening.

The above directions actually necessitated carrying out three separate projects simultaneously, followed by bringing them together at the end. The developments of the first project were presented and covered the production of SiC coatings by PECVD which would represent the inert layer in composite materials (Chapter 3). The second project consisted of an investigation of the processing / structure relationships in the deposition of carbon by low pressure CVD which would represent the interlayer acting as a mechanical fuse (Chapter 4). And the third project encompassed the development and use of laser spallation as an experimental technique for measurement of interface strengths (Chapter 5). Only after these projects were completed could complete model interface systems be synthesized. Each of these three projects were deemed successful by themselves; however, the combination of all three projects toward the overall goal was not fully conclusive because of the additional unknowns introduced with the

necessity to use two types of substrate materials. Moreover, the final levels of interface tensile strength that were achieved were not completely satisfying viewed in light of the design criteria.

The strength of the strongest model interface couple was measured to be almost two orders of magnitude less than the desired strengths determined in Chapter 2 for composite optimization. Interface design considerations delineated by Argon and Gupta [6] specified desired interface strengths of 95 MPa and 825 MPa for SiC coatings deposited onto carbon pitch-55 and sapphire fibers, respectively. These interface strengths would maximize composite transverse strength while still allowing for composite toughening by permitting the operation of the interface delamination/crack bridging mechanism. The highest coating/substrate strength measured was 14.7 MPa for the LPCVD SiC on sapphire. While interfaces with these strengths would surely protect the fibers from cracks in the matrix, composite transverse strength would be unduly compromised. It should also be noted that these results indicate that a composite with fibers coated only with SiC, without a carbon interlayer, would actually perform better as a fuse than a composite utilizing any of the carbon intermediate coatings.

Furthermore, it is not clear that carbon deposited by any CVD technique will meet all of the desired specifications. The ideal interface for composite toughening as envisioned at the beginning of this research is shown schematically in Figure 6.1a. The carbon crystallites were to be sufficiently random that the transverse strength met the design requirements and the weak planes in the crystallites would act as paths deflecting cracks along the fiber. In this way both the strength and energy requirements for crack deflection would be met. However, from the plot in

Figure 4.5 of elastic modulus versus the angle ϕ between crystallographic direction and the c-axis of the crystallites, and from the tensile strength results achieved in this research, it is clear that in order to attain the strengths required for composite optimization most of the crystallites would have to be oriented with their c-axes parallel to the fiber as shown in Figure 6.1b.

This latter orientation would present two problems. If the bulk of the crystallites were oriented with their layers perpendicular to the fiber as shown in Figure 6.1b to optimize transverse strength, the weak planes would direct the crack into the fiber. The path directly to the fiber would offer the least resistance to cracking. Also, it is not clear that carbon has ever been deposited by thermal decomposition with the strongest layers consistently perpendicular to the substrate. The hexagonal rings of hydrogenated carbon molecules that form in the CVD process tend to lie flat with respect to the deposition surface and the known spectrum of orientations ranges from all crystallites laying parallel to the surface to a random distribution of orientations of crystallites.

The connection between the processing / structure part of this work and the structure / property part could be made conclusive by closely examining the carbon interlayers in the test couples themselves. This could not be done in the first place because only a very thin film of carbon could be desposited on sapphire before the film peels from the substrate. As a result, the thin carbon layer could not be analyzed by a technique which requires a relatively large volume of material such as x-ray diffraction. However, the film could be closely examined in cross-section by transmission electron microscopy. This should yield far more information about the carbon processing / structure relationship than traditional x-ray

diffraction methods, but could not be done in this investigation because of the difficulty in sample preparation.

Another investigation that could provide more information upon the structure of the interlayers would be to perform a concentration depth profile through the carbon film to the substrate using Auger Spectroscopy. In this way reaction products may be identified. If the process gases preferentially etched either the aluminum or the oxygen in the sapphire substrate, a layer rich in one of the two elements should be present. This would also identify a layer of reaction product such as aluminum carbide. If the Auger technique was found to be unworkable due to electron charging during analysis, secondary ion mass spectroscopy could also yield this type of information.

In light of this present research it is suggested that two directions may be fruitful to the attainment of optimized interfaces desired for composite materials. First, other materials with strengths greater than those of microcrystalline carbon should be considered and studied as interlayers for composites. Boron nitride is a possibility, as it is has been shown to vary in degree of preferred orientation depending on processing. Another approach to optimized interfaces would be to deposit small elemental layers of an embrittling substance which would then alter interface fracture toughness rather than tensile strength. Precipitates grown by overaging in aluminum matrix composites have been shown to enhance fracture toughness in this way [116, 117] and in the last chapter containing suggestions for future work, a method is outlined in which model test specimens with an exact array of fracture initiators could be produced using microelectronic processing techniques.

In summary, what has been achieved is that, in principle, a method has been introduced by which development of composite interfaces may be pursued through the synthesis and characterization of model interface test specimens. This method brings together the processing of interfaces with a mechanical testing method in a way to specifically address composite development. This work has been a first step in an iterative evolution whereby an optimum design may still be reached.
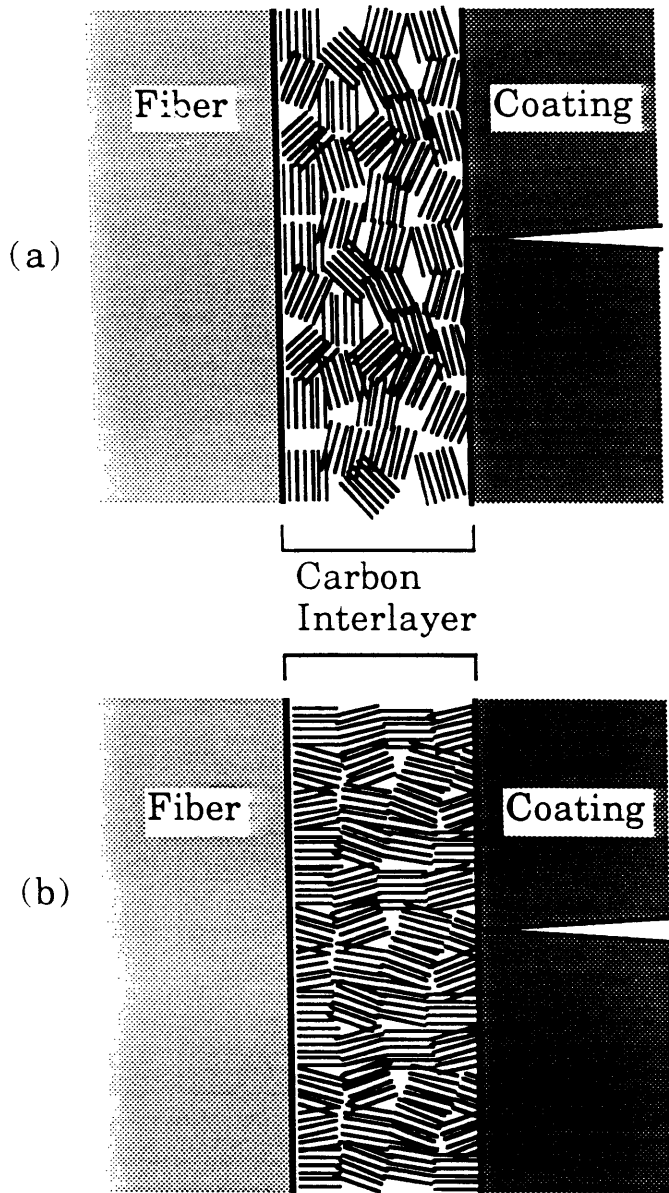
Figure 6.1 Schematic representation of the ideal carbon interlayer (a) and
the carbon layer that would likely be necessary to insure
sufficient transverse strength to meet design criteria for
composite optimization (b).

VII. Conclusions

1. The processing technique necessary to produce low residual stress, homogeneous SiC coatings by plasma enhanced CVD has been determined.

2. The processing of highly oriented carbon by low pressure CVD has been investigated and the processing-structure relationships as a function of deposition temperature have been studied by x-ray diffraction.

3. The experiment whereby the tensile strength of interfaces is determined by laser-induced shock waves has been experimentally and numerically described and used to evaluate the tensile strength of interface couples.

4. Model interface couples with tensile strengths ranging over two orders of magnitude have been processed; however, all couple tensile strengths were radically less than those specified for composite optimization.

VIII. Suggestions for Future Work

There are at least two extensions of this present work which would be of interest. The first would be to examine the effect upon couple tensile strength of carbon interlayers with less preferred orientation than those of this work. The second would be to produce laser test couples with a uniform distribution of "flaws" or "notches" so as to determine the fracture toughness of an interface.

The carbon processed by low pressure CVD in this work was extremely highly oriented with Bacon Anisotropy Factors ranging between 4.5 and 8.0. While it was determined that the strength of model couples varied linearly with the degree of preferred orientation over this range, it would be interesting to find out if this correlation extends to less oriented carbons extending from a BAF of 4.0 down to completely isotropic carbon with a BAF of 1.0. Carbon of this nature could be deposited at higher pressures in a conventional CVD apparatus. This would be the most immediate and fruitful extension of this work.

Previous work with coatings containing the ubiquitous particles showed the possibility of determining the fracture toughness of an interface through the use of laser spallation. Particles in the coating act as flaws and if of known size and distribution would allow the determination of toughness through the spallation experiments. Rather than attempting to regulate the size and distribution of nucleated particles in the plasma, it is here recommended that microelectronic production technology be employed to produce wafers coated with an array of disks or dots on the order of

1.0μm in diameter and 0.1 μm thick. The spacing of these dots could be anywhere from .10 to 1 mm. The cross section of these test couples is shown in Figure 8.1. This approach centers around the introduction of a strength impairing agent, such as perhaps antimony which is well know for producing temper embrittlement in the intergranular fracture of steels.

The processing procedure would be to first deposit the antimony through a shadow mask in the present reactor set-up as shown in Figure 8.2 onto a clean wafer in the evaporator. The shadow mask would be removed while the wafer is still under high vacuum and the wafer would be transferred immediately to the plasma CVD reactor without exposure to atmosphere. A 2.0 μm thick coating of SiC could then be deposited. Production of the shadow mask is the only new experimental work and could be made from a thin silicon wafer in one of the microelectronic facilities on campus. The sequence of processing steps to produce the shadow mask is shown in Figure 8.3. For details on the wet etching steps see Clark [118] and Petersen [75].

Antimony Disks, 1.0 μm in diameter, 1000Å thick

Ceramic Coating: SiC, 2 μm

Sapphire Wafer, 500μm
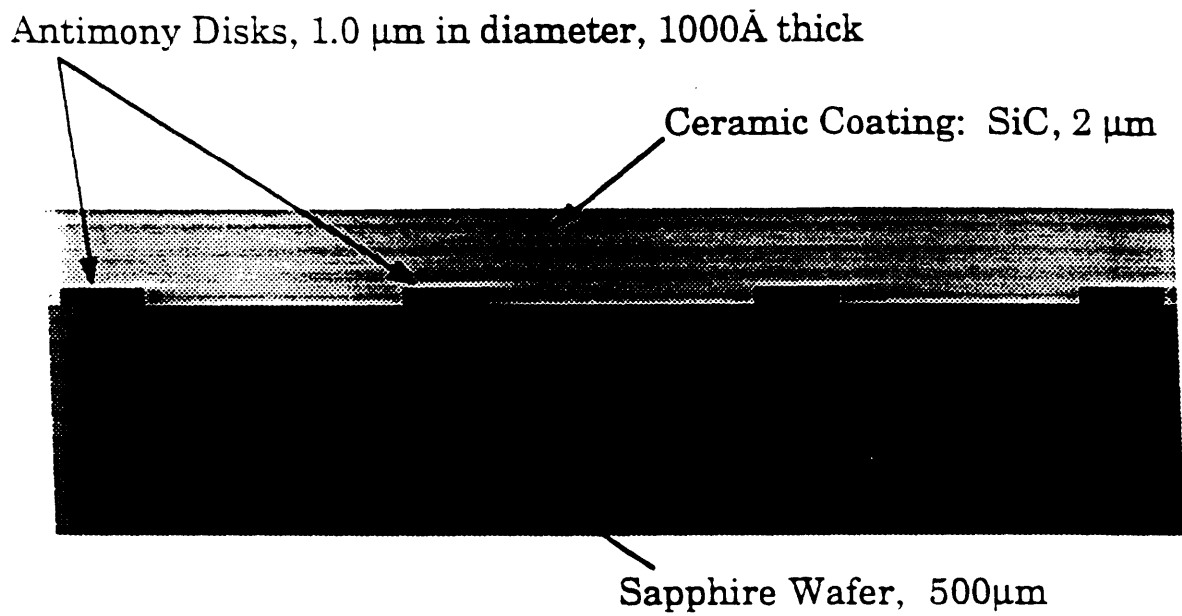
Figure 8.1 Schematic of a test couple used to determine fracture
toughness of an interface.
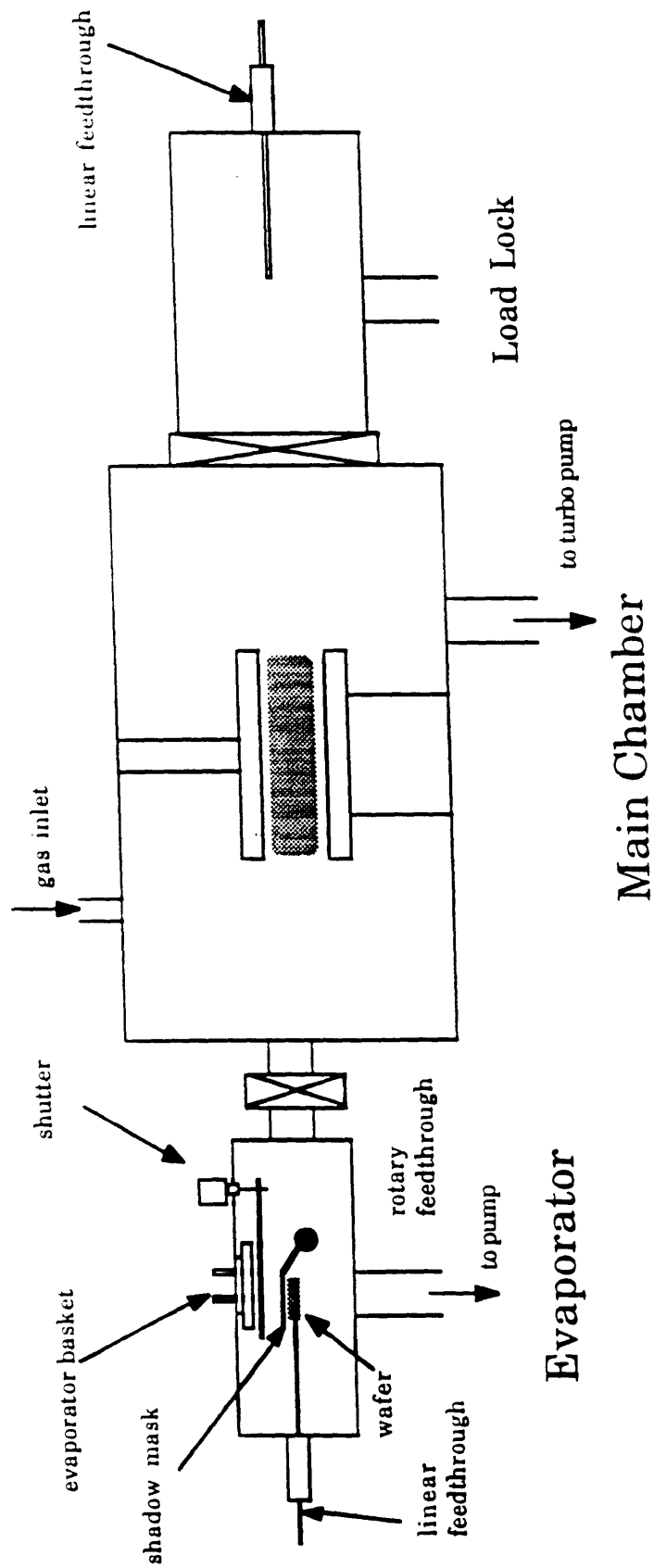
Figure 7.2   Schematic of thermal evaporator in tandem with the PECVD reactor for sequential depositions.
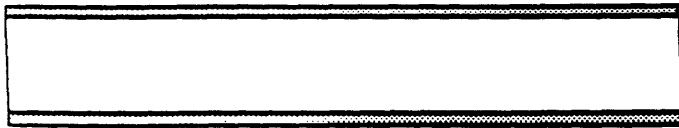
a) Grow silicon oxide
   on each side of wafer

b) Cover both sides with
   resist; expose and
   remove resist on
   backside; strip oxide

c) Remove resist;
   Dope reverse side
   with boron

d) Strip oxide; deposit
   silicon nitride on
   both sides

Figure 8.3   Processing steps used in the production of a shadow mask
              using VLSI techniques.

e) Mask top side with
   resist
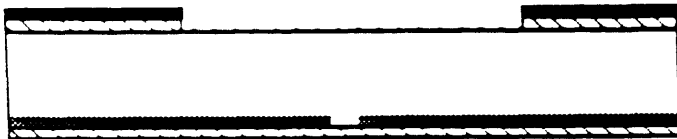
f) Etch top side silicon
   nitride

g) Remove resist; etch
   silicon with KOH

h) Etch nitride on reverse
   side; etch silicon with
   hydrofluoric, nitric,
   and acetic acid

Figure 8.3   Processing steps used in the production of a shadow mask
              using VLSI techniques.

References

1. A.S. Argon, V. Gupta, H.S. Landis, and J.A. Cornie: *Materials Science and Engineering.*, 1989, vol. A107, pp. 41-47.

2. V. Gupta, A.S. Argon, and J.A. Cornie: *Journal of Materials Science*, 1989, vol. 24, pp. 2031-2040.

3. J.A. Cornie, A.S. Argon, and V. Gupta: *MRS Bulletin*, 1991, vol. 16, pp. 32-38.

4. D.H. Grande, J.F. Mandell, and K.C.C. Hong: *Journal Materials Science*, 1988, vol. 23, pp. 311-328.

5. C. Pohthieu, M. Lancin, and J. Thibault-Desseaux: *Philosophical Magazine A*, 1990, vol. 62, pp. 605-615.

6. V. Gupta, A.S. Argon, and Z. Suo: *Journal of Applied Mechanics*, 1992, vol. 59, pp. S79-S86.

7. V. Gupta, J. Yuan, and D. Martinez: *Journal of the American Ceramic Society,* 1993, vol. 76, pp. 305-315.

8. *Engineering Property Data on Selected Ceramics,* Battelle, Columbus Laboratories, July, 1981, MCIC-HB-07.

9. J.C. Bokros: in *Chemistry and Physics of Carbon,* P.L.J. Walker, eds., Marcel Dekker, Inc., New York, 1969, pp. 1-118.

10. D.W. Hess: *Annual Review of Materials Science*, 1986, vol. 16, pp. 163-183.

11. D.W. Hess: in *Silicon Processing,* D.C. Gupta, eds., ASTM, 1983, pp.

12. L.R. Reif and H.H. Sawin: *Plasma Processing in Integrated Circuit Fabrication,* Course Notes, 1987, pp.

13. T.D. Bonnifield: in *Deposition Technologies,* R.R. Bunshah, eds., Noyes Publications, Park Ridge, NJ, 1982, pp. 365-384.

14. A.R. Reinberg: *Annual Review of Materials Science*, 1979, vol. 9, pp. 341-372.

15. K. Tachibana, H. Okuyama, H. Harima, and Y. Urano: in Diagnostics and Modelling of Plasmas used for the CVD of a-C:H, a-Si:H and A-Si$_x$C$_{1-x}$:H Films, Proc. Conf., Eindoven, Netherlands, 1985, eds., pp. 588-593.

16. P. Roca i Cabarrocas: in Detailed Study of Ion Bombardment in RF Glow Discharge Deposition Systems: The Role of Helium Dilution, Proc. Conf., San Diego, CA, 1989, A. Madan, M.J. Thompson, P.C. Taylor, Y. Hamakawa, and P.G. LeComber, eds., Materials Research Society, pp. 33-38.

17. I. Haller: *Journal of Vacuum Science and Technology A*, 1983, vol. 1, pp. 1376-1382.

18. J.L. Andujar, e. Bertran, A. Canillas, C. Roch, and J.L. Morenza: *Journal of Vacuum Science and Technology A*, 1991, vol. 9, pp. 2216-2220.

19. P. Hess: *Journal of Vacuum Science and Technology B*, 1992, vol. 10, pp. 239-247.

20. M.P. Delplancke, J.M. Powers, G.J. Vandentop, M. Salmeron, and G.A. Somorjai: *Journal of Vacuum Science and Technology A*, 1991, vol. 9, pp. 450-455.

21. Y. Catherine, G. Turban, and B. Grolleau: *Thin Solid Films*, 1981, vol. 76, pp. 23-33.

22. R.N. Rudolph and J.H. Moore: *Plasma Chemistry and Plasma Processing*, 1990, vol. 10, pp. 451-471.

23. A. Gallagher: in Surface Reactions in Discharge and CVD Deposition of Silane, Proc. Conf., Palo Alto, CA, 1986, D. Adler, Y. Hamakawa, and A. Madan, eds., Materials Research Society, pp. 3-10.

24. A. Gallagher: *Journal of Applied Physics*, 1988, vol. 63, pp. 2406-2413.

25. A. Gallagher, J. Doyle, and D. Doughty: in Plasma Chemistry in Silane and Silane-Germane Discharge Deposition, Proc. Conf., San Diego, CA, 1989, A. Madan, M.J. Thompson, P.C. Taylor, Y. Hamakawa, and P.G. LeComber, eds., Materials Research Society, pp. 23-31.

26. R. Robertson and A. Gallagher: *Journal of Applied Physics*, 1986, vol. 59, pp. 3402-3411.

27. S. Veprek, M. Heintze, F. Sarott, M. Jurcik-Rajman, and P. Willmott: in Mechanisms of Plasma Induced Silicon Deposition and the Control of the Properties of the Deposit, Proc. Conf., San Diego, CA, 1988, A. Madan, M.J. Thompson, P.C. Taylor, P.G. LeComber, and Y. Hamakawa, eds., Materials Research Society, pp. 3-17.

28. S. Veprek: *Thin Solid Films*, 1989, vol. 175, pp. 129-139.

29. S. Veprek, F. Sarrott, S. Rambert, and E. Taglauer: *Journal of Vacuum Science and Technology* A, 1989, vol. 7, pp. 26142624.

30. S. Veprek, M. Heintze, R. Bayer, and M. Jurick-Rajman: in From the Understanding of the Reaction Mechanism Towards Optimizing the Deposition Rate and Optoelectronic Properties of a-Si:H, Proc. Conf., San Diego, CA, 1989, A. Madan, M.J. Thompson, P.C. Taylor, Y. Hamakawa, and P.G. LeComber, eds., Materials Research Society, pp. 3-9.

31. S. Veprek and M. Heintze: *Plasma Chemistry and Plasma Processing*, 1990, vol. 10, pp. 3-26.

32. S. Veprek: *Journal De Physique*, 1989, vol. C5, pp. 617-635.

33. Ross, F. To be published.

34. K. Tachibana, M. Nishida, H. Harima, and Y. Urano: *Journal of Physics D: Applied Physics*, 1984, vol. 17, pp. 1727-1742.

35. K. Yamamoto, Y. Ichikawa, N. Fukada, T. Nakayama, and Y. Tawada: *Thin Solid Films*, 1989, vol. 173, pp. 253-262.

36. A.H. Mahan, P. Raboisson, D.L. Williamson, and R. Tsu: *Solar Cells*, 1987, vol. 21, pp. 117-126.

37. Y.J. Chabal and C.K.N. Patel: *Reviews of Modern Physics*, 1987, vol. 59, pp. 835-844.

38. H. Wagner and W. Beyer: *Solid State Communications*, 1983, vol. 48, pp. 585-587.

39. R.W. Collins: in In situ Studies of the Microstructure of a-Si:H Surfaces and Interfaces, Proc. Conf., Palo Alto, CA, 1986, D. Adler, Y. Hamakawa, and A. Madan, eds., Materials Research Society, pp. 361-366.

40. R.W. Collins: *Journal of Vacuum Science and Technology* A, 1989, vol. 7, pp. 13781385.

41. M.A. Petrich, K.K. Gleason, and J.A. Reimer: *Physical Review B*, 1987, vol. 36, pp. 9722-9731.

42. R. Demichelis, G. Kaniadakis, E. Mezzeetti, P. Mpawenayo, A. Tagliaferro, E. Tresso, P. Rava, and G. Della Mea: *Il Nuovo Cimento*, 1987, vol. 9, pp. 393-407.

43. D.L. Williamson, A.H. Mahan, B.P. Nelson, and R.S. Crandall: *Applied Physics Letters,*, 1989, vol. 55, pp. 783-785.

44. H. Landis: PhD, Massachusetts Insititute of Technology,

45. Herbots, N. Private communication.

46. W.A.P. Claassen, W.G.J.N. Valkenburg, M.F.C. Wilemsen, and W.M.v.d. Wijgert: *Journal of the Electrochemical Society*, 1985, vol. 132, pp. 893-898.

47. A.K. Sinha, H.J. Levinstein, T.E. Smith, G. Quintana, and S.E. Haszko: *Journal of the Electrochemical Society*, 1978, vol. 125, pp. 601-608.

48. K.G. Spears and R.M. Roth: in Spatial Resolution of Small Prticles in Silane Discharge, Proc. Conf., Boston, MA, 1985, R.P.H. ChangandB. Abeles, eds., Materials Research Society, pp. 111-116.

49. M.J. McCaughey and M.J. Kushner: *Applied Physics Letters*, 1989, vol. 54, pp. 1642-1644.

50. J.C. Knights, R.A. Lujan, M.P. Rosenblum, R.A. Street, D.K. Bieglesen, and J.A. Reimer: *Applied Physics Letters,*, 1981, vol. 38, pp. 331-333.

51. F.J. Kampas: *Journal of Applied Physics*, 1983, vol. 54, pp. 2276-2280.

52. Sawin, H. H. Private communication.

53. H. Windischmann: *Journal of Vacuum Science and Technology* A, 1991, vol. 9, pp. 2459-2463.

54. H. Windischmann, R.W. Collins, and J.M. Cavese: *Journal of Non-Crystalline Solids*, 1986, vol. 85, pp. 261-272.

55. J. Schliwinski, M. Pelka, L. Buchmann, W. Windbracke, P. Lange, and L. Csepregi: *Materials Science and Engineering B*, 1992, vol. 11, pp. 73-77.

56. S. Boily, M. Chaker, A. Ginovker, P.P. Mercier, H. Pepin, J.C. Kieffer, J.F. Currie, and H. Lafontaine: *Canadian Journal of Physics*, 1991, vol. 69, pp. 438-440.

57. N.P. EerNisse: *Journal of Applied Physics*, 1977, vol. 48, pp. 3337-3341.

58. M. Sekimoto, H. Yoshihara, and T. Ohkubo: *Journal of Vacuum Science and Technology* A, 1982, vol. 21, pp. 1017-1021.

59. R. Srinivasan, B.C. Nguyen, and A.P. Short: in Plasma Enhanced Chemical Vapor Deposition of Dielectric Films: Correlation of Stress to Film Structure and Plasma Characteristics, Proc. Conf., San Fransico, CA, 1990, M.F. Doerner, W.C. Oliver, G.M. Pharr, and F.R. Brotzen, eds., pp. 73-78.

60. K. Aite, J. Holleman, J. Middelhoek, and R. Koekoek: in The Relationship between Intrinsic Stress of Silicon Nitride Films and Ion Generation in a 50 kHz RF Discharge, Proc. Conf., Boston, MA, 1989, J.C. Bravman, W.D. Nix, D.M. Barnett, and D.A. Smith, eds., pp. 347-353.

61. K. Aite, R. Koekoek, J. Holleman, and J. Middelhoek: *Journal De Physique*, 1989, vol. C5, pp. 323-331.

62. K. Aite and R. Koekoek: in Intrinsic Stress of PECVD Silicon Oxynitride Filmes Deposited in a Hot-Wall Reactor, Proc. Conf., San Fransico, CA, 1990, M.F. Doerner, W.C. Oliver, G.M. Pharr, and F.R. Brotzen, eds., pp. 85-90.

63. J.A. Taylor: *Journal of Vacuum Science and Technology* A, 1991, vol. 9, pp. 2464-2468.

64. D.C.H. Yu and J.A. Taylor: in Correlation Between Processing, Composition, and Mechanical Properties of PECVD-SiN$_x$ Thin Films, Proc. Conf., San Fransico, CA, 1990, M.F. Doerner, W.C. Oliver, G.M. Pharr, and F.R. Brotzen, eds., pp. 79-84.

65. J. Lopata, W.C. Dautremont-Smith, and J.W. Lee: in Control and Variation of Stress in PECVD SiN$_x$ Films on InP, Proc. Conf., Boston, MA, 1989, J.C. Bravman, W.D. Nix, D.M. Barnett, and D.A. Smith, eds., pp. 361-366.

66. B. Bhushan, S.P. Murarka, and J. Gerlach: *Journal of Vacuum Science and Technology* B, 1990, vol. 8, pp. 1068-1074.

67. R.W. Hoffman: in *Physics of Thin Films,* G. Hassand and R.E. Thun, eds., Academic Press, New York, 1966, pp. 211-273.

68. W. Beyer, H. Wagner, and H. Mell: in Bonding and Release of Hydrogen in a-Si:C:H Alloys, Proc. Conf., 1985, eds., Materials Research Society, pp. 189-194.

69. A.H. Mahan, D.L. Williamson, and B.P. Nelson: in Microvoids and Photoconductivities in a-SiC:H and a-Si:H, Proc. Conf., San Diego, CA, 1989, A. Madan, M.J. Thompson, P.C. Taylor, and Y. Hamakawa, eds., Materials Research Society, pp. 539-543.

70. P. D'Antonio and J.H. Konnert: *Physical Review Letters*, 1979, vol. 43, pp. 1161-1163.

71. R.C. Budhani, R.F. Bunshah, and P.A. Flinn: *Applied Physics Letters*, 1988, vol. 52, pp. 284-286.

72. S.P. Timoshenko and J.N. Goodier: *Theory of Elasticity*, 3rd, McGraw Hill, London, 1982, pp. 394-395.

73. Y.C. Ku: PhD, MIT,

74. J.L. Vossen and W. Kern: *Thin Film Processes*, Academic Press, New York, 1978, pp. 564.

75. K.E. Petersen: *Proceedings of the IEEE* , 1982, vol. 70, pp. 420-457.

76. L. Holland and S.M. Ojha: *Thin Solid Films*, 1979, vol. 58, pp. 107-116.

77. S. Berg and L.P. Andersson: *Thin Solid Films*, 1979, vol. 58, pp. 117-120.

78. L.P. Andersson, S. Berg, H. Norstrom, and R. Olaison: *Thin Solid Films*, 1979, vol. 63, pp. 155-160.

79. H. Minagawa, I. Fujita, T. Hino, and T. Yamashina: *Surface and Coatings Technology*, 1990, vol. 43/44, pp. 813-820.

80. H. Shimizu, S. Nakao, H. Kusakabe, and M. Noda: *Journal of Non-Crystalline Solids*, 1989, vol. 114, pp. 196-198.

81. B.S. Meyerson: in Hydrogenated Amorphous Carbon, An Overview, Proc. Conf., 1986, eds., Materials Research Society, pp. 191-198.

82. A. Inspektor, Y. Hornik, U. Carmi, R. Avni, E. Wallura, H. Hoven, K. Koizlik, and H. Nickel: *Thin Solid Films*, 1980, vol. 72, pp. 195-200.

83. *X-Ray Photoelectron and X-Ray Induced Auger Electron Spectroscopic Data*, T.A. Sasaki and Y. Baba, Japan Atomic Energy Research Institute, June, 1985, 85-063.

162

84. D. Briggs: in *Practical Surface Analysis,* D. BriggsandM.P. Seah, eds., John Wiley and Sons, New York, 1981, pp. 292.

85. R.H. Bragg, D.D. Crooks, R.W.J. Fenn, and M.L. Hammond: *Carbon,* 1964, vol. 1, pp. 171-179.

86. A.R. Ubbelohde: *Endeavour,* 1965, vol. 24, pp. 63-68.

87. J.C. Bokros: *Carbon,* 1965, vol. 3, pp. 201-211.

88. P.A. Tesner: in *Chemistry and Physics of Carbon,* P.A. Thrower, eds., Marcel Dekker, New York, 1983, pp. 65-161.

89. C.F. Powell, J.H. Oxley, and J.M.J. Blocher: *Vapor Deposition,* John Wiley and Sons, New York, 1973, pp.

90. R.J. Diefendorf and E.R. Stover: *Metals Progress,* 1962, vol. 81, pp. 103-108.

91. R.J. Diefendorf: in Deposition of Pyrolytic Carbons, Proc. Conf., Schenectady, New York, 1968, J.W. Mitchell, R.C. DeVries, R.W. Roberts, and P. Cannon, eds., Wiley-Interscience, pp. 461-475.

92. H.O. Pierson and M.L. Lieberman: *Carbon,* 1975, vol. 13, pp. 159-166.

93. J.L. Kaae: *Carbon,* 1985, vol. 23, pp. 665-673.

94. M.L. Lieberman: in Chemical Vapor Deposition of Carbon: A Model to Relate Gas Phase Conditions to Structure of Deposit, Proc. Conf., Salt Lake City, Utah, 1971, F.A. Glaski, eds., American Nuclear Society, pp. 95-119.

95. M.L. Lieberman: *Carbon,* 1975, vol. 13, pp. 243-244.

96. M.L. Lieberman and G.T. Noles: *Carbon,* 1974, vol. 12, pp. 693-696.

97. P. Lucas and A. Marchand: *Carbon,* 1990, vol. 28, pp. 207-219.

98. R.J. Akins and J.C. Bokros: *Carbon,* 1974, vol. 12, pp. 439-452.

99. Y. Yoshimoto, T. Suzuki, Y. Higashigaki, and S. Nakajima: *Thin Solid Films,* 1988, vol. 162, pp. 273-278.

100. J. Lahaye, G. Prado, and J.B. Donnet: *Carbon,* 1974, vol. 12, pp. 27-35.

101. F. Kobayashi, K. Ikawa, and K. Iwamoto: *Carbon,* 1974, vol. 12, pp. 87-90.

102. W.P. Hoffman and F.J. Vastola: *Carbon,* 1985, vol. 23, pp. 151-161.

103. W.P. Hoffman, F.J. Vastola, and J. Walker P. L.: *Carbon*, 1988, vol. 26, pp. 485-499.

104. B.E. Warren: *Journal of Chemical Physics*, 1934, vol. 2, pp. 693.

105. G.E. Bacon: *Journal of Applied Chemistry*, 1956, vol. 6, pp. 477-481.

106. R.C. Reid and T.K. Sherwood: *The Properties or Gases and Liquids*, McGraw-Hill, New York, 1966, pp.

107. R.B. Bird, W.E. Stewart, and E.N. Lightfoot: *Transport Phenomena*, John Wiley and Sons, New York, 1960, pp.

108. B.N. Chapman: *Glow Discharge Processes*, John Wiley and Sons, New York, 1980, pp.

109. C.H.J. Van Den Brekel: *Philips Research Reports*, 1977, vol. 32, pp. 118-133.

110. C.H.J. Van Den Brekel and J. Bloem: *Philips Research Reports*, 1977, vol. 32, pp. 134-146.

111. R.A. Graham, F.W. Neilson, and W.B. Benedict: *Journal of Applied Physics*, 1965, vol. 36, pp. 1775-1783.

112. M. Von Allmen: *Laser-Beam Interactions with Materials*, Springer-Verlag, Berlin, 1987, pp. 232.

113. Achenbach: *Wave Propogation in Elastic Solids*, North-Holland Pub. Co., Amsterdam, 1975, pp. 425.

114. L. Lev and A.S. Argon, To be published.

115. G. Eason: *Journal of the Insititute for Maths Applics* , 1966, vol. 2, pp. 299-336.

116. J.A. Cornie, M. Selzenev, M. Ralph, and F. Armatis: Materials Science and Engineering A, vol. 162, pp.135-142

117. M. Seleznev, J.A. Cornie, and F. Armatis: *Journal of Materials Engineering and Performance* , 1993, vol. 2, pp. 347-352.

118. L.D. Clark, J.L. Lund, and D.J. Edell: in Cesium Hydroxide (CsOH): A Useful Etchant for Micromachining Silicon, Proc. Conf., Hilton Head, South Carolina, 1988, IEEE.